

**A study of spin-parity assignments in
18Ne using the 20Ne(p,t)18Ne
reaction**

A Dissertation Presented for the
Doctor of Philosophy
Degree
The University of Tennessee, Knoxville

Paul James Thompson

August 2018

© by Paul James Thompson, 2018
All Rights Reserved.

To my husband Ben, and my parents, Karen and Robert.

Acknowledgments

I met a large number of people through this project, all of whom had their own impact on me, and this work. Firstly I would like to thank my research advisor, Dr. Kelly Chipps, for providing me with the motivation and support, without which this work would not have been possible. Thank you for providing advice and guidance, and for providing the opportunities to work with other research groups on a multitude of different projects. My PhD advisor Dr. Kate Jones, who provided advice through my PhD, and who facilitated the partnership between the low energy experimental physics group at the university of Tennessee, and the astrophysics group at Oak Ridge National Laboratory. Thank you Dr. Steve Pain, for your advice and guidance through this project (And the fantastic home-made cider). Finally, I would like to thank the friends and family who have been there for me through the years, and helped me when I needed them. I wouldn't have been able to finish this without your support and friendship. Thank you James Cliffe, Clay Culp, Ben Estes, Philip Hartzell, Alex Lepailleur, Jeffery Palluck, Robert Potts, Grant Riley, Karen and Robert Thompson, Cory Thornsberry, and Marija Vostinar.

Abstract

Several key states in ^{18}Ne [Neon-18] affect the reaction rate of the astrophysically-important ^{14}O [Oxygen-14](α [Alpha],p) ^{17}F [Fluorine-17] reaction, important for breakout of the Hot-CNO cycle and key to the ignition of Type-I X-ray bursts. Currently, a direct measurement of the $^{14}\text{O}(\alpha,\text{p})^{17}\text{F}$ reaction cross section is extremely difficult. Instead, calculation of the stellar reaction rate depends on the parameters of the states in the fusion product nucleus ^{18}Ne , which can be studied indirectly through transfer reactions. With the development of the Jet Experiments in Nuclear Structure and Astrophysics (JENSA) gas jet system, targets of pure gas are achievable, opening new avenues for studies with transfer reactions. In order to investigate states in ^{18}Ne , the ^{20}Ne [Neon-20](p,t) ^{18}Ne reaction was utilized with a pure neon target from the JENSA system and an array of highly-segmented silicon strip detectors. Distorted wave Born-approximation (DWBA) calculations were then compared to experimental angular distributions, and a number of spin-parity assignments are made for states in ^{18}Ne .

Table of Contents

1	Introduction	1
1.1	Astrophysics	1
1.1.1	Stellar evolution	1
1.1.2	Hydrogen fusion	2
1.1.3	The CNO cycle	3
1.1.4	The hot CNO cycle	3
1.1.5	Binary stars and X-ray binaries	4
1.1.6	X-ray bursts	4
1.1.7	rp-process	6
1.2	Stellar reaction rates	7
1.2.1	Gamow window	9
1.3	^{18}Ne and hot-CNO breakout	9
1.3.1	Previous studies	10
1.4	Motivation	16
2	Basic Nuclear Structure and Reaction Theory	18
2.1	Nuclear structure	18
2.1.1	Transfer reactions	18
2.1.2	Reactions in normal kinematics	19
2.1.3	Basic nuclear structure	21
2.1.4	Thomas-Erhman shifts	23
2.2	Distorted wave Born approximation	24
2.2.1	DWBA	24

2.2.2	DWBA parameter variations	26
2.2.3	Finite range, zero range and LEA	28
3	Instrumentation	33
3.1	Target	33
3.1.1	Overview	33
3.1.2	Commissioning of JENSA	34
3.1.3	Nozzles	36
3.1.4	Measurement of jet density	36
3.1.5	JENSA for the $^{20}\text{Ne}(p,t)^{18}\text{Ne}$ study	41
3.2	Beam production	43
3.3	Detectors	43
3.3.1	Silicon detectors	43
3.3.2	Detector configuration	44
3.3.3	Electronics	46
4	$^{20}\text{Ne}(p,t)^{18}\text{Ne}$ Calibration and Analysis	47
4.1	Experimental setup	47
4.2	Calibration	49
4.2.1	Segmentation of the data and initial calibration	49
4.2.2	Solid angle calibration	53
4.2.3	Secondary gain coefficients	55
4.3	Residuals	57
4.3.1	Strip downtime corrections	58
4.3.2	Contamination	61
4.3.3	Fitting	63
4.4	Nitrogen background	73
5	Results	74
5.1	Ground state	75
5.2	$E_x = 1887$ keV state	76

5.3	$E_x = 3376$ keV state	77
5.4	$E_x = 3576$ keV state	78
5.5	$E_x = 3616$ keV state	81
5.6	$E_x = 3600$ keV doublet treated as single peak	82
5.7	$E_x = 4520$ keV state	82
5.8	$E_x = 4590$ keV state	84
5.9	$E_x = 5090$ keV state	86
5.10	$E_x = 5146$ keV state	88
5.11	$E_x \approx 5100$ keV doublet treated as single peak	89
5.12	$E_x = 5450$ keV state	90
5.13	$E_x = 6150$ keV state	92
5.14	$E_x = 6297$ keV state	93
5.15	$E_x = 6353$ keV state	94
5.16	$E_x \approx 6300$ keV doublet treated as single peak	95
5.17	Potential candidate state at $E_x \approx 5300$ keV	95
6	Conclusions	101
6.1	States $E_x > 6000$ keV	101
6.2	States $4500 < E_x < 4600$ keV	103
6.3	States $5000 < E_x < 5500$ keV	104
6.3.1	$E_x = 5450$ keV	104
6.3.2	Candidate for a previously unobserved state at $E_x = 5309 \pm 13$ keV	104
6.3.3	$E_x = 5090$ keV and $E_x = 5146$ keV states	105
6.4	Bound states	106
6.4.1	Ground state	106
6.4.2	$E_x = 1887$ keV state	106
6.4.3	$E_x = 3376$ keV state	107
6.4.4	$E_x = 3576$ keV and $E_x = 3616$ keV states	107
6.5	Commissioning of JENSA	108
6.6	Further work	108

Bibliography	110
Appendices	116
A Length of runs	117
B Downtime correction values and uncertainties	118
C List of collaborators	124
D Excitation energies	125
Vita	126

List of Tables

1.1	Values for E_x and J_π for $E_x < 4000$ keV states in ^{18}Ne as reported in R.D Gill et. al[1].	12
1.2	Excitation energy (E_x) and spin-parity assignments (J^π) of states in ^{18}Ne as listed on the most recent Evaluated Nuclear Structure Data File (ENSDF)[2]. As of March 2018, the latest compilation including ^{18}Ne was performed in 1995. References are given as listed on ENSDF, with citations of the individual papers which comprise the list and corresponding reaction studied. A: ^{18}Ne β^+ -decay[3, 4] B: $^{12}\text{C}(^{12}\text{C},^6\text{He})$ [2] C: $^{14}\text{O}(\alpha,\gamma)$ [2] D: $^{16}\text{O}(^3\text{He},n)$ [5, 3, 6] E: $^{16}\text{O}(^{10}\text{B},^8\text{Li})$ [2] F: $^{16}\text{O}(^{12}\text{C},^{10}\text{Be})$ [7] G: $^{18}\text{O}(\pi^+,\pi^-)$ [3, 4] H: $^{20}\text{Ne}(p,t)$ [8, 2, 9] .	12
1.3	Current status of the literature regarding excitation energies (E_x) and spin-parity assignments (J^π) of states in ^{18}Ne . There have been other studies focusing on the particle widths of states in ^{18}Ne but those have been omitted for this table as, while important for reaction rate calculations, they are not pertinent to the present study. Values in the leftmost column represent ENSDF[2] listings. As of March 2018, the latest ENSDF compilation including ^{18}Ne was performed in 1995. References are given in chronological order. . .	13
2.1	These parameters were used for all DWBA calculations shown in Chapter 5. These are as listed in Park et al[10].	26
2.2	The baseline parameters listed below were used for the sensitivity search in this section, and correspond to parameter set 4 from Falk et al[9]. TWOFNR uses $r_v = r_D$ and $a_v = a_D$ and therefore the value listed for a_V was used for a_D , not $a_D = 0.54$ fm.	27

3.1	Vacuum pump specifications as listed on the manufactures specification sheets for the JENSA system as shown in the pumping schematic (Figure 3.1). . . .	34
3.2	Aperture dimensions (Parameters from Chipps et al[11]) for the JENSA system as shown in the pumping schematic (Figure 3.1). The restrictive apertures upstream limit allow a high pressure jet in the target chamber and limit gas flow up the beam line.	34
3.3	JENSA nozzle specifications. These parameters correspond to the lengths as labeled on Figure 3.2b and are given in mm. Tolerances for the individual lengths are listed in the last row. Specifications are from Schmidt et al[12]. .	38
3.4	Natural abundances of neon isotopes[13].	41
3.5	Pertinent specifications for a single Micron Semiconductors Ltd YY1 detector, used in SIDAR[14].	44
4.1	Serial numbers and thicknesses of the six silicon detectors used in SIDAR for this measurement.	48
4.2	Q-value for the reaction channel of interest and other potentially relevant Q-values. As the target used was ^{Nat}Ne , we know approximately 9.5% of the target material is ^{22}Ne . If air somehow bled into the JENSA target system, we could expect to see light recoil nuclei from reactions on ^{16}O and ^{14}N	49
4.3	These sets contain a number of consecutive runs where the gain in the measured light products does not seem to shift. This was performed by eye, looking a ΔE vs E plots and deciding points where multiple channel's gains appeared to shift by a noticeable amount.	51
4.4	Solid angle values used for each strip in each telescope.	56
4.5	Downtime correction factors for telescope 1.	60
4.6	Downtime correction factors for telescope 2.	60
4.7	Final correction factors. These factors represent the number of raw counts in the ground state of $^{20}Ne(p,t)^{18}Ne$ as a ratio to the total number of counts recorded in the corresponding strip. $\sum N_x^n / N_{total}^n = 1$	61

4.8	These final downtime correction factors take into account which strips were off for whichever runs and are the values that the final fits need to be applied to correct for strip downtime.	62
4.9	Parameters of calculated kinematic lines for tritons measured from two of the intersecting states. These used an angular range of 18° to 52° in the laboratory.	63
4.10	Parameters of measured kinematic lines for tritons measured from the two intercepting states. Fit E takes the same strips as D, but 2 additional points are included where the nitrogen triton peak is not fully independent from the neon triton peaks.	64
4.11	Comparisons of the expected crossing point of the kinematic lines, and a comparison of the crossing points calculated using the assumed angles of each strip. The calculated crossing points show that the measured distances were incorrect, and the crossing strip, strip 6, should be at the calculated crossing point of around 30° in the lab frame. The intersection of A and B is the calculated crossing point, while intersection of both C and D, and C and E came from measurements. The difference of 2° demonstrates the initial calculation of the laboratory angles was incorrect.	65
4.12	List of whether the mean of the state was fixed in the fit, or allowed to vary	66
4.13	Listed are the values of energy per bin used when fitting each strip. Binning was adjusted on a strip by strip basis to account for the changes in statistics and the changes in resolution. The energy per channel is always approximately 5 keV, changes in binning are changes in the number of adjacent channels combined	70
4.14	Q-Values used by larelkin[15] for kinematic calculations	70
4.15	Laboratory angles for each of the corresponding strips.	71
5.1	Proton beam energies and targets used in the present work and previous $^{20}\text{Ne}(p,t)^{18}\text{Ne}$ studies.	75

5.2	J^π and E_x values for the $E_x = 1887$ keV state from Gill et al[1] and the present study. There is slight disagreement between the present value of the excitation energy and the value from Gill et al[1] of 6 keV.	77
5.3	J^π and E_x values from Gill et al[1] and extracted from these data for the $E_x = 3376$ keV state.	78
5.4	J^π and E_x values from Gill et al[1] and as extracted from these data for the $E_x = 3576$ keV state.	80
5.5	J^π and E_x values from Gill et al[1] and the results from these data for the $E_x = 3616$ keV state.	82
5.6	J^π and E_x values from Garcia et al[5], Hahn et al[16] and as extracted from these data for the $E_x = 4520$ keV state.	84
5.7	χ^2 values when comparing the angular distribution from this study to DWBA calculations for the different L transfers for the $E_x = 4520$ keV state in ^{18}Ne	85
5.8	J^π and E_x values from as extracted from these data, from Garcia et al[5] and Hahn et al[16] for the $E_x = 4590$ keV state.	86
5.9	χ^2 values for comparing the angular distribution from this study to DWBA calculations for different L transfers for the $E_x = 4590$ keV state.	87
5.10	J^π and E_x values from Nero et al[8], Hahn et al[16], and Park et al[10], and from these data for the $E_x=5090$ keV state.	87
5.11	χ^2 values for comparing the angular distribution from this study to DWBA calculations for the different possible L transfers for the $E_x = 5090$ keV state.	89
5.12	J^π and E_x values from Nero et al[8], Hahn et al[16], and Park et al[10], and as extracted from these data for the $E_x = 5146$ keV state.	89
5.13	χ^2 values when comparing the angular distribution from this study to DWBA calculations for the different possible L transfers for the $E_x = 5146$ keV state.	89
5.14	J^π and E_x values from Nero et al[8], Hahn et al[16], and Park et al[10], and from these data for the $E_x = 5450$ keV state.	91
5.15	χ^2 values for the different possible L transfers for the $E_x = 5450$ keV state. .	92
5.16	J^π and E_x values from previous studies and from these data for the $E_x = 6150$ keV state.	94

5.17	χ^2 values for comparing the angular distribution from this study to DWBA calculations for the different possible L transfers for the $E_x = 6150$ keV state.	94
5.18	J^π and E_x values from literature and as extracted from these data for the $E_x = 6300$ keV state.	96
5.19	χ^2 values for comparing the angular distribution from this study to DWBA calculations for the different possible L transfers for the $E_x = 6297$ keV state.	96
5.20	J^π and E_x values from literature and from these data for the $E_x = 6353$ keV state.	97
5.21	χ^2 values comparing the angular distribution from this study to DWBA calculations for the different possible L transfers for the $E_x = 6353$ keV state.	97
5.22	χ^2 values for comparing the angular distribution from this study to DWBA calculations for the different possible L transfers for the $E_x = 5300$ keV state.	100
1	Length of runs	117
2	Number of counts in the peak corresponding to ^{18}Ne tritons in telescope 1 for runs included in set 1. The uncertainty reported by the fit and the statistical uncertainty ($\frac{\sqrt{N}}{N}$) are listed.	118
3	Number of counts in the peak corresponding to ^{18}Ne tritons in telescope 2 for runs included in set 1. The uncertainty reported by the fit and the statistical uncertainty ($\frac{\sqrt{N}}{N}$) are listed.	118
4	Number of counts in the peak corresponding to ^{18}Ne tritons in telescope 3 for runs included in set 1. The uncertainty reported by the fit and the statistical uncertainty ($\frac{\sqrt{N}}{N}$) are listed.	119
5	Number of counts in the peak corresponding to ^{18}Ne tritons in telescope 1 for runs included in set 2. The uncertainty reported by the fit and the statistical uncertainty ($\frac{\sqrt{N}}{N}$) are listed.	119
6	Number of counts in the peak corresponding to ^{18}Ne tritons in telescope 2 for runs included in set 2. The uncertainty reported by the fit and the statistical uncertainty ($\frac{\sqrt{N}}{N}$) are listed.	119

7	Number of counts in the peak corresponding to ^{18}Ne tritons in telescope 3 for runs included in set 2. The uncertainty reported by the fit and the statistical uncertainty ($\frac{\sqrt{N}}{N}$) are listed.	120
8	Number of counts in the peak corresponding to ^{18}Ne tritons in telescope 1 for runs included in set 3. The uncertainty reported by the fit and the statistical uncertainty ($\frac{\sqrt{N}}{N}$) are listed.	120
9	Number of counts in the peak corresponding to ^{18}Ne tritons in telescope 2 for runs included in set 3. The uncertainty reported by the fit and the statistical uncertainty ($\frac{\sqrt{N}}{N}$) are listed.	120
10	Number of counts in the peak corresponding to ^{18}Ne tritons in telescope 3 for runs included in set 3. The uncertainty reported by the fit and the statistical uncertainty ($\frac{\sqrt{N}}{N}$) are listed.	121
11	Number of counts in the peak corresponding to ^{18}Ne tritons in telescope 1 for runs included in set 4. The uncertainty reported by the fit and the statistical uncertainty ($\frac{\sqrt{N}}{N}$) are listed.	121
12	Number of counts in the peak corresponding to ^{18}Ne tritons in telescope 2 for runs included in set 4. The uncertainty reported by the fit and the statistical uncertainty ($\frac{\sqrt{N}}{N}$) are listed.	121
13	Number of counts in the peak corresponding to ^{18}Ne tritons in telescope 3 for runs included in set 4. The uncertainty reported by the fit and the statistical uncertainty ($\frac{\sqrt{N}}{N}$) are listed.	122
14	Number of counts in the peak corresponding to ^{18}Ne tritons in telescope 1 for runs included in set 5. The uncertainty reported by the fit and the statistical uncertainty ($\frac{\sqrt{N}}{N}$) are listed.	122
15	Number of counts in the peak corresponding to ^{18}Ne tritons in telescope 2 for runs included in set 5. The uncertainty reported by the fit and the statistical uncertainty ($\frac{\sqrt{N}}{N}$) are listed.	122
16	Final correction factors. These factors represent the number of raw counts in the ground state of $^{20}\text{Ne}(\text{p,t})^{18}\text{Ne}$ as a ratio to the total number of counts recorded in the corresponding strip. $\sum N_x^n / N_{total}^n = 1$	123

17	Downtime correction factors for telescope 1.	123
18	Downtime correction factors for telescope 2.	123
19	Individual excitation energies for each strip, extracted from these data. All energies are given in keV.	125

List of Figures

1.1	A Hertzsprung-Russell (HR) diagram[17] with the life cycle of a star like our Sun mapped on it. HR diagrams show stellar luminosity (Energy emitted per unit time). Most observable stars ($\sim 90\%$) lie on the main sequence, and stars typically spend around 90% of their life on the main sequence.	2
1.2	A main sequence star evolves into a red giant, causing material to push past the limit Roche limit, where material is gravitationally bound to it. The binary partner, in the case for Type-I X-ray bursts a neutron star, accretes this material[18].	5
1.3	Diagram showing the HCNO-I cycle (Light Blue), the path to transition ^{14}O to ^{15}O (Orange), and three potential hot-CNO breakout mechanisms (Red, Dark Blue and Green).	6
1.4	The maximum extent of the rp-process path reached for a long, hydrogen-rich burst. In this explosive nucleosynthesis, nuclei pass through a rapid chain of proton captures and β -decays, generating energy two orders of magnitude faster than typical nucleosynthesis (Such as the p-p chain)[19]. Figure from Langanke and Schatz[20]	7
1.5	Cyburt et al[21] investigated the sensitivity of current X-ray burst models by varying 96 different reaction rates. Light curves when varying reaction rates of $^{14}\text{O}(\alpha, p)^{17}\text{F}$ and $^{15}\text{O}(\alpha, \gamma)^{19}\text{Ne}$ by a factor of 10 both up and down are shown. Both Figures are from Cyburt et al[21]	11
1.6	Level diagram for ^{18}Ne generated from levels and spin-parity assignments in the latest ENSDF compilation (1995)[2].	16

2.1	Diagrammatic representation of a generalized reaction between two nuclei. Let us define the following: M_1 is the incident particle, M_2 is the target particle, M_3 is the light recoil particle and M_4 is the heavy recoil particle, E_1 is the beam energy, E_3 is the light recoil particle energy and E_4 is the heavy recoil particle energy. The lab angles ψ and ζ may be greater than 90° , which is the case for inverse kinematics. Diagram from Nuclear Reaction Analysis Graphs and Tables by J.B. Marion & F.C. Young[22]	20
2.2	Shown[23] is a diagram of the shell structure for the first few shells. On the left are the shells without taking the spin-orbit term into account, and on the right are the levels after spin-orbit coupling is accounted for.	22
2.3	The parameter V_0 , the real well depth of the outgoing ($t+^{18}\text{Ne}$) optical potential was varied over a range of 100 - 140 MeV (Red) to study the effect on the shape of the angular distribution. Varying this parameter had very little effect on the cross section and no effect on the shape of the distribution. A calculation using the original value listed in Falk et al set 4[9] is also shown (Blue).	28
2.4	The parameter r_0 , the real radius of the outgoing ($t+^{18}\text{Ne}$) optical potential was varied over a range of 0.95 - 1.55 fm to study the effect on the shape of the angular distribution. Varying this parameter had very little effect on the cross section and no effect on the shape of the distribution. A calculation using the original value listed in Falk et al set 4[9] is also shown (Blue).	29
2.5	The parameter a_0 , the real well diffuseness of the outgoing ($t+^{18}\text{Ne}$) optical potential was varied over a range of 0.45 - 0.85 fm to study the effect on the shape of the angular distribution. Varying this parameter had very little effect on the cross section and no effect on the shape of the distribution. A calculation using the original value listed in Falk et al set 4[9] is also shown (Blue).	29

2.6	The parameter W_v , the imaginary well depth of the outgoing ($t+^{18}\text{Ne}$) optical potential was varied over a range of 30 - 70 MeV to study the effect on the shape of the angular distribution. Varying this parameter had very little effect on the cross section and no effect on the shape of the distribution. A calculation using the original value listed in Falk et al set 4[9] is also shown (Blue).	30
2.7	The parameter r_v , the imaginary radius of the outgoing ($t+^{18}\text{Ne}$) optical potential was varied over a range of 1.40 - 1.90 fm to study the effect on the shape of the angular distribution. This parameter was only lowered, as a value of $r_v = 1.90$ fm is already large. Though the shape is still identifiable as an L=0 transfer, varying this parameter had a significant effect on the cross section. A calculation using the original value listed in Falk et al set 4[9] is also shown (Blue).	30
2.8	The parameter a_v , the imaginary well diffuseness of the outgoing ($t+^{18}\text{Ne}$) optical potential was varied over a range of 0.45 - 0.85 fm to study the effect on the shape of the angular distribution. Varying this parameter had a significant effect on the cross section, but little effect on the overall shape of the angular distribution. A calculation using the original value listed in Falk et al set 4[9] is also shown (Blue).	31
2.9	The parameter W_D , the surface imaginary well depth of the outgoing ($t+^{18}\text{Ne}$) optical potential was varied over a range of 30 - 70 MeV to study the effect on the shape of the angular distribution. The general shape of the angular distribution stays the same over the range of parameters used, though there are differences between the feature heights of the first and second minimum. A calculation using the original value listed in Falk et al set 4[9] is also shown (Blue).	31

2.10	Comparison of Falk set 4[9] which are the base parameters used in Figures 2.3 - 2.9 and Park et al[10], the parameters used for the DWBA calculations shown in Chapter 5. Though there are differences in relative feature height, both calculations exhibit the same features: a first minimum at around 20° and a second minimum at around 50°	32
3.1	Pumping schematic for the JENSA system as configured at Oak Ridge National Laboratory and the present work. Vacuum pump specifications are listed in Table 3.1, and aperture specifications for U4 through D4 are listed in Table 3.2. Figure from Chipps et al[11]	35
3.2	Image of the central JENSA chamber, and cross section of the JENSA Laval nozzles.	37
3.3	Photograph of the setup for the nozzle tests performed at the NSCL. The source, nozzle, reciever and detector are all pictured.	41
3.4	Diagramatic representation of the setup for the NSCL jet density tests. Distances between the source, target and detector are all shown. The tests at ORNL used a similar setup, but relative distances were different. Figure courtesy of Konrad Schmidt.	41
3.5	Cartoon showing the “projection” of the jet on the superORRUBA segmented silicon detector through the density tests. Figure courtesy of Konrad Schmidt.	42
3.6	A typical result from both the ORNL and NSCL JENSA jet density tests. A linear increase in α -particle energy loss (and therefore jet density) can be seen for tests at both laboratories. The ORNL result shown is for the specific case for α -particle energy loss over the central 2 mm of jet through a ^{Nat}He target at 200, 300, and 400 psi with nozzle A. The NSCL result shown is for the specific case for α -particle energy loss in the central 2 mm of the jet through a ^{Nat}He target at 150, 250, and 350 psi with nozzle A.	42
3.7	Single YY1 detector schematic, used in SIDAR. Drawing from Micron Semiconductors Ltd UK product catalogue[14]	45

3.8	Photograph showing the mount used for SIDAR in the “lampshade” configuration. There are 6 slots for detectors, which are tilted by 43° degrees towards the beamline. Two are shown. (Photograph courtesy of Kelly Chipps.) . . .	45
4.1	The experimental setup for this measurement. (b) has been annotated to show the beam direction, target location and light recoil trajectory	48
4.2	Energy distribution of tritons from the $^{20}\text{Ne}(p,t)^{18}\text{Ne}$ reaction at 30° with a 37.0 MeV proton beam. Triton energies are labeled with the excitation energy of the state they correspond to.	50
4.3	ΔE vs E plot of strip eight in telescope 1 for set of runs 1 and 2. The locations of the clusters of counts, representing particles corresponding to states from (p,t) reaction channels, is shifted over the two sets of runs. This means that the sets have to be calibrated individually to facilitate combining these sets of runs. See Figure 4.4 for an example of uncalibrated data being combined.	51
4.4	Figures 4.3a and 4.3b combined. Location of the tritons corresponding to the ground state of the $^{20}\text{Ne}(p,t)^{18}\text{Ne}$ reaction channel have been circled in red. Both groups of particles represent the ground state tritons, but because these data are uncalibrated, they are in different locations on the ΔE vs E plot. . .	52
4.5	Particle identification plot with the proton, deuteron and triton kinematic lines labeled.	53
4.6	Demonstration of the gating procedure. A line is drawn around the triton line, and in the analysis code this region is used as gate for triton events. The red line representing the gate in this image is much larger than the actual gates used and is that way only to assist the reader. The lines comprising the gates have been enlarged to better display the gate.	54
4.7	Raw counts of ground state tritons from the $^{20}\text{Ne}(p,t)^{18}\text{Ne}$ reaction channel, from run set 2, over strips 9 - 15 from all three telescopes. It can be seen that while telescope 2 and 3 are in good agreement with each other, there is a clear discrepancy with the raw counts in telescope 1. This is due to the fact that the outer strips of telescope 1 was shadowed slightly by the JENSA receiver.	55

4.8	Results from the ΔE solid angle run. Telescope 2 was shadowed between strips 10 and 15, and telescope 1 was shadowed slightly for the last 3 strips, potentially due to an off-axis source position. There is good agreement between all three telescopes at lower angles. It is also important to note that these values vary slightly with the values in Table 4.4, because the ΔE detectors were not at the same location as the E detectors and therefore had a slightly different solid angle coverage. The difference is accounted for by including the standoff distance between the ΔE and E detectors.	57
4.9	Residuals for the ground state of ^{18}Ne . The residuals are scattered around zero	58
4.10	The residuals for the first excited state in ^{18}Ne ($E_x = 1887$ keV). The offset of all points from zero in the same direction indicates a disagreement with literature values for this excitation energy of this state.	59
4.11	Kinematic calculators for tritons from the 2nd excited state in ^{18}Ne (Blue) and the first excited state in ^{12}N (Red). Across the range of angles studied, the behavior is approximately linear. Linear fits were performed on these points and are displayed as lines. The parameters of the fits are given in Table 4.9.	63
4.12	The extracted channel locations of tritons identified from the 2nd excited state in ^{18}Ne (Blue) and the first excited state in ^{12}N (Red and Green). Linear fits were performed through the extracted points and are shown as lines on the figure. The difference between the green and red points arises from the two points at approximately 45° and 47° . These peaks were identified as shoulders, and two fits were performed, one ignoring the shoulder points (Red) and one including them (Green). This resulted in a slight difference in crossing point (See Table 4.10).	64
4.13	This is a single fit for strip 14 over the entire range shown by the red fit line.	67
4.14	This is the entire fit for strip 10, with the individual component gaussians shown along the length of the entire fit. These were added post-fit and are just representative of the constituents of the fit. Background in these display curves is not modeled accurately, while it is in the actual fit. The thin vertical black lines are representative of states in ^{18}Ne , ^{12}N and ^{14}O in current literature.	68

4.15	A segment of the fit used for strip 6. The red line is the line fit over the entire range, while the blue, green and pink lines represent constituents of the overall fit. These were generated post-fit and are only to guide the eye as to the constituents of the doublets and how they were fit individually. Background estimations shown in these fits is not representative of the background estimations in the actual fit (red line). X axis is channel number, where 1 channel is approximately 5 keV, Y axis is counts per bin	69
4.16	The 15 raw triton spectra of strips 1 through 15, used to extract excitation energies and peak integrals used in the analysis of this work. For all plots, the y-axis is number of counts, and the x-axis is channel number (approximately 5 keV per channel), with smaller triton energies corresponding to lower excitation energies.	72
5.1	Angular distribution for the ground state of ^{18}Ne . The locations of maxima and minima in the distribution agree well with the DWBA calculation, but the relative heights of the features differ at higher angles. Also shown are triton distributions from Nero et al[8] and Falk et al[9], and a second L=0 DWBA calculation performed with $E_{beam}=42$ MeV.	76
5.2	Angular distribution of the $E_x = 1887$ keV state. Previous work and mirror arguments constrain the assignment to $J^\pi = 2^+$ therefore only an L=2 transfer was explored for this state. The calculation has a distinctive structure, while the angular distribution is significantly flatter. The trend of the distribution extracted from these data tend to agree with the position of the features, the trough between 30° and 40° and the peak between 40° and 50° . The shape of the triton angular distribution in the present work agrees with the studies performed by Falk et al[9] and Nero et al[8]. A DWBA calculation performed with $E_{beam} = 42$ MeV is also presented for better comparison between these data and previous work.	78

5.3	Angular distribution of tritons corresponding to the $E_x = 3376$ keV state in ^{18}Ne . There are larger error bars on the points between 30° and 40° due to the subtraction of ^{12}N background, as discussed in Section 5.3. Only L=4 transfer was explored for this state. The extracted distribution is mostly flat while the DWBA calculation for an L=4 transfer shows distinctive features, though these data agrees well with previous work.	79
5.4	Angular distribution for the $E_x = 3576$ keV state. Only an L=0 transfer was explored for this state as previous work has constrained the assignment to $J^\pi = 0^+$. The present study, Nero et al[8] and the DWBA calculation for an L=0 transfer are all in agreement.	80
5.5	Angular distribution for the $E_x = 3616$ keV state. Only an L=2 transfer was explored for this state. At lower angles, there are differences between calculation and the angular distribution while at angles above 35° calculation and these data agree in feature location and relative feature height. There is reasonable agreement at lower angles between these data and Nero et al[8]	81
5.6	Angular distribution of the $E_x = 3600$ keV doublet fit as a single state. This state corresponds to an excitation energy of $E_x = 3589 \pm 12$ keV. The distribution is mostly featureless, appearing flat at lower angles with a downward trend past 30°	83
5.7	Angular distribution for the $E_x = 4520$ keV state. L=0,1,2,3 and 4 transfers were all explored for this state, with the two lowest χ^2 values, L=1 and L=4, shown alongside these data. The DWBA calculation for an L=1 transfer agrees very well with these data over the observed angular range. Both calculation and these data follow the same shape, with only slight disagreement in relative feature height at 60° . There is significant disagreement between Falk et al[9] and both these data and Nero et al[8]. This is due to the distribution from Falk et al[9] containing tritons from both the $E_x = 4520$ keV and $E_x = 4590$ keV states being incorrectly attributed to only the $E_x = 4520$ keV state.	84

5.8	Comparison of data from Falk et al[9], Nero et al[8] and these data for the multiplet at $E_x \approx 4500$. Falk et al[9] saw only a single peak, but it had multiple constituents which were completely resolved in both these data and Nero et al[8]. These individual components were summed together for comparison with data from Falk et al[9] in this figure.	85
5.9	Angular distribution for the $E_x = 4590$ keV state. L=0,1,2,3 and 4 transfer were all explored for this state and the two lowest χ^2 , DWBA calculations for L=0 and L=4 transfers are shown. These data and the L=0 calculation are in very good agreement, with the presented distribution replicating both relative feature height and location over the angular range studied in the present work. The general trend of the distribution from Nero et al[8] agrees over most overlapping angles with respect to these data.	86
5.10	Angular distribution for the $E_x = 5090$ keV state. All possible L-transfer were explored for this state. DWBA calculations for L=2 and L=3 transfers are shown alongside these data, because of previous assignments to this state. The transfers with the two lowest χ^2 values are also shown. At lower angles, this combined distribution is featureless and flat, with a small bump at around 35° the extracted distribution appears flat, with larger variations in the differential cross section appearing at higher angles. The value presented from this work was adopted from Nero et al[8]	88
5.11	Angular distribution for the $E_x = 5146$ keV state. All possible L-transfer were explored for this state. DWBA calculations for L=2 and L=3 transfers are shown alongside these data, because of previous assignments to this state. The transfers with the two lowest χ^2 values are also shown. The angular distribution is mostly flat for the $E_x = 5146$ keV state. The lower angle structure compares favorably with an L=4 transfer, though the distribution from Park et al[10] is significantly flatter than these data, indicating difficulties separating the two constituent states of the single peak.	90

5.12	Angular distribution of the $E_x = 5090$ keV and $E_x = 5146$ keV doublet fit as a single peak. The angular distribution appears mostly featureless, with a small bump at around 35° . This single peak corresponds to $E_x = 5130 \pm 12$ keV. There is good agreement between these data and Park et al[10] across all angles covered in the present work, and a slight disagreement between Falk et al[9], these data and Park et al[10] at lower angles.	91
5.13	Angular distribution for the $E_x = 5450$ keV state. L=0,1,2,3 and 4 transfer were all explored for this state. The distribution shows a slow decline from 20° to 45° with a minima at 45° , then an increase in differential cross section at angles between 45° to 60° . This is well described by DWBA calculations for an L=3 transfer. The relative height of features suggest that L=3 better agree with these data than L=0.	92
5.14	Angular distribution for the $E_x = 6150$ keV state, shown alongside DWBA calculations for L=1, L=3, and L=4 transfer. DWBA calculations for an L=3 or L=4 are the lowest χ^2 when compared to the extracted distribution, and the L=1 transfer calculation is shown because of the abundance of previous studies assigning this state a $J^\pi = 1^-$. Mirror arguments also constrain the possible L transfer to L=1, L=3 or L=4 with the assumption of S=0. The structure of the extracted angular distribution does not agree with an L=1 transfer, but is much more compatible with an L=3 transfer.	93
5.15	Angular distribution for the $E_x = 6297$ keV state shown alongside DWBA calculations for an L=1, L=3 and L=4 transfer, chosen because of mirror nucleus constraints and low χ^2 values. An L=3 transfer calculation seems to describe the presented distribution well. The distribution presented in Falk et al[9] compares well to the distribution from these data.	95
5.16	Angular distribution for the $E_x = 6353$ keV state shown alongside DWBA calculations for an L=1, L=3 and L=4 calculation, chosen because of mirror nucleus constraints and low χ^2 values. The distribution for this state does not show any pronounced features across the measured angular range.	97

5.17	Angular distribution of the $E_x = 6297$ keV and $E_x = 6353$ keV doublet fit as a single peak. The excitation energy of this single peak corresponds to $E_x = 6315 \pm 11$ keV. Previous work indicates two states at this energy, therefore this combined distribution is expected to be flatter than that of a single state, with less pronounced features. There are no defining features aside from a small bump at around 55°	98
5.18	Raw counts vs channel plot with three labeled previously observed states and a potential new state as detected at 27.5° in the center of mass. This state corresponds to $E_x = 5309 \pm 13$ keV	98
5.19	Raw counts vs channel plot with three labeled previously observed states and a potential new state as detected at 32.5° in the center of mass. This state corresponds to $E_x = 5309 \pm 13$ keV	99
5.20	Angular distribution of the triton peak observed at $E_x = 5309 \pm 13$ keV shown alongside DWBA calculations for L=0 through L=4 transfers.. . . .	99

Chapter 1

Introduction

1.1 Astrophysics

Astrophysics is the study of objects in the cosmos and the phenomena we see out in space, including the life cycle of stars, the formation of galaxies, and X-ray bursts. Since we cannot travel to directly study these phenomena, the next best thing is to study the mechanisms we believe to be involved in these stellar events here on Earth, and see how they apply to our observations of space. The evolution of astrophysical phenomena depends on a number of properties, some that we cannot directly measure, such as the isotopic abundances in the specific environment. However, some of these intrinsic properties depend on quantities we can measure in the laboratory, such as the reaction rate of a particle pair of nuclei or the spin-parity of a state. For this purpose, we use transfer reactions, which are a powerful tool in nuclear structure studies, and have been used for decades to probe the properties of nuclei.

1.1.1 Stellar evolution

Stars are fueled by nuclear fusion, generating energy by burning hydrogen via the proton-proton (p-p) chain and the carbon-nitrogen-oxygen (CNO) cycle. When most of the hydrogen is burned up, helium becomes the primary constituent of the core. At this point, the star begins gravitational contraction until hydrogen outside of the core ignites. Energy generated outside of the core is more easily lost, and as a result the outer layers of the star expand. The

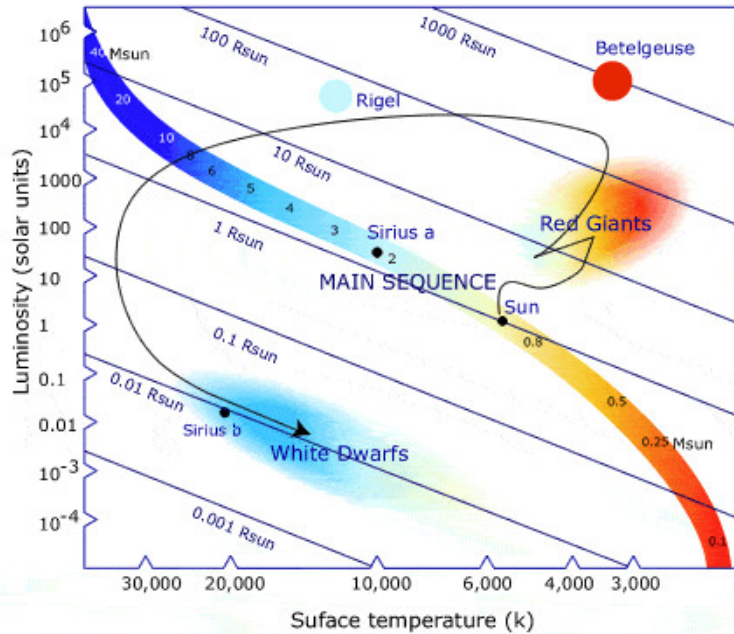


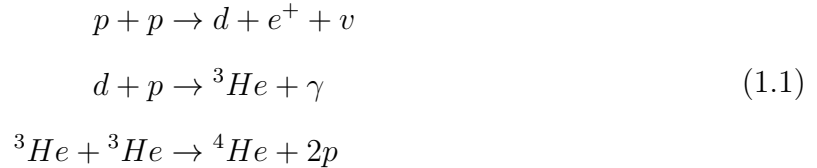
Figure 1.1: A Hertzsprung-Russell (HR) diagram[17] with the life cycle of a star like our Sun mapped on it. HR diagrams show stellar luminosity (Energy emitted per unit time). Most observable stars ($\sim 90\%$) lie on the main sequence, and stars typically spend around 90% of their life on the main sequence.

star becomes brighter, larger and cooler; stars at this stage are red giants. The star’s core temperature continues to increase as the surface expands and cools, becoming hot enough in the core for helium burning to ignite. What happens at this point depends entirely on the mass of the star. Stars with masses up to $10 M_{\odot}$ ($M_{\odot} = 1$ solar mass = 2×10^{30} kg, the mass of the Sun) are thought to eject their outer layers as planetary nebulae. This leaves the core to cool, becoming a white dwarf star. Stars above $10 M_{\odot}$ continue burning beyond helium burning, forming heavier elements all the way up to iron, at which point the massive star explodes in a Type II supernova explosion where the star is destroyed, aside from potentially leaving a highly dense core behind, in the form of a black hole or a neutron star. The life cycle of a typical Sun-like star is shown in Figure 1.1.

1.1.2 Hydrogen fusion

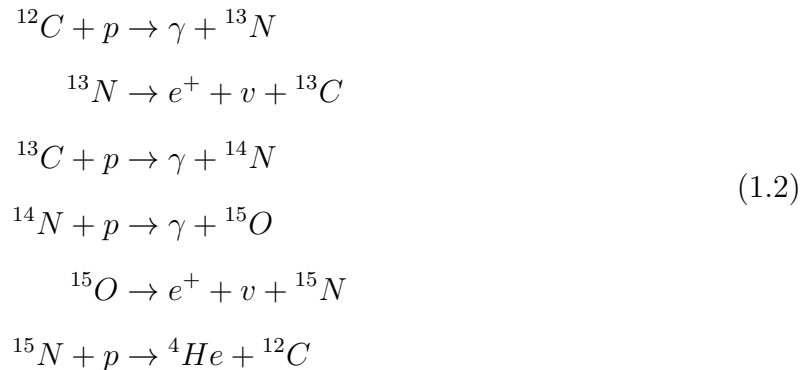
The fusion of hydrogen into helium occurs via the proton-proton chain. There are multiple p-p chains. Which of these is the dominating mechanism depends on the temperature of the

environment. In environments below 8 MK, the p-p chain stops at ${}^3\text{He}$. This accounts for around 90% of main sequence stars within around 15 light years of the Sun and can be seen in Equation 1.1:



1.1.3 The CNO cycle

Carbon, nitrogen and oxygen provide another mechanism for stellar environments to turn hydrogen into helium. This cycle switches on at temperatures around 15 MK, and becomes the dominant source of energy generation around 17 MK. The CNO-I cycle is shown in Equation 1.2

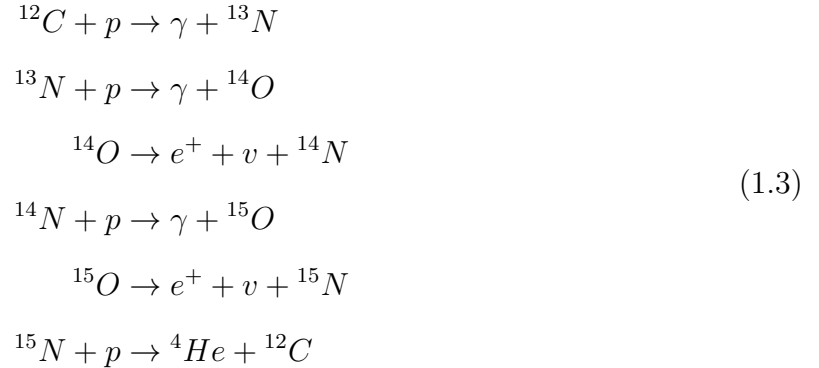


This cycle ends with exactly the same results as at p-p I chain, namely the conversion of 4p into ${}^4\text{He}$, the ${}^{12}\text{C}$ acting as a catalyst for the production of ${}^4\text{He}$. The CNO cycle accounts for approximately 1.5% of the energy generation in the Sun, as the p-p chain dominates at the Sun's core temperature of approximately 15 MK.

1.1.4 The hot CNO cycle

As temperatures increase into much hotter astrophysical phenomena, of the order 1GK, far above the temperatures where the CNO and p-p chain dominate, the CNO cycle continues

to operate, but nuclei which undergo β -decay, such as ^{13}N , can be used up before the β -decay occurs, as reactions happen much faster in these much hotter stellar environments. Reactions on ^{13}N start to occur on the same time scale as the β -decay of ^{13}N . In this hot-CNO cycle, hydrogen to helium conversion rates are limited by the lifetimes of ^{14}O and ^{15}O . The hot-CNO I cycle (See Figure 1.3) is shown in Equation (1.3):



1.1.5 Binary stars and X-ray binaries

A binary star system consists of two stars orbiting around the center of mass of the system. There are multiple types of binary star systems, but the present work is concerned with the specific case where one of the stars is a main sequence star and the other is a neutron star, also referred to as an X-ray binary, owing to the observation of X-rays produced.

1.1.6 X-ray bursts

There are two distinct types of X-ray bursts, Type I and Type II. Type I are the focus of this work, and are characterized by regular burst recurrence and typical burst profile consisting of a sharp rise in X-ray emission, followed by a slow trail off. Type II X-ray bursts are irregular and have have much sharper burst profile, cutting out suddenly with no trail off.

As the main sequence star swells and becomes a red giant, material pushes past the star's Roche limit (Figure 1.2), the limit in which material is gravitationally bound to the star. As the material pushes past this boundary, it can extend into the Roche limit of the partner neutron star and begin accreting onto the surface of the neutron star. This accreted hydrogen and helium collects on the surface over a period of hours to days. In

these extremely high temperature and pressure environments, the accreted material begins to undergo thermonuclear runaway via breakout of the hot CNO cycle.

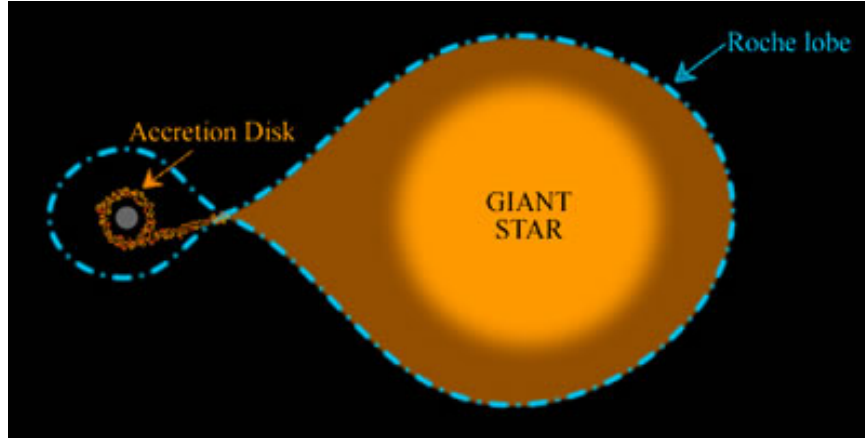


Figure 1.2: A main sequence star evolves into a red giant, causing material to push past the limit Roche limit, where material is gravitationally bound to it. The binary partner, in the case for Type-I X-ray bursts a neutron star, accretes this material[18].

Type I X-Ray bursts are thought to occur in X-ray binary star systems. The hot-CNO cycle is rate limited by the β -decay of ^{14}O and ^{15}O , so any possible reaction that provides a reaction path away from ^{14}O or ^{15}O can cause “breakout” from the hot-CNO cycle (See Figure 1.3). The rate limiting factor in the hot-CNO cycle happens at ^{14}O and ^{15}O . The following process:



provides a path to transition from ^{14}O to ^{15}O , and:





provides a path to breakout from the hot-CNO cycle into the rapid proton capture process (rp-process)[16].

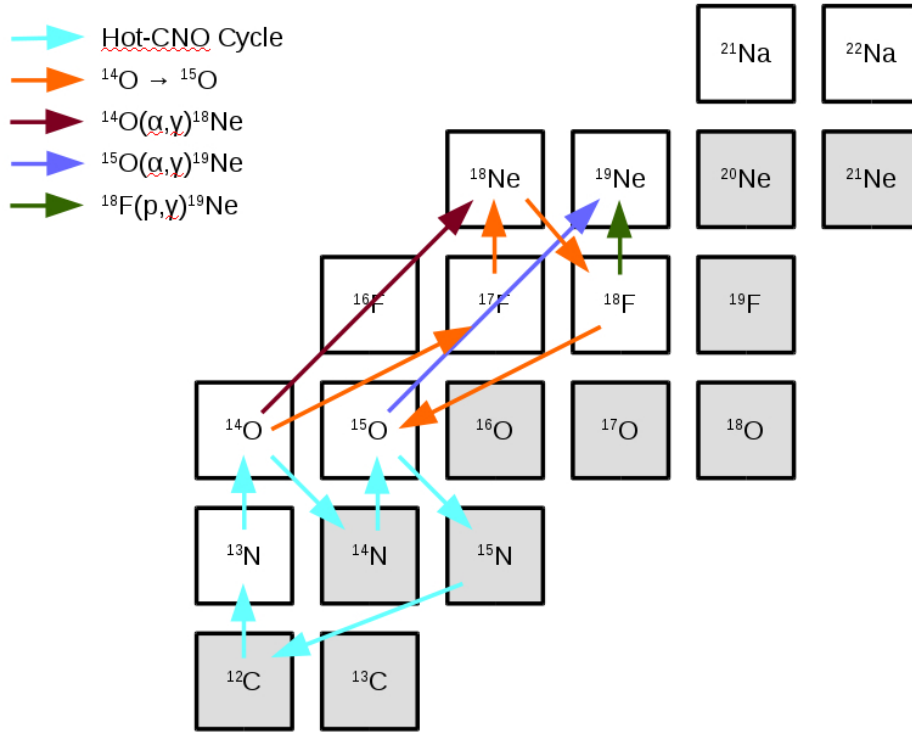


Figure 1.3: Diagram showing the HCNO-I cycle (Light Blue), the path to transition ${}^{14}\text{O}$ to ${}^{15}\text{O}$ (Orange), and three potential hot-CNO breakout mechanisms (Red, Dark Blue and Green).

1.1.7 rp-process

Stellar nucleosynthesis can only produce elements up to iron. We know via observations that elements heavier than iron are produced in the universe, and one possible way is through the rapid proton capture process (rp-process). A much faster mechanism to burn hydrogen is

opened up in the explosive conditions generated as material is accreted onto a neutron star. The rapid proton capture process is a series of rapid proton captures and β -decays along the proton drip line, the line above which nuclei are energetically unbound[20]. Figure 1.4 shows an example of an rp-process path for an X-ray burst.

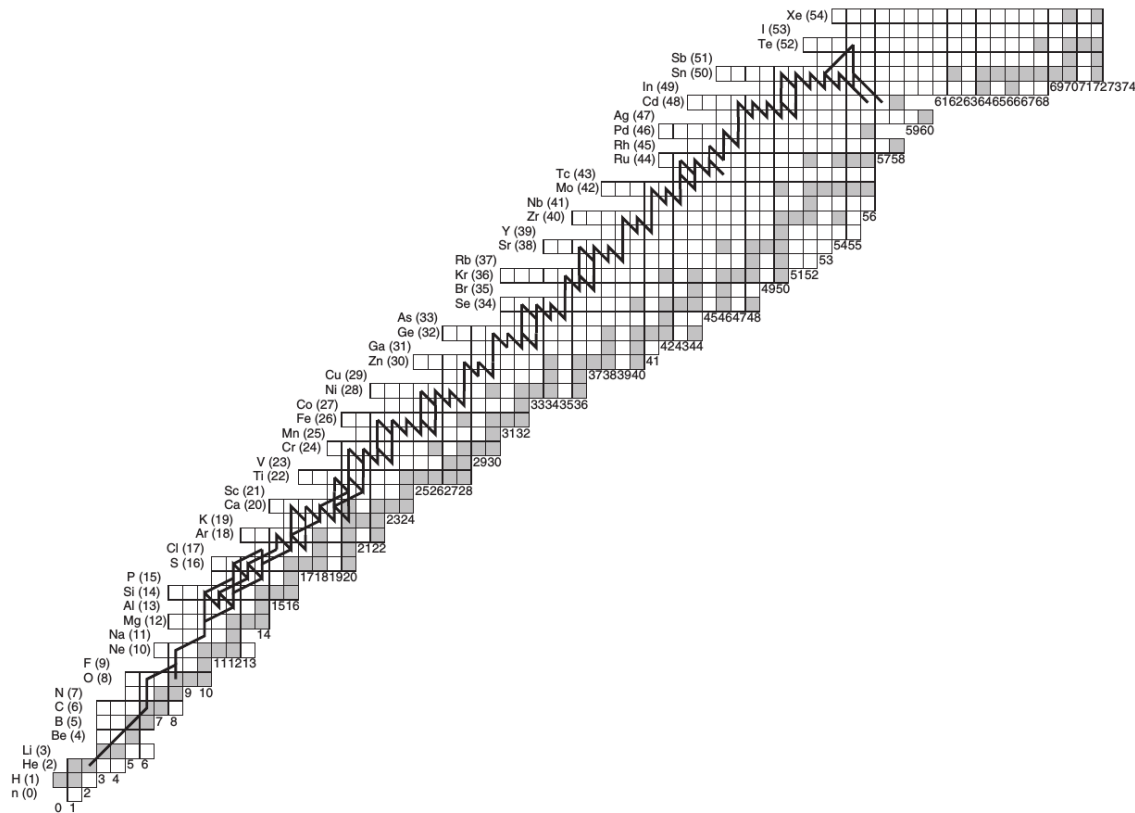


Figure 1.4: The maximum extent of the rp-process path reached for a long, hydrogen-rich burst. In this explosive nucleosynthesis, nuclei pass through a rapid chain of proton captures and β -decays, generating energy two orders of magnitude faster than typical nucleosynthesis (Such as the p-p chain)[19]. Figure from Langanke and Schatz[20]

1.2 Stellar reaction rates

Stellar reaction rates are important to understand how processes evolve in stellar environments, and predict element production and energy generation. Isotopic abundances are altered through production channels (how an isotope is produced), and destruction channels (how an isotope is transmuted into a different isotope). With knowledge of reaction rates, we

can understand how isotopic abundances change over time, and in turn understand energy production over time, which gives us insight into the ignition of supernovae and X-ray bursts.

The stellar reaction rate per particle pair for a narrow resonance is given by Equation (1.7)[24]:

$$\langle \sigma v \rangle = \left(\frac{2\pi}{\mu kT} \right)^{\frac{3}{2}} \hbar^2 (\omega \gamma) \exp\left(-\frac{E_1}{kT}\right) f, \quad (1.7)$$

Where:

- $\mu = \frac{M_1 M_2}{M_1 + M_2}$ = reduced mass of the interacting particle pair
- k = Boltzmann's constant
- T = environment temperature (K)
- \hbar = reduced Planck constant
- E_1 = energy of the resonance
- f = electron screening factor

γ is the ratio of the partial widths of possible decay modes (Γ_a and Γ_b) to the total width ($\Gamma = \sum_i \Gamma_i$):

$$\gamma = \frac{\Gamma_a \Gamma_b}{\Gamma}, \quad (1.8)$$

The total width of a state is related to the lifetime of the state (τ) by $\Gamma = \frac{\hbar}{\tau}$. ω is the statistical factor, given by:

$$\omega = \frac{2J + 1}{(2J_1 + 1)(2J_2 + 1)} (1 + \delta_{12}) \quad (1.9)$$

J_1 , J_2 and J refer to the angular momentum of the state in the projectile, the target and the sum of the projectile and target nuclei, the compound nucleus, respectively. The parameter δ_{12} represents the cross section increasing by a factor of two when both particles are identical in the entrance channel. The combined $\omega \gamma$ factor is referred to as the resonance strength. The stellar reaction rate therefore depends on a number of experimentally measurable resonance parameters: the energy of the resonance, the angular momentum, and widths of the particles and states involved.

The present work intends to constrain the spin-parities of states in ^{18}Ne , which are used to calculate the statistical factor ω in reaction rate calculations of $^{14}\text{O}(\alpha, p)^{17}\text{F}$. Constraining

parameters involved in calculations of sensitive reaction rates is vital for the accuracy of astronomical models.

1.2.1 Gamow window

Two-body reaction rates depend primarily on two energy-dependent factors: the velocity distribution of the particles, and the tunneling probability a particle has to overcome due to the Coulombic repulsion of the two particles. The Gamow window is the energy window where the overlapping of these two factors results in a region of significantly increased reaction probability. The effective mean energy of the Gamow window is given by[24]:

$$E_0 = 1.22(Z_1^2 Z_2^2 \mu T_6^2)^{\frac{1}{3}} \quad (1.10)$$

Z = proton number

T_6 = temperature in units of 1 MK

and the effective width of the energy window is:

$$\Delta = 0.749(Z_1^2 Z_2^2 \mu T_6^5)^{\frac{1}{6}} \quad (1.11)$$

Combining these two gives the Gamow window:

$$E = E_0 \pm \frac{\Delta}{2} \quad (1.12)$$

The Gamow peak E_0 represents the location where the cross section is at a maximum, and the Gamow window represents the range of energies where most reactions occur.

1.3 ^{18}Ne and hot-CNO breakout

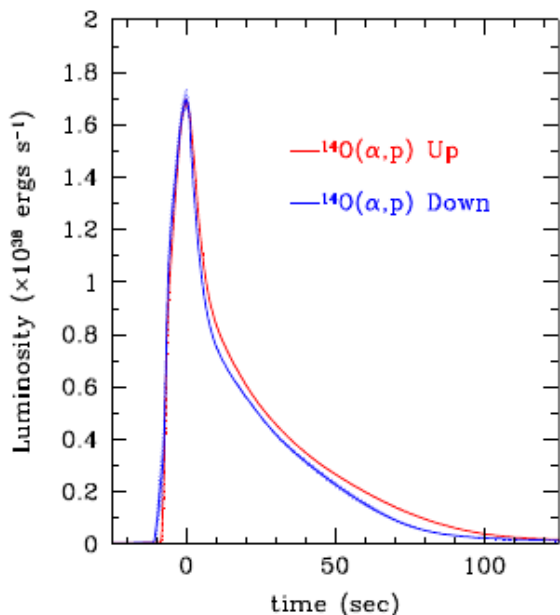
As mentioned earlier, type I X-ray bursts are thought to originate in binary star systems consisting of a neutron star and a main sequence star. Material, mainly hydrogen and helium, is accreted onto the neutron star from its partner star. As material continues to

accrete, fusion begins in the hot-CNO cycle due to the extreme temperature and pressure environment. Breakout from the hot-CNO cycle into the rp-process can occur via the reaction $^{14}\text{O}(\alpha, \text{p})^{17}\text{F}$ (Figure 1.3 and Equation 1.6), therefore playing a part in triggering Type I X-ray bursts. The stellar reaction rate of a particle pair (Equation 1.7) is dependent on the temperature of the environment T , resonance strength $\omega\gamma$. In turn, the resonance strength depends on two factors relating to the final state in the compound nucleus ^{18}Ne , the fusion product of $^{14}\text{O} + \alpha$: E_1 , the energy and J , the angular momentum. Thus, measuring the excitation energy E_x and angular momentum J of states in ^{18}Ne will aid calculations of the reaction rate of $^{14}\text{O}(\alpha, \text{p})^{17}\text{F}$. The isotope ^{18}Ne plays an important role in the hydrogen burning process in two ways, as the compound nucleus in $^{14}\text{O}(\alpha, \text{p})^{17}\text{F}$ and the product of $^{17}\text{F}(\text{p}, \gamma)^{18}\text{Ne}$.

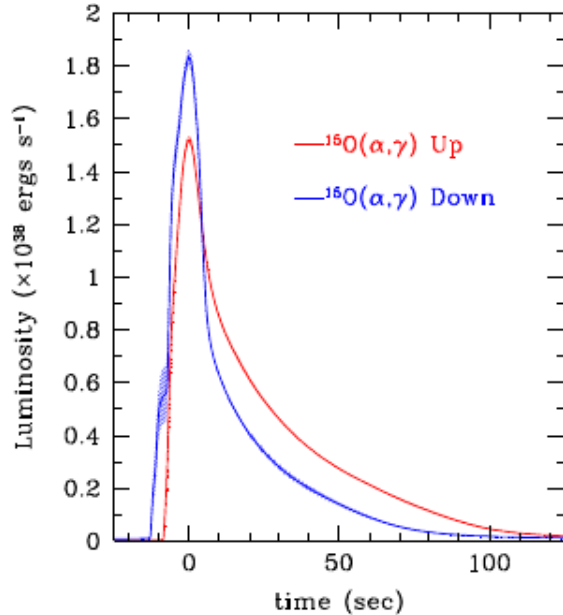
Studies[6, 25] have shown that alpha capture on ^{14}O and ^{15}O happens at a comparable rate to β -decay at temperatures typical in Type-I X-ray bursts, between 0.1 and 1 GK. Considering that the α -threshold in ^{18}Ne lies at $Q_\alpha = 5114$ keV, states in ^{18}Ne above this threshold can affect the reaction rate of $^{14}\text{O} + \alpha$. A recent sensitivity study, Cyburt et al[21], showed that current type I X-ray burst models are sensitive to the reaction rates of $^{14}\text{O}(\alpha, \text{p})^{17}\text{F}$ and $^{15}\text{O}(\alpha, \gamma)^{19}\text{Ne}$. These reaction rates were varied up and down by a factor of 10. Simulated light curves (the change in luminosity over time) showing reaction rate sensitivity for these reactions are shown in Figure 1.5. While the reaction rate of $^{14}\text{O}(\alpha, \text{p})^{17}\text{F}$ does not have a significant effect on the light curve (Figure 1.5a) when compared to the effect of the $^{15}\text{O}(\alpha, \gamma)^{19}\text{Ne}$ (Figure 1.5b) reaction rate, it is still significant when compared to most of the other reaction rate variations performed in the sensitivity study. The reaction rates of $^{14}\text{O}(\alpha, \text{p})^{17}\text{F}$ and $^{15}\text{O}(\alpha, \gamma)^{19}\text{Ne}$ also affect the burst recurrence rate. Decreasing the reaction rate by a factor of 10 decreased recurrence time by 7% in the case of $^{14}\text{O}(\alpha, \text{p})^{17}\text{F}$ and 11% in the case of $^{15}\text{O}(\alpha, \gamma)^{19}\text{Ne}$ [21].

1.3.1 Previous studies

The first study of states in ^{18}Ne was reported in 1961 by Towle and Macefield[26] through the $^{16}\text{O}(^3\text{He}, \text{n})^{18}\text{Ne}$ reaction. This study reported 3 excited states in ^{18}Ne , $E_x=1880\pm 10$ keV, 3362 ± 11 keV, 3608 ± 12 keV. Utilizing the same reaction, R.D Gill et. al[1], with a follow



(a) The affect of varying the $^{14}\text{O}(\alpha,\text{p})^{17}\text{F}$ reaction rate on the X-ray burst light curve. While the variation between light curves is small in comparison with Figure 1.5b, it is still a significant effect when compared with variations of other reaction rates in the Cyburt et al[21] sensitivity study. The reaction rate of $^{14}\text{O}(\alpha,\text{p})^{17}\text{F}$ does have an effect on the recurrence rate of Type I X-ray bursts. Figure from Cyburt et al[21].



(b) The affect of varying the $^{15}\text{O}(\alpha,\gamma)^{19}\text{Ne}$ reaction rate on the X-ray burst light curve. According to Cyburt et al[21], the reaction rate of $^{15}\text{O}(\alpha,\gamma)^{19}\text{Ne}$ significantly affects both the light curve and X-ray burst recurrence times. Figure from Cyburt et al[21].

Figure 1.5: Cyburt et al[21] investigated the sensitivity of current X-ray burst models by varying 96 different reaction rates. Light curves when varying reaction rates of $^{14}\text{O}(\alpha,\text{p})^{17}\text{F}$ and $^{15}\text{O}(\alpha,\gamma)^{19}\text{Ne}$ by a factor of 10 both up and down are shown. Both Figures are from Cyburt et al[21]

up paper in early 1969[27], studied excited states in ^{18}Ne . The values reported are shown in Table 1.1. These excitation energies were extracted by studying the Doppler-corrected γ -ray energies from $^{18}\text{Ne}^*$ de-exciting to the ^{18}Ne ground state.

Wiescher et al[6] calculated the structure of ^{18}Ne based on the mirror nucleus ^{18}O . A mirror nucleus is a nucleus with the same mass, but with the proton and neutron numbers reversed. These predictions were used as a good starting point for further studies into the structure of ^{18}Ne [16]. The current evaluated knowledge of states in ^{18}Ne , as listed in the latest Evaluated Nuclear Structure Data File[2] are shown in Table 1.2, while the most recent literature as of October 2017 is compiled in Table 1.3.

Table 1.1: Values for E_x and J_π for $E_x < 4000$ keV states in ^{18}Ne as reported in R.D Gill et. al[1].

E_x (keV)	J_π
1887.3 ± 0.2	2^+
3376.2 ± 0.4	4^+
3576.3 ± 2	0^+
3616.4 ± 0.6	2^+

Table 1.2: Excitation energy (E_x) and spin-parity assignments (J^π) of states in ^{18}Ne as listed on the most recent Evaluated Nuclear Structure Data File (ENSDF)[2]. As of March 2018, the latest compilation including ^{18}Ne was performed in 1995. References are given as listed on ENSDF, with citations of the individual papers which comprise the list and corresponding reaction studied.

A: ^{18}Ne β^+ -decay[3, 4] B: $^{12}\text{C}(^{12}\text{C},^6\text{He})$ [2] C: $^{14}\text{O}(\alpha,\gamma)$ [2] D: $^{16}\text{O}(^3\text{He},n)$ [5, 3, 6] E: $^{16}\text{O}(^{10}\text{B},^8\text{Li})$ [2] F: $^{16}\text{O}(^{12}\text{C},^{10}\text{Be})$ [7] G: $^{18}\text{O}(\pi^+,\pi^-)$ [3, 4] H: $^{20}\text{Ne}(p,t)$ [8, 2, 9]

E_x (keV)	J_π	REF
0	0^+	A D GH
1887.3 ± 0.2	2^+	D GH
3376.2 ± 0.4	4^+	DEF H
3576.3 ± 2	0^+	D H
3616.4 ± 0.6	2^+	D H
4519 ± 8	1^-	D H
4561 ± 9	3^+	D
4590 ± 8	0^+	D H
5090 ± 8	$(2^+, 3^-)$	D H
5146 ± 7	$(2^+, 3^-)$	D H
5453 ± 10		H
6150	(1^-)	BC
6297 ± 10	4^+	D H
6353 ± 10		H
7059 ± 10	$(1^-, 2^+)$	D H
7350		B
7713 ± 10		D H
7910 ± 10	$(1^-, 2^+)$	D
7950 ± 10		H
8086 ± 10		D
8500 ± 30		D
9201 ± 9		H

Table 1.3: Current status of the literature regarding excitation energies (E_x) and spin-parity assignments (J^π) of states in ^{18}Ne . There have been other studies focusing on the particle widths of states in ^{18}Ne but those have been omitted for this table as, while important for reaction rate calculations, they are not pertinent to the present study. Values in the leftmost column represent ENSDF[2] listings. As of March 2018, the latest ENSDF compilation including ^{18}Ne was performed in 1995. References are given in chronological order.

E_x (keV), J^π [2]	[16]	[10]	[28]	[29]	[30]	[31]	[32]	[33]	[34]
4519±8, 1 ⁻	4520, 1 ⁻								
4561±9, 3 ⁺	4561, 3 ⁺		4523.7±2.9, 3 ⁺						
4590±8, 0 ⁺	4589, 0 ⁺								
5090±8, (2 ⁺ , 3 ⁻)	5106, (3 ⁻)	5110, 2 ⁺					5100±100		
5146±7, (2 ⁺ , 3 ⁻)	5153, (2 ⁺)	5150, 3 ⁻							
5453±10	5454, 2 ⁻	5467±5							
6150, (1 ⁻)	6150, (1 ⁻)			6150, 1 ⁻	6137, 1 ⁻	6150, 1 ⁻	6150±83	6150±30, 1 ⁻	
6297±10, (4 ⁺)	6286, (4 ⁺)	6305±4		6290, 3 ⁻	6310		6300±47	6280±30, 3 ⁻	
6353±10	6345, (3 ⁻)	6358±5,		6350 2 ⁻	6310			6350±30, 2 ⁻	
							6850±110, (0 ⁻ , 0 ⁺)		
7059±10, (1 ⁻ , 2 ⁺)				7050±100, 4 ⁺	7092	7120, 4 ⁺	7060±39	7050±30, 4 ⁺	
					7050, 2 ⁺				
7350				7370±60, 2 ⁺	7323	7350, 2 ⁺			7350±30, (1 ⁻)
7713±10				7600±50, 1 ⁻	7584	7620, 1 ⁻			7580±20, (0 ⁺)
				7710±50, 2 ⁻					7720±20, (2 ⁺ , 3 ⁻)
7910±10, (1 ⁻ , 2 ⁺)									
7950±10							7950±30		
8086±10							8090±28		8100±100, (0 ⁺)
8500±30									
9201±9									

$^{14}\text{O}(\alpha,\text{p})^{17}\text{F}$

Wiescher et al[6] were the first to calculate that the reaction rate of $^{14}\text{O}(\alpha,\text{p})^{17}\text{F}$ at temperatures pertaining to type I X-ray bursts is dominated by specific resonances. Since then, there have been numerous sensitivity studies[35, 21] which have resulted in various discrepancies. Though the use of different models does play a part in accounting for this, Parikh et al[35] specifically discuss disagreements between Blackmon et al[30] and Hahn et al[16] of a factor of 10 in the $^{14}\text{O}(\alpha,\text{p})^{17}\text{F}$ reaction rate. Variations of a factor of 10 in the reaction rate were large enough to see a shift in total energy production in 5 of the 10 models explored by Parikh et al[35], and they conclude that further efforts should be placed in constraining the $^{14}\text{O}(\alpha,\text{p})^{17}\text{F}$ reaction rate.

Resonant reaction rates depend on the excitation energies, spin-parity assignments, and the partial and total particle widths of states in the compound nucleus of the reaction (Section 1.2). Therefore to understand the reaction rate of $^{14}\text{O}(\alpha,\text{p})^{17}\text{F}$ one needs a deep understanding of states in ^{18}Ne . Each of the aforementioned parameters can be determined experimentally, and as a result there have been extensive studies into states in ^{18}Ne (Refer to Tables 1.3 and 1.2). Even with so much focus on ^{18}Ne , there are still significant discrepancies between studies. Blackmon et al[36] investigated the time-reverse of $^{14}\text{O}(\alpha,\text{p})^{17}\text{F}$, $^1\text{H}(^{17}\text{F},\alpha)^{14}\text{O}$, Notani et al[37] directly studied $^{14}\text{O}(\alpha,\text{p})^{17}\text{F}$ with a 43 MeV ^{14}O beam, reporting a 50% difference in reaction rate with Blackmon et al[36]. Notani et al[37] measured nine resonances above $E_x > 6000$ keV, but statistics were limited this direct study. Later work Changbo Fu et al[38] called into question the assumptions made by Notani et al[37], highlighting difficulties in separation of recoil protons from $^{14}\text{O}(\alpha,\text{p})^{17}\text{F}$.

Both ^{14}O and the α -particle have a ground state with $J^\pi = 0^+$, which means that natural parity levels (discussed later in Section 2.18) are populated in the compound nucleus ^{18}Ne . Only states above the threshold energy of $Q_\alpha = 5114$ keV in ^{18}Ne will contribute to the $^{14}\text{O}(\alpha,\text{p})^{17}\text{F}$ reaction rate. Hahn et al[16] calculated reaction rate contributions from natural parity states above the Q_α threshold in ^{18}Ne and found that there is a significant contribution from a $J^\pi = 1^-$ resonance at $E_x=6150$ keV in ^{18}Ne (the level diagram is shown in Figure 1.6).

Because of the importance of the resonance at $E_x=6150$ keV in reaction rate calculations, this state in particular has been the subject of many studies.

The existence of a state at $E_x=6125$ keV was first predicted by Wiescher et al[6], with a $J^\pi = 1^-$. The state was first seen in a study 9 years later by Hahn et al[16] and tentatively assigned $J^\pi = 1^-$ based on the proximity to the predicted 1^- state. Gomez del Campo et al[39] observed this state in a study of 2-proton emission from states in ^{18}Ne and firmly assigned $J^\pi = 1^-$. Shortly after, Harss et al[29] studied the time inverse reaction, $^{17}\text{F}(p,\alpha)^{14}\text{O}$, and also firmly assigned $J^\pi = 1^-$, based on R-Matrix analysis. The first inelastic scattering measurement to observe this level was performed a year later by Blackmon et al[30], who also make a spin-parity assignment of 1^- , based on R-matrix analysis. Another study adding credence to the 1^- assignment was performed by He et al[31] in 2011, utilizing R-matrix to make a 1^- assignment.

The $E_x=6150$ keV state was widely assumed to be a 1^- state until He et al[40] revisited previous data from Gomez del Campo et al[39] and found a spin-parity assignment of 3^- was a better fit of the data. This study reverses the current knowledge, and changes spin-parity assignments of two neighboring states. The paper claims that the $E_x=6300$ keV state has a spin-parity of 1^- and the $E_x=6150$ keV has a spin-parity of 3^- . They also perform reaction rate calculations, and demonstrate that switching the spin-parity assignments between the closely spaced $E_x=6150$ keV and $E_x=6300$ keV states, as their reanalysis of data suggests may be the case, can alter the resonant reaction rate of $^{14}\text{O}(\alpha,p)^{17}\text{F}$ by an order of magnitude.

$^{17}\text{F}(p,\gamma)^{18}\text{Ne}$

The other breakout reaction from the hot-CNO cycle, $^{17}\text{F}(p,\gamma)^{18}\text{Ne}$, is also dominated by resonances in hot, dense astrophysical environments. Garcia et al found a $J^\pi=3^+$ level in ^{18}Ne 230 keV higher than calculations predicted, at $E_x=4561\pm 9$ keV, and as a result shifted the calculated contribution of that state to the $^{17}\text{F}(p,\gamma)^{18}\text{Ne}$ reaction rate by a factor of approximately 100. A later study by Bardayan et al[41] suggests that the $J^\pi=3^+$ state in the $E_x \approx 4500$ keV region has an excitation energy of $E_x=4523.7\pm 2.9$ keV, and reaction rate calculations performed therein show that this state dominates the $^{17}\text{F}(p,\gamma)^{18}\text{Ne}$ reaction

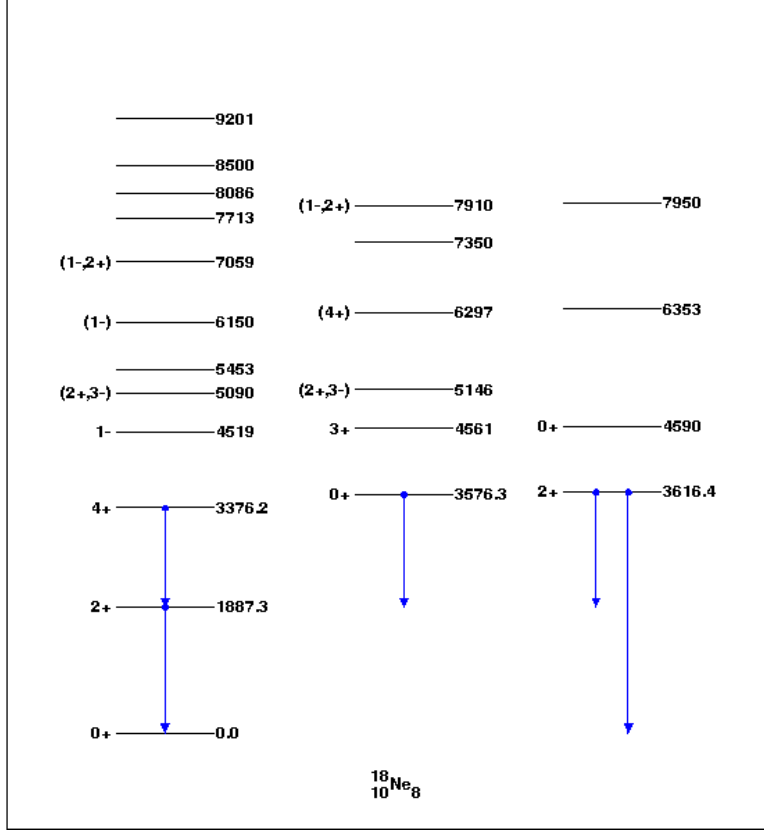


Figure 1.6: Level diagram for ^{18}Ne generated from levels and spin-parity assignments in the latest ENSDF compilation (1995)[2].

rate at temperatures higher than 0.5 GK. Chipps et al[42] measured the $^{17}\text{F}(p,\gamma)^{18}\text{Ne}$ cross section directly for the first time, improving on uncertainties in the calculated reaction rate.

These huge variations in reaction rate calculations from comparatively small shifts in level energies make a strong argument that a clear experimental understanding of the level structure in ^{18}Ne is required in order to reduce uncertainty in the reaction rates involved in breakout of the hot-CNO cycle.

1.4 Motivation

There are two motivations for this work, as this project includes an instrumentation part and an astrophysical part. The first part involved the commissioning of the Jet Experiments in Nuclear Structure and Astrophysics (JENSA) gas target. With the development of new beam facilities such as the Facility for Rare Isotope Beams (FRIB) comes the need to develop

more advanced target systems. There are many reactions of astrophysical interest involving a proton, or α -particle, and a radioactive isotope.

Targets of these materials are typically hard to manufacture and come with drawbacks, such as unwanted material composing part of the target, such as the carbon in a solid CH_2 target. Reactions on the unwanted components of a compound target can cause a significant background in a measurement, and make low background measurements difficult. Similarly, reactions for studying nuclear structure often require non-solid targets, such as gas cells with windows. This window material can introduce background in a measurement. The Jet Experiments in Nuclear Structure and Astrophysics (JENSA) gas target is a windowless gas jet target, designed for low background reaction measurements of radioactive nuclei on hydrogen and helium. More details on the JENSA system are given in Section [?]. Part of the motivation of this work is commissioning the JENSA system. The commissioning experiments also related to, in particular, the spin-parity assignments of states in ^{18}Ne . This study also intends to address the discrepancies with the spin-parity assignments of states in ^{18}Ne by utilizing the $^{20}\text{Ne}(p,t)^{18}\text{Ne}$ reaction. This work will attempt to assign J^π values to states in ^{18}Ne through measurement of the angular distributions of reaction tritons and comparison with distorted wave Born approximation calculations (DWBA).

Chapter 2

Basic Nuclear Structure and Reaction Theory

2.1 Nuclear structure

The present work utilizes transfer reactions, specifically $^{20}\text{Ne}(p,t)^{18}\text{Ne}$, to probe the nuclear structure of ^{18}Ne . Transfer reactions are a powerful tool for studying nuclear structure, and can be used to extract a number of properties of nuclei, such as the excitation energies of states in a nucleus. The understanding of properties that are not directly observable can also be informed via transfer reaction experiments. The shape and structure of measured particle angular distributions gives insight to the L-transfer of a reaction, which can be used to infer the spin-parity of particular states.

2.1.1 Transfer reactions

A nuclear reaction is the process of nuclei colliding to produce other nuclei through the transfer of one or more nucleons. Transfer reactions can be written as follows:

$$A + a \rightarrow B + b + Q \tag{2.1}$$

Where A and a refer to the target and projectile nuclei (the reactants), B and b refer to the residual and recoil nuclei (the products). Q represents the reaction Q-value which

is equal to the difference in rest mass energies between the reactants and the products. A reaction Q-value thus corresponds to the amount of energy that either needs to be added to the system for the reaction to occur, or the amount of energy released in the reaction. The difference in invariant masses gives the ground state Q-value. Each excited state in the residual nucleus has a Q-value, given by the following:

$$Q_{final} = Q - E_x \quad (2.2)$$

Where E_x corresponds to the excitation energy of the state in the residual nucleus. It is typical to write transfer reactions such as Equation 2.1 using the following shorthand notation:

$$A(a, b)B \quad (2.3)$$

The nuclear binding energy is the mass defect between the sum of the constituent parts of the nucleus and the actual mass of the nucleus, and is given by:

$$E_B({}_Z^A X_N) = ZM_p c^2 + NM_n c^2 - M({}_Z^A X_N) c^2 \quad (2.4)$$

Where M_p and M_n denotes the proton mass and neutron mass, and $M({}_Z^A X_N)$ denotes the actual mass of the nucleus.

2.1.2 Reactions in normal kinematics

This section follows from Nuclear Reaction Analysis Graphs and Tables by J.B. Marion & F.C. Young[22].

$E_{1...4}$ and $M_{1...4}$ are defined as in Figure 2.1. Let us also define:

M = rest mass in MeV ($c = 1$)

T = kinetic energy

E = total energy = $T + M$

P = relativistic momentum = $\sqrt{E^2 - M^2} = \sqrt{T^2 + 2MT}$

E_T = total energy of the reactants = $T_1 + M_1 + M_2$

$Q = M_1 + M_2 - M_3 - [M_1^2 + M_2^2 + M_3^2 + 2M_2 E_1 - 2E_3(E_1 + M_2) + P_1 P_3 \cos \psi]^{\frac{1}{2}}$

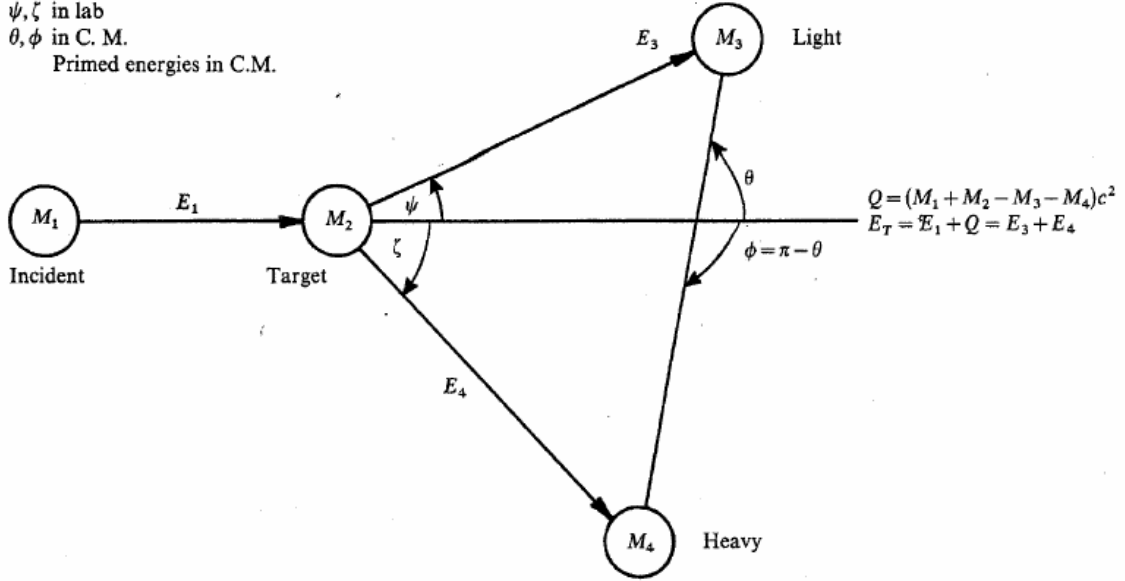


Figure 2.1: Diagrammatic representation of a generalized reaction between two nuclei. Let us define the following: M_1 is the incident particle, M_2 is the target particle, M_3 is the light recoil particle and M_4 is the heavy recoil particle, E_1 is the beam energy, E_3 is the light recoil particle energy and E_4 is the heavy recoil particle energy. The lab angles ψ and ζ may be greater than 90° , which is the case for inverse kinematics. Diagram from Nuclear Reaction Analysis Graphs and Tables by J.B. Marion & F.C. Young[22]

$$A = 2M_2T_1 + 2M_1M_3 + 2M_2M_3 + 2Q(M_1 + M_2 - M_3) - Q^2 \quad (2.5)$$

$$B = E_T^2 - P_1^2 \cos^2 \psi \quad (2.6)$$

$$C = \frac{M_2M_3}{(M_1 + M_2)(M_3 + M_4)} \left(1 + \frac{M_1Q}{M_2E_T}\right) \quad (2.7)$$

$$D = \frac{M_2M_4}{(M_1 + M_2)(M_3 + M_4)} \left(1 + \frac{M_1Q}{M_2E_T}\right) \quad (2.8)$$

$$\text{Where } A + B + C + D = 1 \quad \text{and} \quad AC = BD$$

The laboratory energy of the light product can be calculated using equations 2.5 through 2.8 and the laws of conservation of energy and momentum:

$$\frac{E_3}{E_T} = B + D + 2(AC)^{\frac{1}{2}} \cos \theta = \begin{cases} B[\cos(\psi) + (D/B - \sin^2 \psi)^{\frac{1}{2}}]^2 & \text{if } B < D \\ B[\cos(\psi) - (D/B - \sin^2 \psi)^{\frac{1}{2}}]^2 & \text{if } B > D \end{cases} \quad (2.9)$$

$$\text{Additionally, if } B > D \text{ then } \psi_{max} = \sqrt{\sin^{-1}(D/B)} \quad (2.10)$$

For the light product, the relation between the center of mass frame angle θ and laboratory frame angle ψ for the light product M_3 is as follows:

$$\sin \theta = \frac{E_3}{E_t} \sin \psi \quad (2.11)$$

The center of mass angle of the light product θ is dependent on D , which depends on the Q-value of the reaction. We measure the energy of the light product for different Q-values of the same reaction.

The solid-angle ratio for the light product is as follows:

$$\frac{\sigma(\theta)}{\sigma(\psi)} = \frac{(AC)^{\frac{1}{2}} \left(\frac{D}{B} - \sin^2 \psi\right)^{\frac{1}{2}}}{\frac{E_3}{E_T}} \quad (2.12)$$

E_3/E_t is dependent on ψ , and therefore the ratio between the solid-angle coverage in the laboratory frame to the center of mass frame is dependent on Q-value and angle.

2.1.3 Basic nuclear structure

Nucleons in the nucleus are ordered into orbitals, which relate to energy states that nuclei may occupy. These energy states can be determined by solving the Schrödinger equation for a potential $V(r)$ which describes the nucleus. For the nuclear shell model, the potential used is the Woods-Saxon potential (Equation 2.13):

$$V(r) = -\frac{V_0}{1 + \exp\left(\frac{r-R}{a}\right)} \quad (2.13)$$

Where V_0 is the potential well depth, typically ≈ 50 MeV, R describes the nuclear radius and is given by $R = 1.25A^{\frac{1}{3}}$ fm for stable nuclei, and a represents the diffuseness of the potential, and is typically taken to be 0.65 fm. When using a Woods-Saxon potential, the resulting energy levels can be seen on the left of Figure 2.2. The level structure on the right includes an additional level splitting term. Because of the Pauli exclusion principle, orbitals may have a certain number of quantum states, each of which can only contain a

studied via the transfer reactions such as $^{16}\text{O}(\text{d,p})^{17}\text{O}$. The 8 neutrons in ^{16}O fill the 1s and 1p orbitals, so the neutron supplied by the (d,p) reaction is expected to strongly populate states where the last neutron is in the 2s orbital or one of the 1d orbitals, and therefore the expected angular momentum transfer of $\Delta L = 0$ or 2 respectively. As the ground state of ^{16}O has a spin-parity of $J^\pi = 0^+$ and the spin of the transferred neutron $S = \frac{1}{2}$, one would populate states where $J^\pi = \frac{5}{2}^+$ or $\frac{1}{2}^+$ in ^{17}O via $^{16}\text{O}(\text{d,p})^{17}\text{O}$. The shape of the angular distribution of recoil particles from a reaction, in the case of the $^{16}\text{O}(\text{d,p})^{17}\text{O}$ example, the protons, gives us information on the spin-parity of the residual nucleus.

2.1.4 Thomas-Erhman shifts

The neutron and proton have similar properties, although a proton has positive charge and has a slightly lower mass than the neutron. They can be viewed as two states of the nucleus that are acted on equally by the strong force. Mirror nuclei are pairs of nuclei that have their proton and neutron numbers reversed with respect to the other member of the pair, for the case of ^{18}Ne with 8 neutrons and 10 protons, the mirror nucleus has 10 neutrons and 8 protons, so ^{18}O . Energy levels in the mirror nucleus can tell us the expected spin-parities and level structure in the nucleus of interest. Though the spin-parities of the states match up between the proton-rich and neutron-rich mirror nuclei, there are differences in the excitation energies in these states, known as Thomas-Erhman (T-E) shifts. This is due to the Coulomb shift between protons and neutrons. Wiescher et al[6] calculated these shifts for most of the known states in ^{18}Ne between $5000 \text{ keV} < E_x < 8500 \text{ keV}$. The average T-E shift for most states in ^{18}Ne , as calculated by Wiescher et al[6], is approximately 110 keV from states in ^{18}O . There is a rather large shift of approximately 800 keV between two known states in ^{18}O and ^{18}Ne , a $J^\pi = 0^+$ state at $E_{x(^{18}\text{O})} = 5336 \text{ keV}$ and $E_{x(^{18}\text{Ne})} = 4590 \text{ keV}$.

Known states in ^{18}O give us information about the expected level structure regarding any currently unobserved states in ^{18}Ne , and provide a good reference point for the expected spin-parity of those states.

2.2 Distorted wave Born approximation

2.2.1 DWBA

The Distorted Wave Born Approximation (DWBA) is a theoretical approach to nuclear scattering by a potential. The scattering amplitude is given by the following equation[43]:

$$f_{DWBA}(\theta, \phi) = f_1(\theta, \phi) - \frac{1}{4\pi r} \int \chi_1^{(-)}(\mathbf{k}', \mathbf{r}') * U_2(\mathbf{r}') \chi_1^{(+)}(\mathbf{k}, \mathbf{r}') d\mathbf{r}'. \quad (2.14)$$

DWBA is named as such because the first order term $f_1(\theta, \phi)$ from the potential is from the Born approximation, but that we also utilize distorted waves $\chi_1^{(\pm)}$.

The optical model potentials U often take the form:

$$U(R) = -V_0 f(R, r_0, a_0) - iW_v f(R, r_v, a_v) - iW_D g(R, r_D, a_D) \quad (2.15)$$

Where:

- V_0 = real potential well depth
- r_0 = real mean radius
- a_0 = real well diffuseness
- W_v = imaginary well depth
- r_v = imaginary radius
- a_v = imaginary well diffuseness
- W_D = surface imaginary well depth
- r_D = surface imaginary radius
- a_D = surface imaginary diffuseness

g is the nuclear surface form factor:

$$g(R, r, a) = 4a \left(\frac{d}{dr} \right) f(R, r, a) \quad (2.16)$$

and f is the Woods-Saxon form factor:

$$f(R, r, a) = \frac{1}{(1 + e^{\frac{(R-r)}{a}})} \quad (2.17)$$

The scattering potential (2.15) is complex. The real part of the potential (Equation 2.15) represents elastic scattering, and the imaginary part represent all other non-elastic processes. The imaginary term in Equation 2.15 can include the volume term ($-iW_v f(R, r_v, a_v)$), responsible for non-elastic processes somewhere in the volume of the nucleus, the surface term ($iW_D g(R, r_D, a_D)$), responsible for non-elastic processes at the surface or both. Optical model parameters describe the potential and can be obtained experimentally via elastic scattering experiments. While data exists for many stable species, not as much data exists for species far from stability. To address this, global optical model parameters can be used. Global optical models average and parameterize empirical data from across the nuclear chart, based on A , Z , and bombarding energy E . In general, these optical model parameters are different for the incoming and outgoing channels, so in the case of $A(a,b)B$, two different sets of parameters would be used; $A + a$ and $B + b$.

The result of these calculations is a differential cross section, the shape of which is often referred to as an angular distribution. These cross sections can be measured experimentally and compared to calculations. The angular distributions can be thought of as a diffraction pattern of the reaction; the cross section changes with angle due to the differing interactions of the wave-functions of the nuclei. Though DWBA calculated cross sections are typically sensitive to optical model parameters, the overall shape of the angular distribution is characterized by the L-transfer[44]. Lower angles in the center of mass system correspond to more peripheral interactions, and therefore variations in the optical model parameters generally have less of an effect at lower angles. The DWBA code utilized in this analysis is TWOFNR[45]. TWOFNR is a one-step DWBA code and treats reactions such as (p,t) as the transfer of a single 2n particle with $S=0$. As $J = L + S$, with $S=0$, J reduces to $J = L$. Equation 2.18 gives the definition of parity:

$$\pi = (-1)^L \tag{2.18}$$

Utilizing a one-step code, we can only account for natural parity states, those which follow from the definition of parity. Unnatural parity states, such as a $J^\pi = 3^+$ (As, if

$S=0$ and $J=3$, then $L=3$, and following from (2.18) only 3^- should be possible), can only be populated by two-step processes, where $S \neq 0$.

DWBA is useful for analyzing data from single nucleon transfer reactions such as (d,n), and reactions which can be approximated to single nucleon transfer, like (p,t). When other processes, such as two step transfers begin to contribute strongly, more representative results can be obtained via other methods, such as using a coupled channel Born approximation (CCBA) formalism[44].

For the case of $^{20}\text{Ne}(p,t)^{18}\text{Ne}$, the incoming channel ($^{20}\text{Ne} + p$) has been measured experimentally via proton scattering on ^{20}Ne and is well understood. There is no similar scattering data for the outgoing channel, however. DWBA parameters used in previous studies on $^{18}\text{Ne} + t$ have tailored the optical model parameters used to the particular state of interest to the study. The parameters used in the present work are listed in Table 2.1.

Table 2.1: These parameters were used for all DWBA calculations shown in Chapter 5. These are as listed in Park et al[10].

	V_0 (MeV)	r_0 (fm)	a_0 (fm)	W_v (MeV)	r_v (fm)	a_v (fm)	W_D (MeV)	r_D (fm)	a_D (fm)
$p+^{20}\text{Ne}$	-42.33	1.197	0.746	-11.31	1.196	0.786	00.72	1.196	0.786
$t+^{18}\text{Ne}$	-100	1.38	0.75	-85.00	1.55	0.85	45.00	1.55	0.85

2.2.2 DWBA parameter variations

The parameters used in the current work, listed in Table 2.1 for the incoming ($^{20}\text{Ne} + p$) channel came from a scattering measurement[9], while for the outgoing channel ($^{18}\text{Ne} + t$) there is no scattering data. For this reason, the parameters in the outgoing channel were varied individually over a range of values to see what effect they had on the shape of the angular distribution, starting from the baseline parameters listed in Table 2.2. For the present work, the absolute cross section is not important, only the overall shape of the angular distribution. These calculations were performed for the ground state to ground state $L=0$ transfer. All figures in this section have been restricted to an angular range relevant to the present work, between 10° and 70° in the center of mass frame.

Figures 2.3, 2.4 and 2.5 show the effect of varying the real potential well depth, the real radius and the real well diffuseness parameters in the outgoing channel respectively. There is very little change in both the shape of the angular distribution and the absolute cross section over the range parameters. This is because the real parameters represent the elastic scattering part of the interaction, and the calculation represents an inelastic process.

Figures 2.6, 2.7 and 2.8 show the effect of varying the imaginary potential well depth, the imaginary radius and the imaginary well diffuseness parameters in the outgoing channel respectively. Unlike the variations in the real parameters, varying the imaginary parameters has a more significant effect on the absolute cross section, though not much of an effect on the overall shape of the angular distributions. This larger change in the cross section is expected, as the imaginary input parameters represent non-elastic processes, and this is an inelastic reaction.

Figure 2.9 shows the effect of varying the imaginary surface potential parameter. The general shape of the angular distribution stays the same over the range of parameters used, though there are differences between the feature heights of the first and second minimum.

In all calculations, the shape remains approximately the same for an L=0 transfer. While small variations in the specific parameters may produce a better fit for certain states, the shape of the angular distribution is mostly dependent on the specific L-transfer. A comparison of the base set (Falk et al set 4 [9]) used in these parameter variations and the set chosen for this analysis (Park et al [10]) can be seen in Figure 2.10.

Table 2.2: The baseline parameters listed below were used for the sensitivity search in this section, and correspond to parameter set 4 from Falk et al[9]. TWOFNr uses $r_v = r_D$ and $a_v = a_D$ and therefore the value listed for a_V was used for a_D , not $a_D = 0.54$ fm.

	V_0 (MeV)	r_0 (fm)	a_0 (fm)	W_v (MeV)	r_v (fm)	a_v (fm)	W_D (MeV)	r_D (fm)	a_D (fm)
Falk Set 4	120.0	1.25	0.65	50.0	1.90	0.65	40.0	1.90	0.65

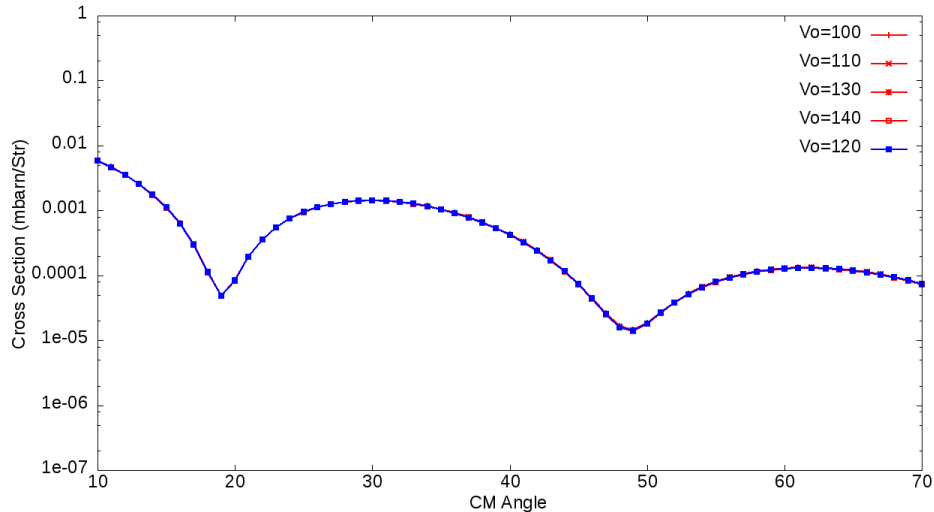


Figure 2.3: The parameter V_0 , the real well depth of the outgoing ($t+^{18}\text{Ne}$) optical potential was varied over a range of 100 - 140 MeV (Red) to study the effect on the shape of the angular distribution. Varying this parameter had very little effect on the cross section and no effect on the shape of the distribution. A calculation using the original value listed in Falk et al set 4[9] is also shown (Blue).

2.2.3 Finite range, zero range and LEA

In DWBA, there are three ways of treating the potentials in transfer reactions: finite range, zero-range, and Local Energy Approximation (LEA). Finite range is the full exact treatment of the finite range of the potentials[44]. The zero-range approximation greatly simplifies the calculation by approximating the interaction radii of the incoming and outgoing channels to a single parameter[46]. The LEA is the application of a first-order correction to the zero range approximation[44]. The zero-range approximation is valid for light s-wave nuclei, such as α -particles or tritons[47, 46, 44], and for this reason the zero-range approximation will be utilized for the present work.

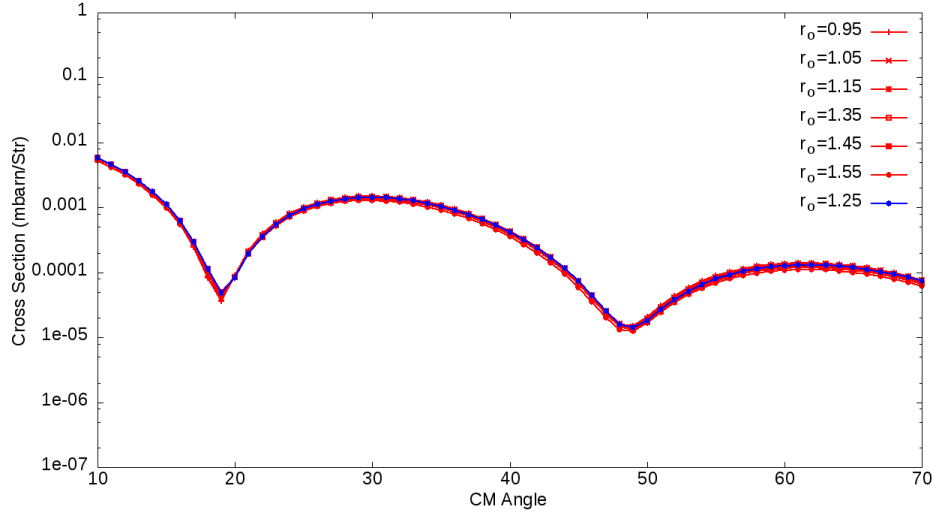


Figure 2.4: The parameter r_0 , the real radius of the outgoing ($t+^{18}\text{Ne}$) optical potential was varied over a range of 0.95 - 1.55 fm to study the effect on the shape of the angular distribution. Varying this parameter had very little effect on the cross section and no effect on the shape of the distribution. A calculation using the original value listed in Falk et al set 4[9] is also shown (Blue).

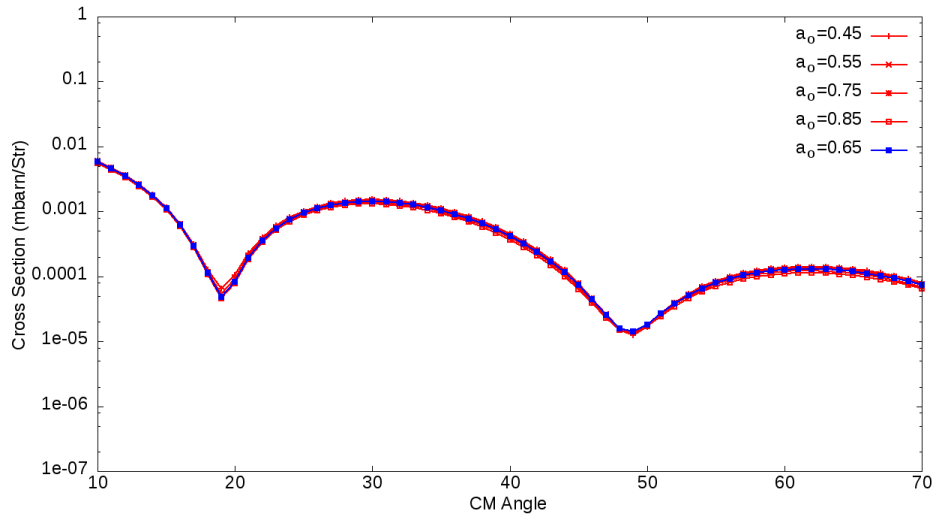


Figure 2.5: The parameter a_0 , the real well diffuseness of the outgoing ($t+^{18}\text{Ne}$) optical potential was varied over a range of 0.45 - 0.85 fm to study the effect on the shape of the angular distribution. Varying this parameter had very little effect on the cross section and no effect on the shape of the distribution. A calculation using the original value listed in Falk et al set 4[9] is also shown (Blue).

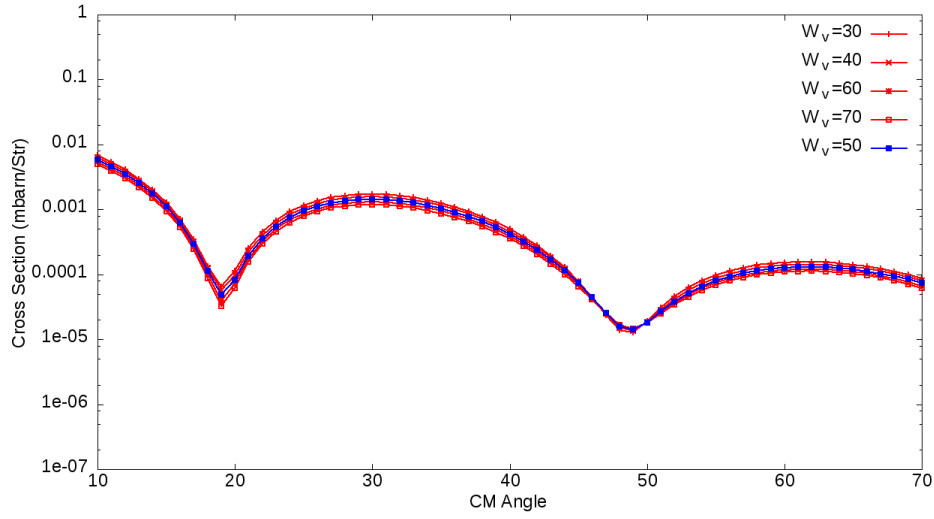


Figure 2.6: The parameter W_v , the imaginary well depth of the outgoing ($t+^{18}\text{Ne}$) optical potential was varied over a range of 30 - 70 MeV to study the effect on the shape of the angular distribution. Varying this parameter had very little effect on the cross section and no effect on the shape of the distribution. A calculation using the original value listed in Falk et al set 4[9] is also shown (Blue).

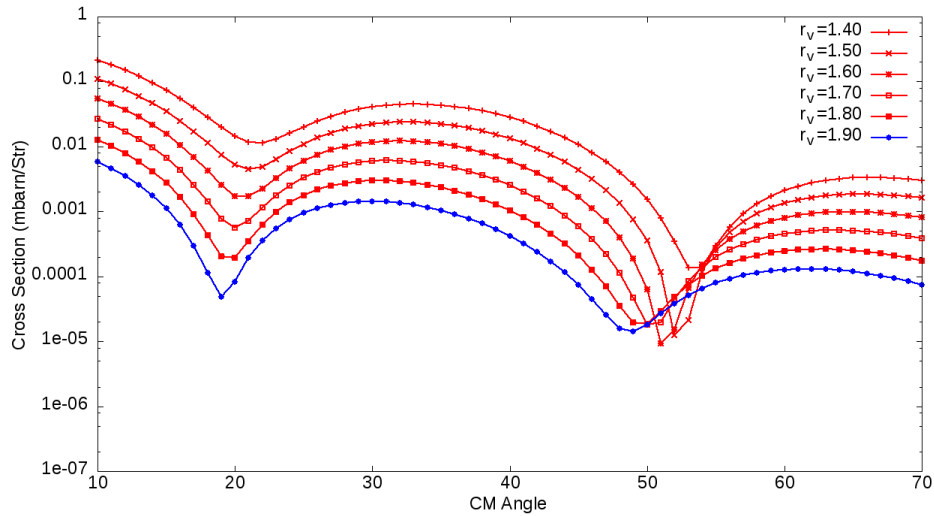


Figure 2.7: The parameter r_v , the imaginary radius of the outgoing ($t+^{18}\text{Ne}$) optical potential was varied over a range of 1.40 - 1.90 fm to study the effect on the shape of the angular distribution. This parameter was only lowered, as a value of $r_v = 1.90$ fm is already large. Though the shape is still identifiable as an $L=0$ transfer, varying this parameter had a significant effect on the cross section. A calculation using the original value listed in Falk et al set 4[9] is also shown (Blue).

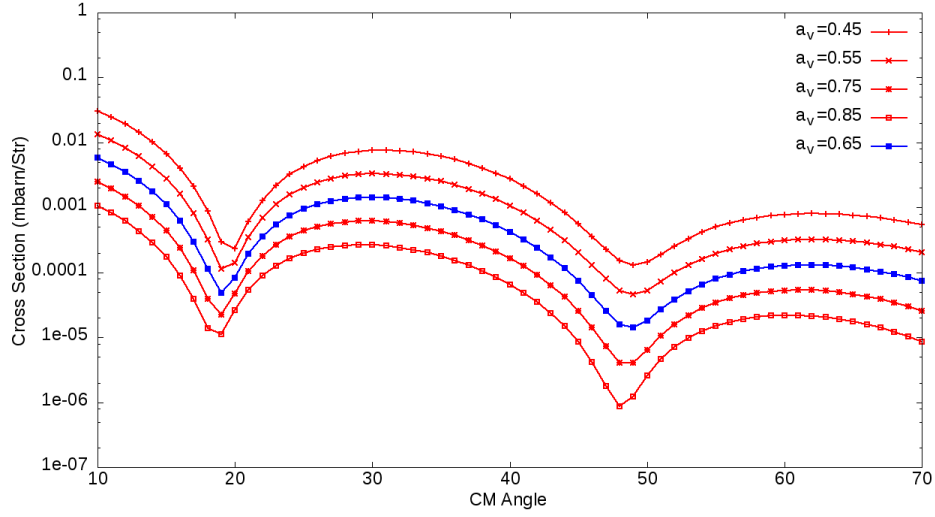


Figure 2.8: The parameter a_v , the imaginary well diffuseness of the outgoing ($t+^{18}\text{Ne}$) optical potential was varied over a range of 0.45 - 0.85 fm to study the effect on the shape of the angular distribution. Varying this parameter had a significant effect on the cross section, but little effect on the overall shape of the angular distribution. A calculation using the original value listed in Falk et al set 4[9] is also shown (Blue).

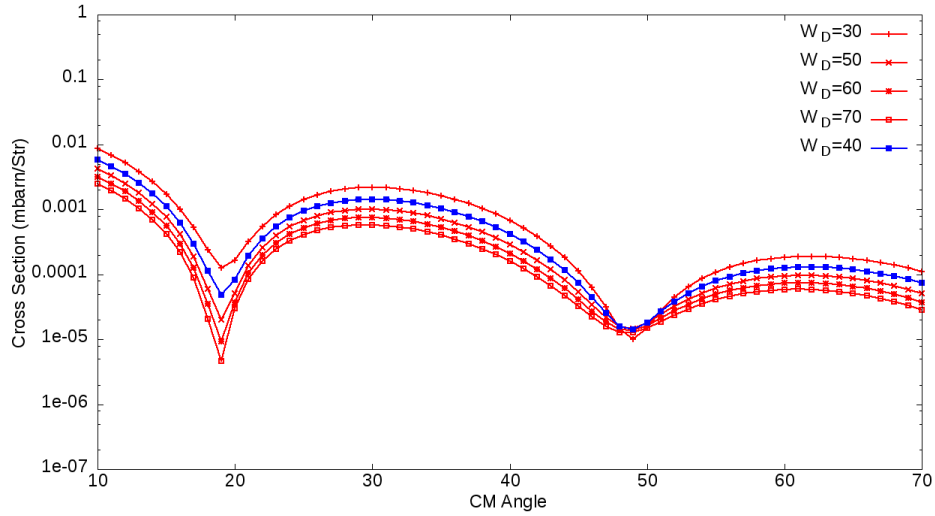


Figure 2.9: The parameter W_D , the surface imaginary well depth of the outgoing ($t+^{18}\text{Ne}$) optical potential was varied over a range of 30 - 70 MeV to study the effect on the shape of the angular distribution. The general shape of the angular distribution stays the same over the range of parameters used, though there are differences between the feature heights of the first and second minimum. A calculation using the original value listed in Falk et al set 4[9] is also shown (Blue).

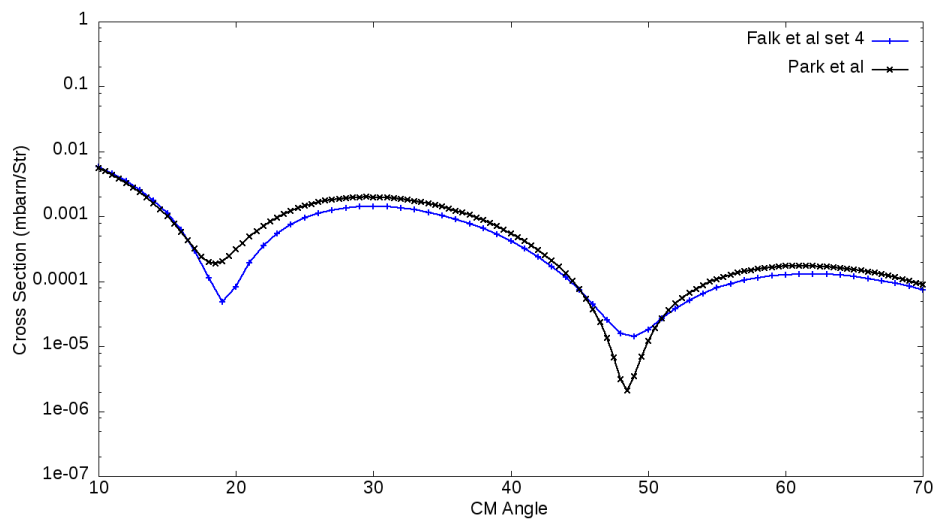


Figure 2.10: Comparison of Falk set 4[9] which are the base parameters used in Figures 2.3 - 2.9 and Park et al[10], the parameters used for the DWBA calculations shown in Chapter 5. Though there are differences in relative feature height, both calculations exhibit the same features: a first minimum at around 20° and a second minimum at around 50° .

Chapter 3

Instrumentation

There are three vital components to any transfer reaction measurement: the target, the beam, and the detectors. In this chapter, the instruments used to perform the experiment will be presented, why they were used and the job they perform will be discussed.

3.1 Target

Reactions of astrophysical interest are typically radioactive nuclei reacting with hydrogen or helium. This presents a difficulty when studying these reactions, as hydrogen, helium and radioactive nuclei are difficult to use as target material. Solid targets, such as CH_2 , can be used with radioactive beams but reactions on the carbon in the target material can present a significant background, making low statistics measurements difficult. The Jet Experiments in Nuclear Structure and Astrophysics (JENSA) gas jet target is designed to be a highly localized, dense and pure gas jet target for use in astrophysically important reaction studies.

3.1.1 Overview

JENSA was designed for use as a highly localized hydrogen or helium gas-jet target for reactions of astrophysical interest. JENSA is a recirculating system. The gas is collected from the target by two concentric receivers, and then pumped back into the system through

a closed loop of oil-free pumps and a custom industrial compressor[11]. At the time these data were recorded, the JENSA system comprised of:

Target chamber with nozzle, two concentric gas receivers and room for various detectors around the target location (Figure 3.2a),

A two-stage oil-free diaphragm compressor, rated to 80 Nm³/hr, with atmospheric pressure at the inlet and over 400psi at the outlet[11],

8 gas-flow limiting apertures along the beamline, 4 upstream and 4 downstream (3.2)

9 water cooled turbomolecular pumps, each individually controlled (Listed in Table 3.1),

7 single-stage roots blowers (Listed in Table 3.1),

4 multi-stage water-cooled roots blowers (Listed in Table 3.1).

Table 3.1: Vacuum pump specifications as listed on the manufactures specification sheets for the JENSA system as shown in the pumping schematic (Figure 3.1).

Manufacturer/Model	Type	Nominal pumping speed (m^3h^{-1})
Leybold WSU501	Air-cooled Roots blower	505
Leybold WSU1001	Air-cooled Roots blower	1000
Leybold WSU2001	Air-cooled Roots blower	2050
Ebara A10S	Water-cooled Multistage Roots blower	72
Shimadzu 3203	Water-cooled Turbomolecular pump	3300
Leybold 361C	Water-cooled Turbomolecular pump	1440
Leybold 600C	Water-cooled Turbomolecular pump	2016
Leybold 1000C	Water-cooled Turbomolecular pump	3060

Table 3.2: Aperture dimensions (Parameters from Chipps et al[11]) for the JENSA system as shown in the pumping schematic (Figure 3.1). The restrictive apertures upstream limit allow a high pressure jet in the target chamber and limit gas flow up the beam line.

Aperture	U4	U3	U2	U1	D1	D2	D3	D4
Diameter (mm)	5	5	4	3	15	19	24	28
Length (mm)	40	40	60	50	60	60	60	60

A list of collaborators for the JENSA project can be found in Appendix C

3.1.2 Commissioning of JENSA

This measurement was part of the commissioning campaign of the JENSA system. JENSA was commissioned and built at Oak Ridge National Laboratory (ORNL), at the Holifield

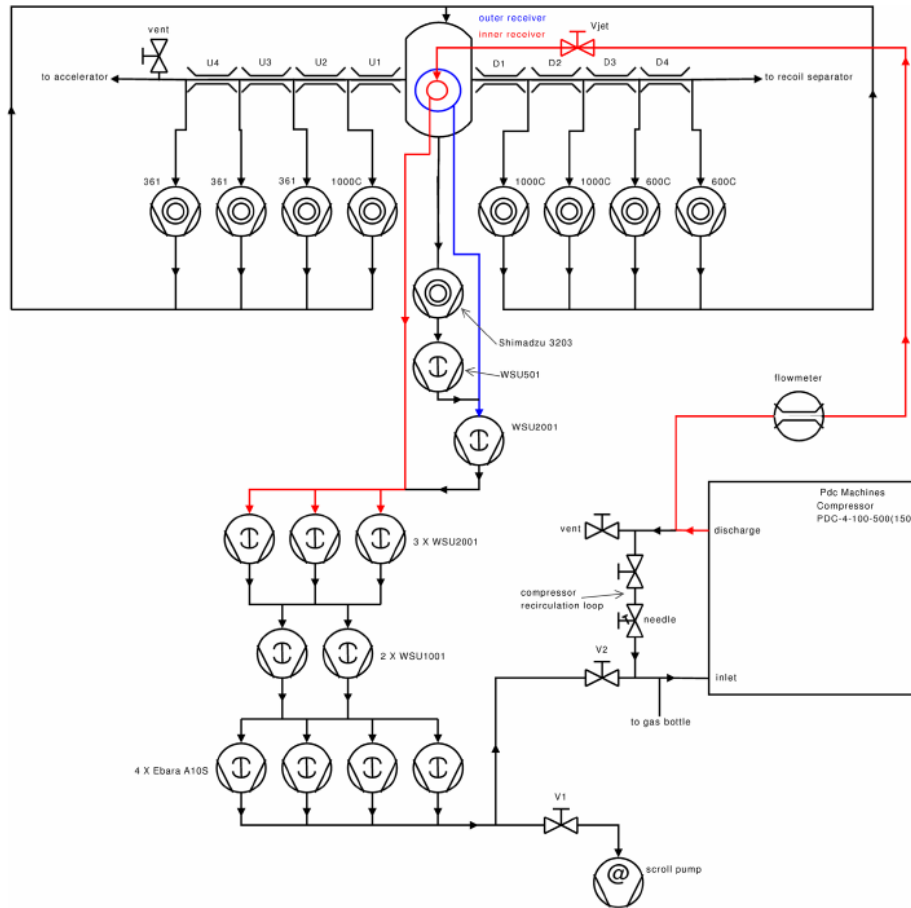


Figure 3.1: Pumping schematic for the JENSA system as configured at Oak Ridge National Laboratory and the present work. Vacuum pump specifications are listed in Table 3.1, and aperture specifications for U4 through D4 are listed in Table 3.2. Figure from Chipps et al[11]

Radioactive Ion Beam Facility (HRIBF), where the system was characterized and a number commissioning experiments were performed with the system. The commissioning experiments were: $^{14}\text{N}(p,t)^{12}\text{N}$ [48], $^{20}\text{Ne}(p,d)^{19}\text{Ne}$ [49], $^{20}\text{Ne}(p,t)^{18}\text{Ne}$ (Present work), $^{15}\text{N}(\alpha,\alpha)^{15}\text{N}$ [11] and $^{120}\text{Sn}(^{14}\text{N},^{14}\text{N})^{120}\text{Sn}$ [50]. Multiple facets of the JENSA system were characterized as part of the commissioning at ORNL. This included, among other parameters, the pressure inside the chamber, the pressure along each stage U4 through D4 as labeled on Figure 3.1, and the pressure profile across the jet. The restrictive apertures U4 through U1 additionally collimate any beam halo. A full discussion of the characterization of the JENSA system is given in Chipps et al[11].

3.1.3 Nozzles

JENSA utilizes Laval nozzles to create the jet. Laval nozzles are shaped like a stretched hourglass (See Figure 3.2b), and the narrow section (the throat) causes the gas to become supersonic. The mass flow rate is given by the following equation:

$$\dot{m} = \rho v A \quad (3.1)$$

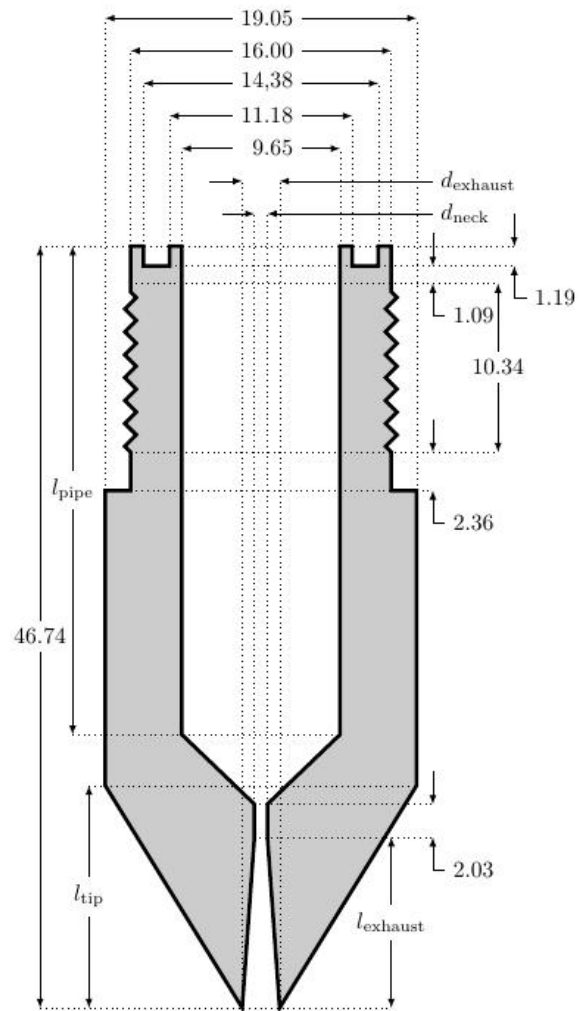
Where ρ is the gas density, v is the gas velocity and A is the area of the tube. Mass flow rate is conserved, so as the area of the tube decreases, the velocity increases. The supersonic gas then expands into the wider area after the throat and maintains the supersonic flow rate[51, 52]. A cross section of the Laval nozzles used with JENSA can be seen in Figure 3.2b. Multiple Laval nozzles have been manufactured and tested with JENSA, with nozzle neck widths (d_{neck} in Figure 3.2b) varying from 0.8 mm to 1.1 mm, and the specifications of each nozzle are listed in Table 3.3.

3.1.4 Measurement of jet density

In order to characterize the jet formed by the different nozzles, tests were performed both during the commissioning of JENSA at ORNL, and replicated at the NSCL after the JENSA system was moved. Through this section, psi will be used in reference to gauge pressure reading (psig), not absolute pressure readings. All actual analysis of the gas jet target by



(a) Photograph of inside the JENSA chamber showing a nozzle and two concentric receivers. When the system is operational, gas leaves the nozzle through the gap and is collected in the concentric receivers. The collected gas is then recirculated back into the compressor is reused as target gas. Photograph courtesy of Kelly Chipps.



(b) Cross section of the JENSA Laval nozzles. Dimensions are in mm, and the variable parameters shown are in Table 3.3. Figure from Schmidt et al[12].

Figure 3.2: Image of the central JENSA chamber, and cross section of the JENSA Laval nozzles.

Table 3.3: JENSA nozzle specifications. These parameters correspond to the lengths as labeled on Figure 3.2b and are given in mm. Tolerances for the individual lengths are listed in the last row. Specifications are from Schmidt et al[12].

Nozzle	d_{neck}	$d_{exhaust}$	$l_{exhaust}$	l_{pipe}	l_{tip}
A	0.80	2.39	7.62	32.64	14.43
B	0.80	3.20	11.40	31.39	13.72
C	0.90	2.69	8.61	31.65	14.17
D	1.00	3.00	9.50	30.76	13.89
E	1.10	3.30	10.49	29.77	13.64
F	1.10	3.30	10.49	29.77	13.64
Tol.	0.08	0.08	0.25	0.25	0.25

Chipps et al[11] and Schmidt et al[12] were performed using absolute readings taken at the inlet of the jet nozzle. I was involved in the data collection process for both sets of tests, but in both cases the analysis was performed by another party.

Stopping power

Both sets of measurements of the JENSA jet density consisted of measuring the energy loss of α -particles as they travel through the jet.

For charged particles, the linear stopping power, S , in a given material is as follows[53]:

$$S = -\frac{dE}{dx} \quad (3.2)$$

This represents the differential energy loss of the particle (dE) over the differential path length (dx). The expression which describes this is known as the Bethe formula and is as follows:

$$S = \frac{4\pi e^4 z^2}{m_0 v^2} N B_B \quad (3.3)$$

Where:

$$B_B \equiv Z \left[\ln \frac{2m_0 v^2}{I} - \ln \left(1 - \frac{v^2}{c^2} \right) - \frac{v^2}{c^2} \right] \quad (3.4)$$

Where v is the incoming particle velocity, ze is the electron charge, N is the number density of material atoms, Z is the atomic number of material (and combining the two, NZ is the electron density), m_0 is the electron rest mass and I is known as the average excitation and ionization potential for material, and is determined experimentally.

From the Bethe formula (Equation 3.3), we can see that when $v \ll c$, only the term involving I is significant in B_B . B_B varies slowly with particle energy, therefore the first factor in S , $\frac{4\pi e^4 z^2}{m_0 v^2}$, is the most important in this case. This factor varies with $\frac{1}{v^2}$, so the lower the kinetic energy of the particle, the slower it moves and the longer the particle is in the medium, the more energy it will deposit in the medium.

The Bethe formula describes the energy loss of a charged particle in a medium and relates to this work in two ways, the tritons measured lose energy in the thin dE detectors and thicker E detectors, and the calibration of the jet at both the NSCL and ORNL both involve the energy loss of alpha particles traveling through the jet.

ORNL density tests

The density profile tests at ORNL were performed using a superORRUBA (Oak Ridge Rutgers University Barrel Array) segmented silicon strip detector, with 64 front side strips (1.2 mm width) and 4 back side strips (1 cm width), and a ^{244}Cm source. ^{244}Cm is an α emitter with two main α energies, $E_{\alpha 0} = 5804.77$ keV (76.90%) and $E_{\alpha 1} = 5762.64$ keV (23.10%)[54]. The energy loss of the $E_{\alpha 0}$ particles through 3 different jet gases, helium, nitrogen, and neon, was measured at nominal jet outlet pressures of 200, 300 and 400 psi. As the jet density increases, the energy loss of the α -particles that travel through the jet increases (Refer to Section 3.1.4). These energy losses can be converted to areal jet densities using measured stopping powers of α -particles in the aforementioned gases[55] via the following formula:

$$\epsilon = \frac{E_l}{N} \quad (3.5)$$

Where ϵ is the α -particle stopping cross section in units of eV/10¹⁵ atoms cm⁻², E_l is the measured energy loss in eV, and N is the molecular density of the jet in 10¹⁵ atoms cm⁻².

The use of a highly segmented silicon strip detector allows for mapping of the energy loss as a function across the jet. An example from tests performed at the NSCL is shown in Figure 3.5. For the ORNL jet density tests, the width of the jet was measured using aluminum strips of known width at the jet location, comparing the energy loss profile observed when the jet was active to the number of strips shadowed from the α -source with a small aluminum strip in the target location. The results from these tests are discussed in greater detail in Chipps et al[11] and the results from one particular case (Top 4 mm, central 4 mm of jet, ^{Nat}He Areal jet density at 200, 300, and 400 psi for nozzle A) is shown in Figure 3.6.

NSCL density tests

After the commissioning run at ORNL, JENSA was deconstructed, the entire system moved to the National Superconducting Cyclotron Laboratory (NSCL) at Michigan State University (MSU) and reconstructed in the ReAccelerator for 3 MeV/u beams (ReA3) hall. After the move, similar density profile measurements were performed. Like the ORNL measurements, these measured the energy loss of α -particles through the jet at different jet pressures. These measurements also utilized a superORRUBA segmented silicon strip detector, but in this case a ^{241}Am source was used ($E_{\alpha 0} = 5485.56 \text{ keV}$ (84.8%) and $E_{\alpha 1} = 5442.80 \text{ keV}$ (13.1%))[56]), and measurements were performed at nominal jet pressures of 150, 250, and 350 psi. Figure 3.3 shows a photograph of the testing procedure at the NSCL, and Figure 3.4 shows a side-on representation of the setup for the NSCL jet density tests, with distances. The results from these tests are discussed in greater detail in Schmidt et al[12] and the results from one particular case (Top 4 mm, ^{Nat}He Areal jet density at 150, 250, and 350 psi for nozzle A) is shown in Figure 3.6.

Density test results

Results from two similar cases are shown in Figure 3.6. Both the ORNL and NSCL jet density tests show the same result: α -particle energy loss increases linearly as a function of jet density. The slight difference in offset is due to differences in ambient pressure in the chamber. The behavior of the JENSA system as seen at ORNL during the commissioning period has been replicated at the NSCL after the system was rebuilt.

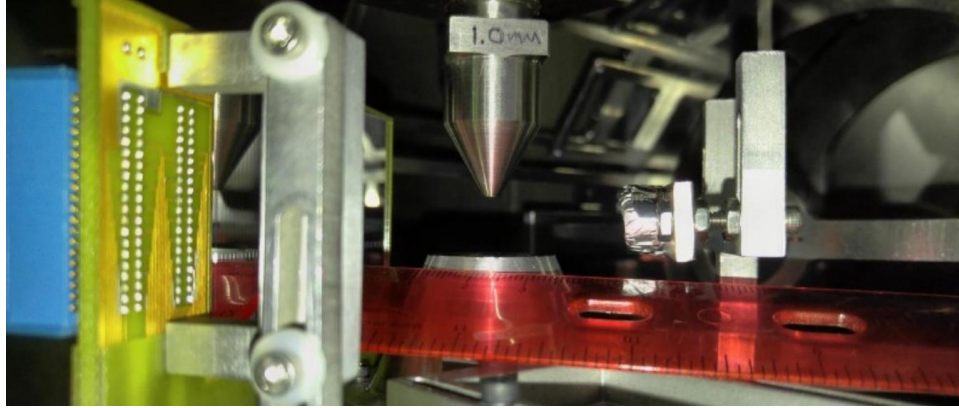


Figure 3.3: Photograph of the setup for the nozzle tests performed at the NSCL. The source, nozzle, receiver and detector are all pictured.

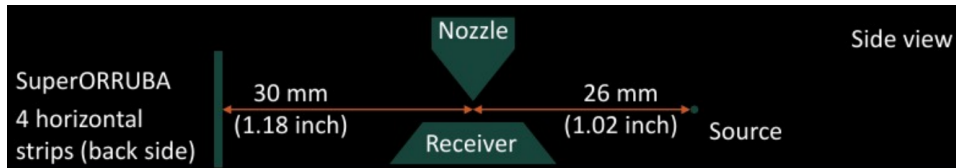


Figure 3.4: Diagrammatic representation of the setup for the NSCL jet density tests. Distances between the source, target and detector are all shown. The tests at ORNL used a similar setup, but relative distances were different. Figure courtesy of Konrad Schmidt.

3.1.5 JENSA for the $^{20}\text{Ne}(p,t)^{18}\text{Ne}$ study

The target for this experiment was the JENSA gas jet target as discussed earlier in this section. Natural neon gas was used as the target gas, the composition of which is listed in Table 3.4. The jet was maintained at 300 ± 15 psi for the length of the experiment.

Table 3.4: Natural abundances of neon isotopes[13].

Isotope of Neon	Natural Abundance
^{20}Ne	90.48%
^{21}Ne	0.27%
^{22}Ne	9.25%

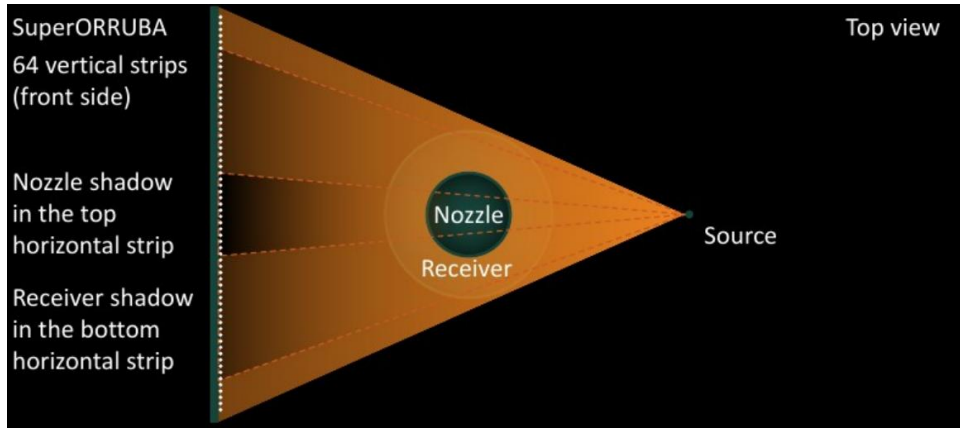


Figure 3.5: Cartoon showing the “projection” of the jet on the superORRUBA segmented silicon detector through the density tests. Figure courtesy of Konrad Schmidt.

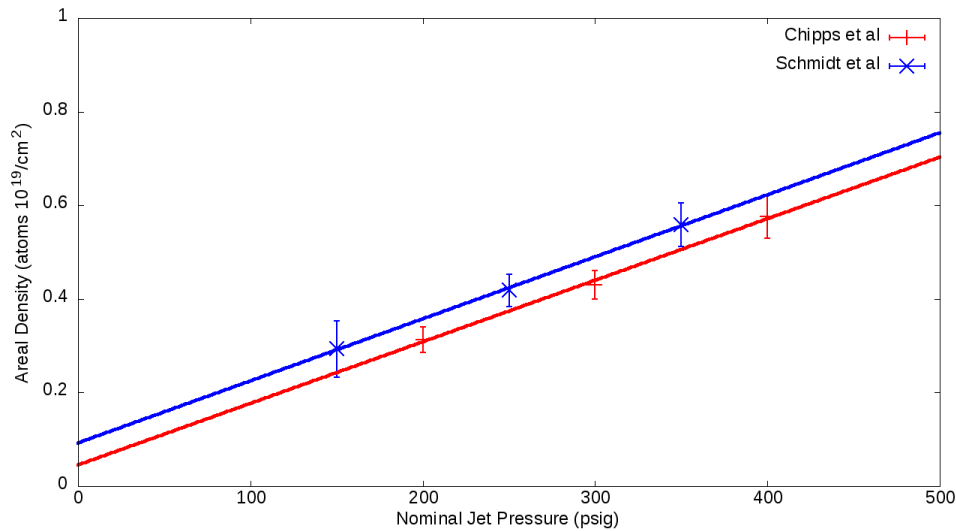


Figure 3.6: A typical result from both the ORNL and NSCL JENSA jet density tests. A linear increase in α -particle energy loss (and therefore jet density) can be seen for tests at both laboratories. The ORNL result shown is for the specific case for α -particle energy loss over the central 2 mm of jet through a ^{Nat}He target at 200, 300, and 400 psi with nozzle A. The NSCL result shown is for the specific case for α -particle energy loss in the central 2 mm of the jet through a ^{Nat}He target at 150, 250, and 350 psi with nozzle A.

3.2 Beam production

A proton beam was accelerated using the 25 MV tandem accelerator at Oak Ridge National Laboratory (ORNL), at the Holifield Radioactive Ion Beam Facility (HRIBF). Negative TiH ions were produced by a TiH cathode tip sputter source, then accelerated into the tandem terminal before being stripped to produce the proton beam[57]. For the present $^{20}\text{Ne}(p,t)^{18}\text{Ne}$ measurement, a beam energy of 37 MeV was chosen.

3.3 Detectors

3.3.1 Silicon detectors

Silicon detectors are part of a group of semiconductor detectors, which are commonly used for charged particle measurements[53]. Crystalline solids such as silicon have a band structure with a lower energy valence band and a higher energy conduction band. These two bands are separated by a gap in energy known as the band gap, E_g . The valence band contains the outer shell electrons that are bound to the crystal structure of the lattice, while the conduction band contains free moving electrons, which contribute to the conductivity of the material. Semiconductors have a much lower band gap than insulating materials, with $E_g \gtrsim 1$ eV in the case of semiconductors, and $E_g \gtrsim 9$ eV for insulators. For electrons to move from the valence band to the conduction band, they need enough energy to cross the band gap.

When a charged particle passes through the active area of a semiconductor, electrons are excited from the valence band and pushed into the conduction band. This leaves a hole in the valence band. These electron-hole pairs are created in equal parts. There is a layer on either side of the active area which is inactive, but particles still deposit some energy as they pass through this inactive area. This inactive region is referred to as the dead layer of the detector. If an electric field is applied to the material, the holes will move along the direction of the electric field in the valence band, as electrons move up in the opposite direction of the electric field and fill in the holes, leaving behind a hole where they moved from. Electrons will also move in the conduction band, and the movement of these electrons and holes creates

a current proportional to the energy deposited by the charged particle, and this current can be measured by contacts either side of the material.

3.3.2 Detector configuration

For this experiment, we used an array of single-sided annular segmented silicon strip detectors, the Silicon Detector ARray (SIDAR). A single detector can be seen in Figure 3.7, and the specifications of these detectors are listed in Table 3.5. SIDAR is an annular array of detectors, designed to be used as either a flat ring of eight detectors, or six detectors tilted by 43° towards the beam-line in a “lampshade” configuration. The active area of the individual areas of the detectors is separated into 16 strips of equal width, but varying length. For the present work, SIDAR was used in the “lampshade” configuration (Figure 3.8), with three pairs of detectors, referred to as telescopes, with each telescope comprising of one thick silicon detector ($\sim 1000 \mu\text{m}$ thick) with a thin detector ($\sim 65 \mu\text{m}$ thick) mounted directly in front of it. Small standoffs keep the two detectors separated by $\frac{5}{16}$ inches. Utilizing pairs of detectors in this configuration allows for ΔE -E particle identification, which is discussed in greater detail in Chapter 4. Using the detectors in this configuration allows us to have a large angular coverage (20° to 55° in the lab frame) while maintaining a large solid angle coverage.

Table 3.5: Pertinent specifications for a single Micron Semiconductors Ltd YY1 detector, used in SIDAR[14].

Design:	DC single-sided annular detector
Active inner dimensions:	55 mm
Outer inner dimensions:	130 mm
Number of sectors:	16
Total active area:	29 cm ²
Silicon thickness tolerance:	$\pm 15 \mu\text{m}$
Silicon thickness uniformity:	$\pm 5 \mu\text{m}$

SIDAR[28] is based on the Louvain-Edinburgh Detector Array (LEDA)[58] and has been used in multiple recently published studies[49, 48].

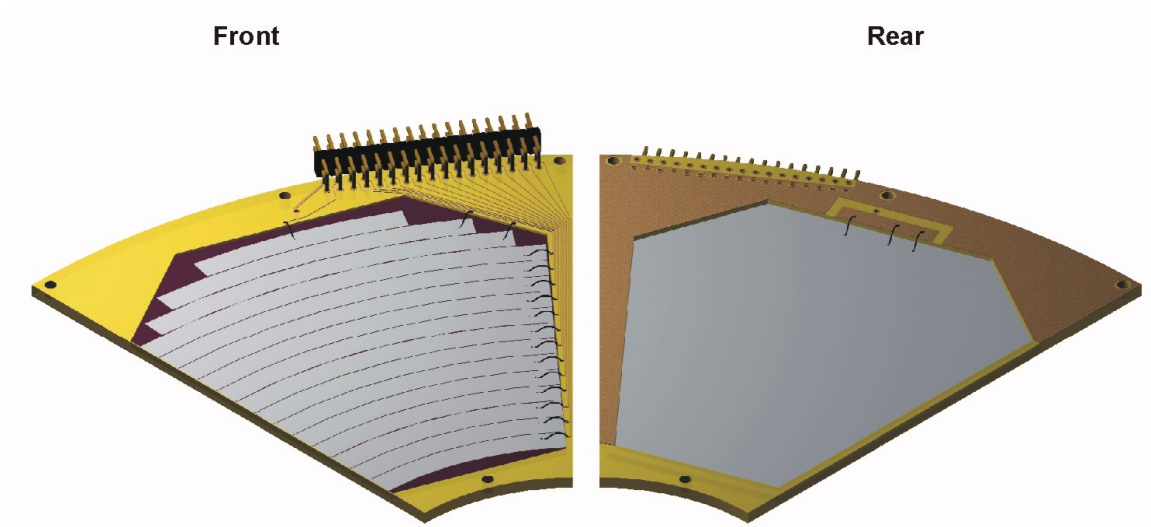


Figure 3.7: Single YY1 detector schematic, used in SIDAR. Drawing from Micron Semiconductors Ltd UK product catalogue[14]

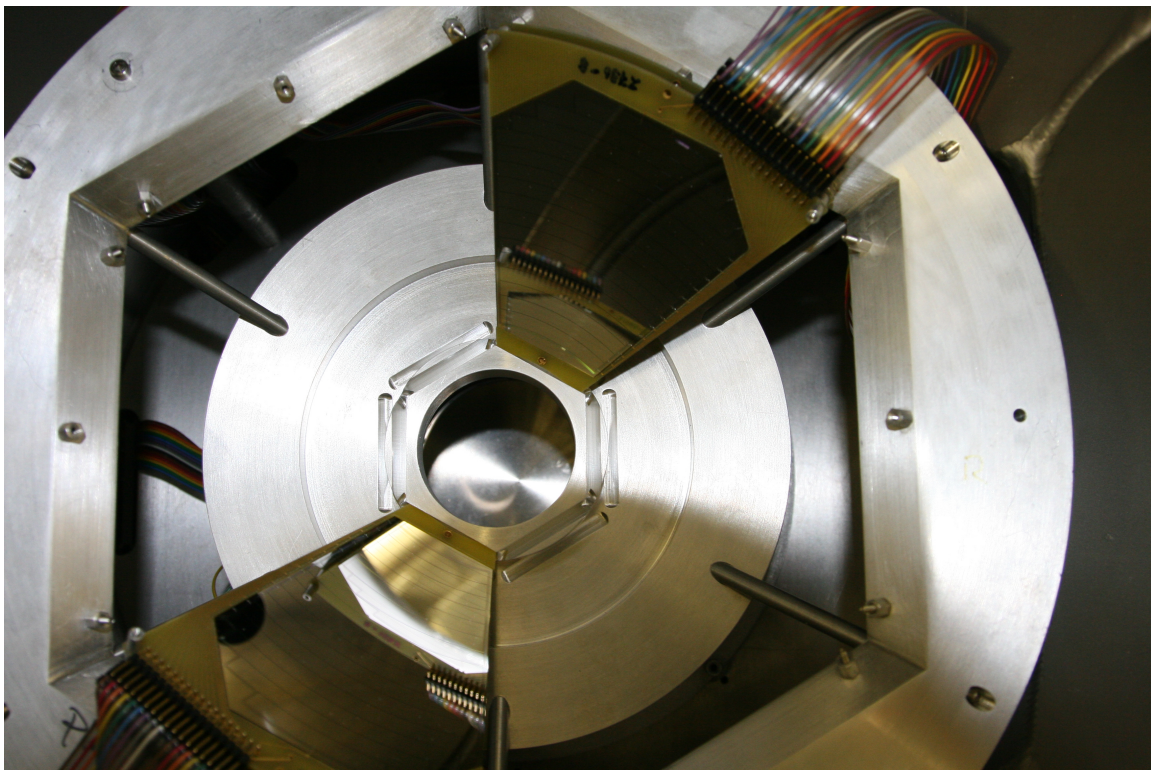


Figure 3.8: Photograph showing the mount used for SIDAR in the “lampshade” configuration. There are 6 slots for detectors, which are tilted by 43° degrees towards the beamline. Two are shown. (Photograph courtesy of Kelly Chipps.)

3.3.3 Electronics

For each particle-on-detector interaction, the signal generated in the detector needs to be recorded by a data acquisition system (DAQ). The signal from each strip in the silicon detectors is read off individually into a charge-sensitive preamplifier[59]. These have differing gains depending on whether from one of the thick E detectors (15 mV/MeV), or thinner ΔE detectors (60 mV/MeV). The signal is then passed into a Rutherford Appleton Laboratories (RAL) shaping amplifier & discriminator, shaping the signal for an analog-to-digital converter (ADC). In addition to signal shaping/amplification, the RAL shapers also have a built-in discriminator, which generates a fast timing signal if the signal is above a certain threshold. This is passed to a gate and delay generator and opens a 6 μs gate for the DAQ to record an event. The DAQ records an ID number related to the detector/strip the signal originated and the voltage from the ADC. These ID numbers are then mapped to the corresponding detector and strip number of original for analysis.

Chapter 4

$^{20}\text{Ne}(p,t)^{18}\text{Ne}$ Calibration and Analysis

In this Section, I discuss the specifics of how the detectors were calibrated, how the tritons were isolated from all measured particles, and the analysis techniques used to interpret these data.

4.1 Experimental setup

This experimental campaign consisted of two separate experimental runs: a short run in August 2013, and a longer run in October 2013. The detectors were not moved between the two experimental runs. For a full breakdown of the length of each run see Appendix A. The thicker E silicon detectors were biased at 210 V, and the thinner ΔE silicon detectors were biased at 25 V. The composition of the target material used for this measurement, $^{\text{Nat}}\text{Ne}$ is shown in Table 3.4. This was a normal kinematics measurement, with a proton beam and a neon jet target. The JENSA jet pressure was maintained at approximately 300 ± 15 psig throughout the experiment. Using Table 4 in Chipps et al[11], a JENSA jet pressure of 300 psig of $^{\text{Nat}}\text{Ne}$ gas corresponds to an areal target density of 2.73×10^{18} atoms/cm², to within 5-10%[11]. Throughout the experiment, there were minor pressure variations in the target, on the order of 1% per 20 minutes, due to small amounts of target material being

lost from the beam line. This was remedied by adding small amounts of ^{20}Ne gas to the system as needed.

Figure 4.1 shows a photograph of the JENSA target chamber in the configuration used for this measurement. Table 4.1 shows a list of the detectors used in this measurement.

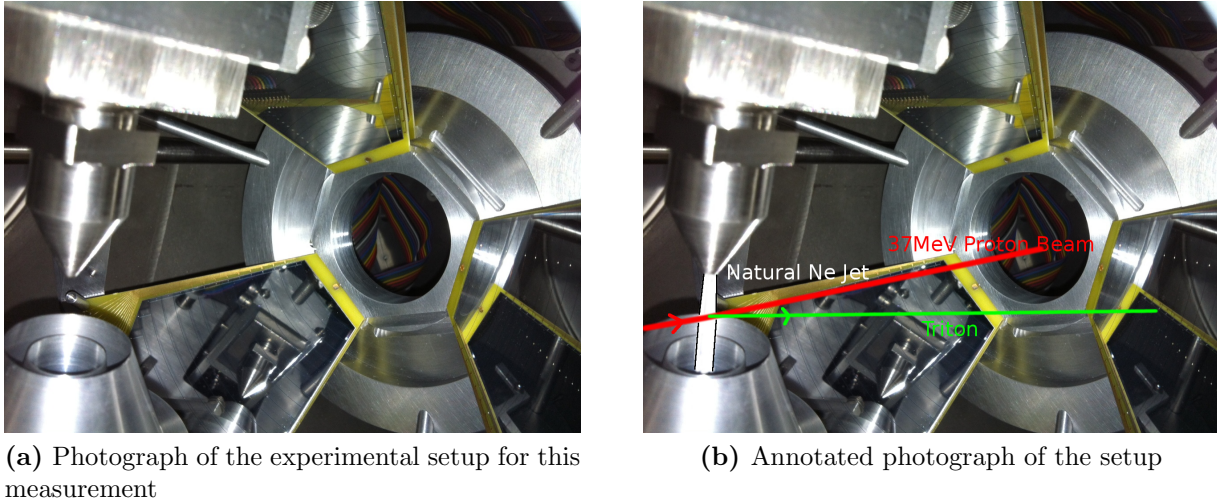


Figure 4.1: The experimental setup for this measurement. (b) has been annotated to show the beam direction, target location and light recoil trajectory

Table 4.1: Serial numbers and thicknesses of the six silicon detectors used in SIDAR for this measurement.

Detector	Serial Number	Thickness
E1	2736-8	1001 μm
E2	2542-14	992 μm
E3	2542-16	998 μm
ΔE1	2558-5	68 μm
ΔE2	2554-2	60 μm
ΔE3	2558-4	67 μm

The proton beam energy of $E_{beam} = 37$ MeV was chosen because of the $^{20}\text{Ne}(p,t)^{18}\text{Ne}$ reaction Q-value. Table 4.2 lists the Q-value of the reaction of interest, and Q-values of other potentially relevant reaction channels, pertinent to this analysis. An energy distribution of tritons at 30° in the laboratory frame can be seen in Figure 4.2 to demonstrate the importance of the choice of E_{beam} .

Table 4.2: Q-value for the reaction channel of interest and other potentially relevant Q-values. As the target used was ^{Nat}Ne , we know approximately 9.5% of the target material is ^{22}Ne . If air somehow bled into the JENSA target system, we could expect to see light recoil nuclei from reactions on ^{16}O and ^{14}N .

Reaction	Ground State Q-value (MeV)
$^{20}\text{Ne}(p,t)^{18}\text{Ne}$	-20.020
$^{22}\text{Ne}(p,t)^{20}\text{Ne}$	-8.644
$^{16}\text{O}(p,t)^{14}\text{O}$	-20.406
$^{14}\text{N}(p,t)^{12}\text{N}$	-22.135

4.2 Calibration

4.2.1 Segmentation of the data and initial calibration

During the time between the two experiments, the gains shifted in the electronics, making it difficult for the data from the August runs and the October runs to be combined. Gain shifts also occurred in some channels over the course of a few runs in the October campaign. In this experiment, the array of six detectors in three ΔE -E telescopes required gain matching for combination, since some of the higher excitation energy states have a much lower cross section when compared to the ground state cross section. The solution to the issue of gain shifting over time was to isolate runs into 5 groups, where the gains in each channel are stable. Table 4.3 shows the five sets of runs and which five runs are contained in each.

This separation was done manually, checking on a run by run basis and looking for large differences in ΔE vs E plots between runs. See Figure 4.3 for an illustrated example. It was discovered that during set 5, there was an issue with the electronics and the peak width in telescope 3 almost doubled, potentially due to a fault with the shaping amplified associated with these channels. For this reason, no events from set 5 in telescope 3 were included in this analysis.

The Bethe-Bloch formula (Equation 3.2) shows that the amount of energy a particle deposits in the thin ΔE detector is dependent on particle velocity and proton number. A heavier particle with the same kinetic energy as a lighter particle will have a lower velocity than the lighter particle. Protons, deuterons and tritons with the same kinetic energy will

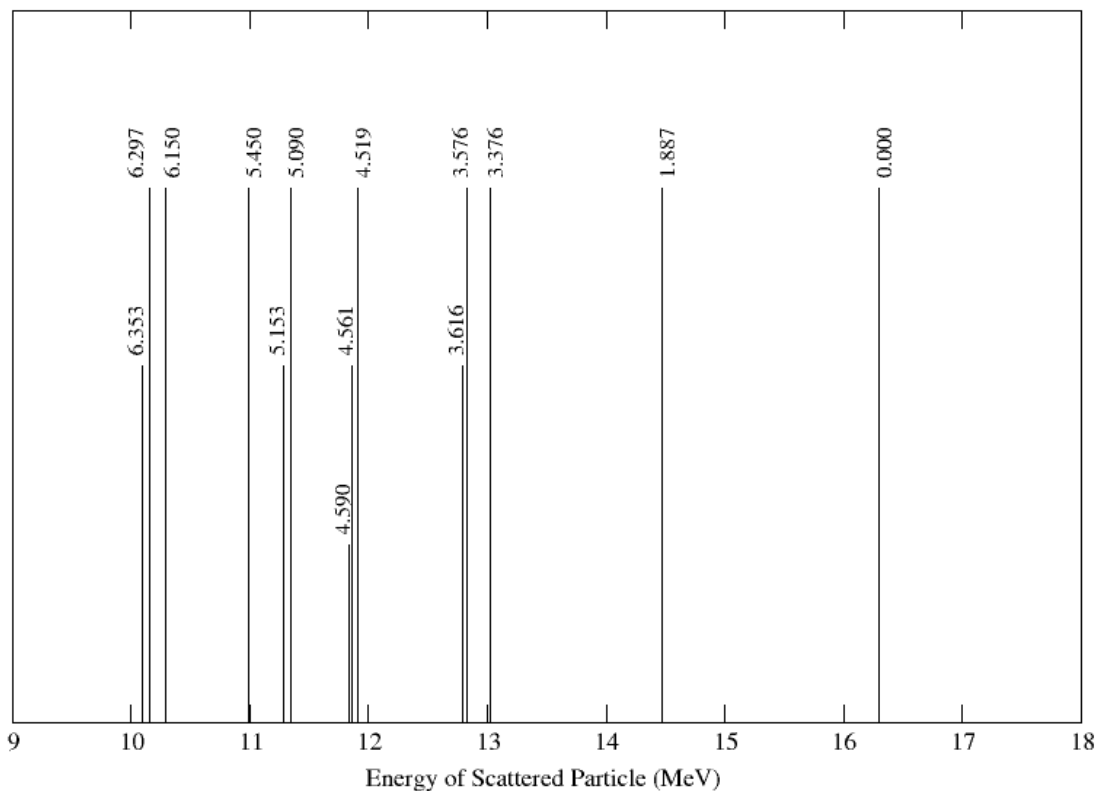


Figure 4.2: Energy distribution of tritons from the $^{20}\text{Ne}(p,t)^{18}\text{Ne}$ reaction at 30° with a 37.0 MeV proton beam. Triton energies are labeled with the excitation energy of the state they correspond to.

deposit different amounts of energy in the ΔE detectors before being stopped completely in the accompanying E detector. Therefore, the use of a thin ΔE detector allows us to separate detected particles of differing mass, by plotting the energy deposited in the ΔE detector against the energy deposited in the E detector. This is demonstrated in Figure 4.5.

SIDAR detectors were calibrated using the 5804 keV α -particle emissions from a ^{244}Cm alpha source. Unfortunately there was disagreement between the calibration runs due to the aforementioned gain shifts, and so these alpha calibration runs were unsuitable for calibration required of these data. Instead, to calibrate the ΔE and E detectors, the ground state from the $^{20}\text{Ne}(p,t)^{18}\text{Ne}$ reaction channel was used.

Because the ground state from the $^{20}\text{Ne}(p,t)^{18}\text{Ne}$ reaction channel was so strongly populated, it could be seen clearly even with only a short set of runs. This allowed, on

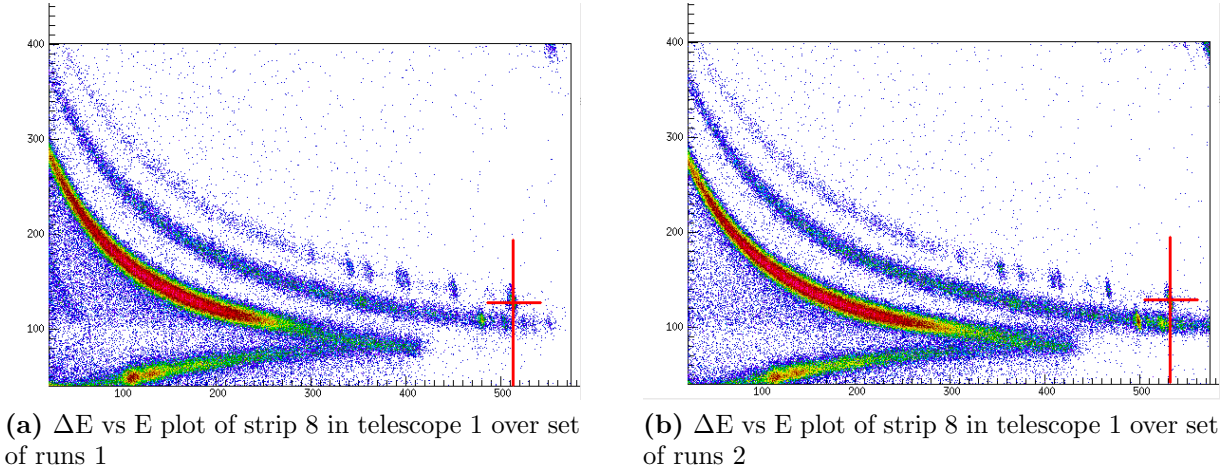


Figure 4.3: ΔE vs E plot of strip eight in telescope 1 for set of runs 1 and 2. The locations of the clusters of counts, representing particles corresponding to states from (p,t) reaction channels, is shifted over the two sets of runs. This means that the sets have to be calibrated individually to facilitate combining these sets of runs. See Figure 4.4 for an example of uncalibrated data being combined.

a set by set, strip by strip basis, to isolate the ground state tritons from the $^{20}\text{Ne}(p,t)^{18}\text{Ne}$ reaction channel in the ΔE vs E plot, and from this, coupled with LISE++ [60] calculations of the energy loss expected in each detector at the corresponding angle to calibrate the ΔE and E detectors. The measured locations of the tritons were then shifted to known, calculated positions on a strip by strip, set by set basis.

This method is considerably more thorough than using a single alpha calibration, as the data are split into subsets and each of those is individually calibrated, then combined after.

Table 4.3: These sets contain a number of consecutive runs where the gain in the measured light products does not seem to shift. This was performed by eye, looking a ΔE vs E plots and deciding points where multiple channel's gains appeared to shift by a noticeable amount.

Group	Runs contained
1	01 to 08
2	12 to 18
3	19 to 22
4	23 to 27
5	28 to 41

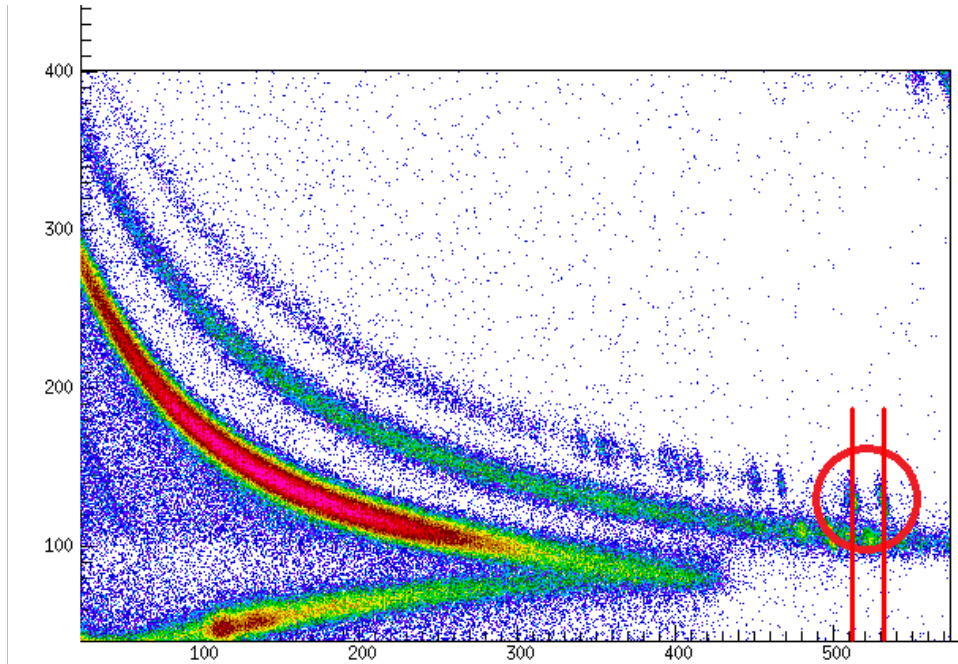


Figure 4.4: Figures 4.3a and 4.3b combined. Location of the tritons corresponding to the ground state of the $^{20}\text{Ne}(p,t)^{18}\text{Ne}$ reaction channel have been circled in red. Both groups of particles represent the ground state tritons, but because these data are uncalibrated, they are in different locations on the ΔE vs E plot.

This helps to minimize the effect of even minor gain shifts, and thus allows us to achieve a better resolution than if we just used a single alpha run.

Triton isolation

The primary reason for using telescopes comprised of a thin silicon detector on top of a much thicker silicon detector is particle identification. As the detectors individually cannot discriminate between charged light ions from multiple reaction channels such as (p,p), (p,d) and (p,t), we need a way to separate the nuclei of different mass and charge, and as discussed earlier, using two detectors of differing thickness allows us to do this as particles of varying masses will lose different amounts of energy as they pass through the same material. Figure 4.5 shows the energy deposited in the thin ΔE detector vs the energy deposited in the thick E detector, demonstrating a clear separation between the protons, deuterons and tritons.

In order to identify tritons, a calibrated ΔE vs E plot was generated, and a gate that encompasses only the events corresponding to the triton kinematic line was created. These

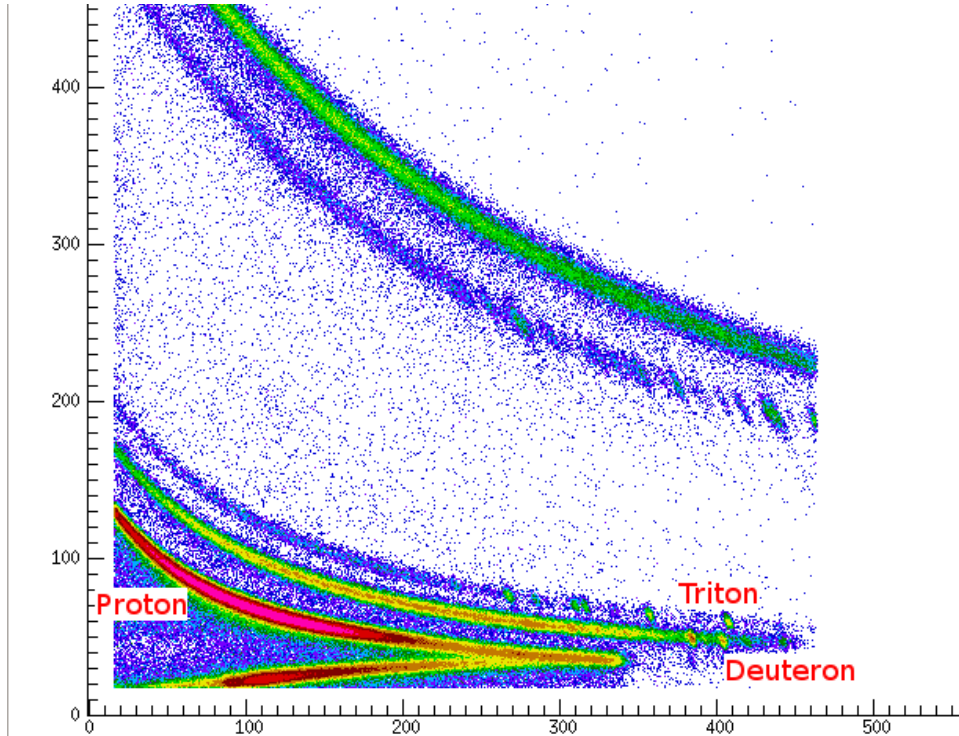


Figure 4.5: Particle identification plot with the proton, deuteron and triton kinematic lines labeled.

stored coordinates select only events with a triton, effectively rejecting anything else. Figure 4.6 shows the gating procedure.

Shadowing during experimental run

Due to the location of telescope 1, part of the detectors were shadowed by the JENSA gas receiver. This was obvious in the experimental data, showing a reduction in count rate (varying from strip to strip) when compared with the other two detector telescopes. For this reason, strips 9 through 16 of telescope 1 were excluded from this analysis. Figure 4.7 displays an example of the shadowing seen in Telescope 1.

4.2.2 Solid angle calibration

Solid angle coverage used for this measurement were calculated using two solid angle calibration runs, one for the ΔE detectors and one for the E detectors. These runs were performed during the October segment of the experiment using a calibrated ^{244}Cm source

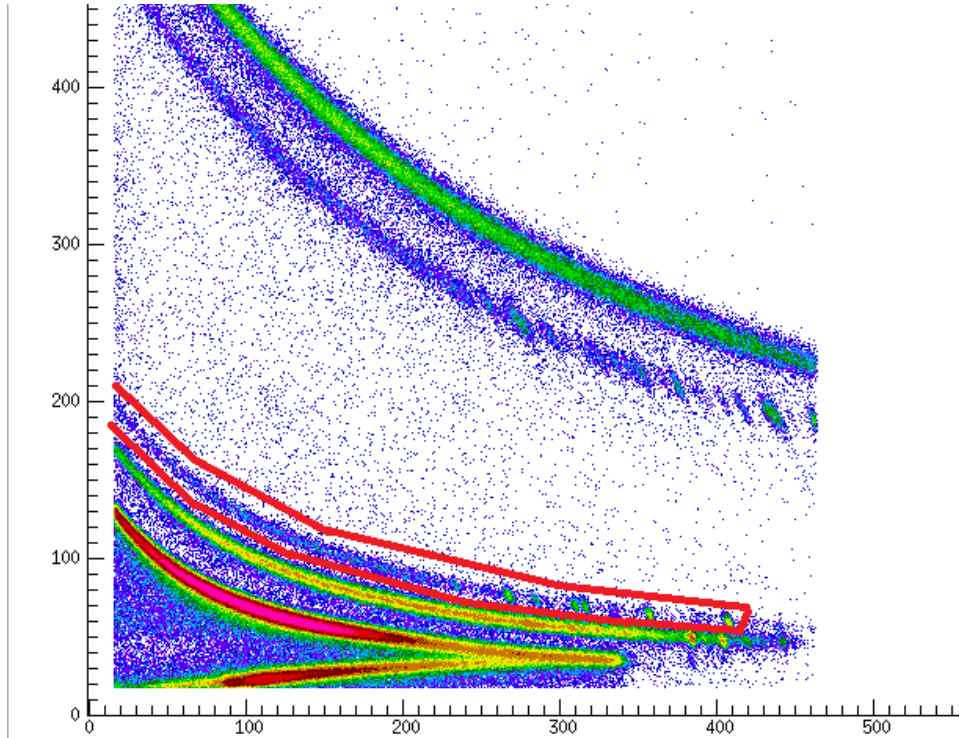


Figure 4.6: Demonstration of the gating procedure. A line is drawn around the triton line, and in the analysis code this region is used as gate for triton events. The red line representing the gate in this image is much larger than the actual gates used and is that way only to assist the reader. The lines comprising the gates have been enlarged to better display the gate.

with known activity. Using the half-life and the calibrated activity, the source's emission rate on the day of measurement was calculated. The source was positioned as close to the target location as possible, which was about 1 cm forward of the JENSA target location. Assuming the total number of alpha particles per second are released isotropically from the target location, the number of counts measured in each strip of each detector per second gives a measurement of the solid angle coverage of each strip.

Shadowing was seen in telescope 2, potentially due to an off-axis source position during the angle calibration runs. For this reason, only measurements from telescopes 1 and 3 were used. Figure 4.8 shows the results from the ΔE solid angle run, while Table 4.4 shows the solid angle of each strip.

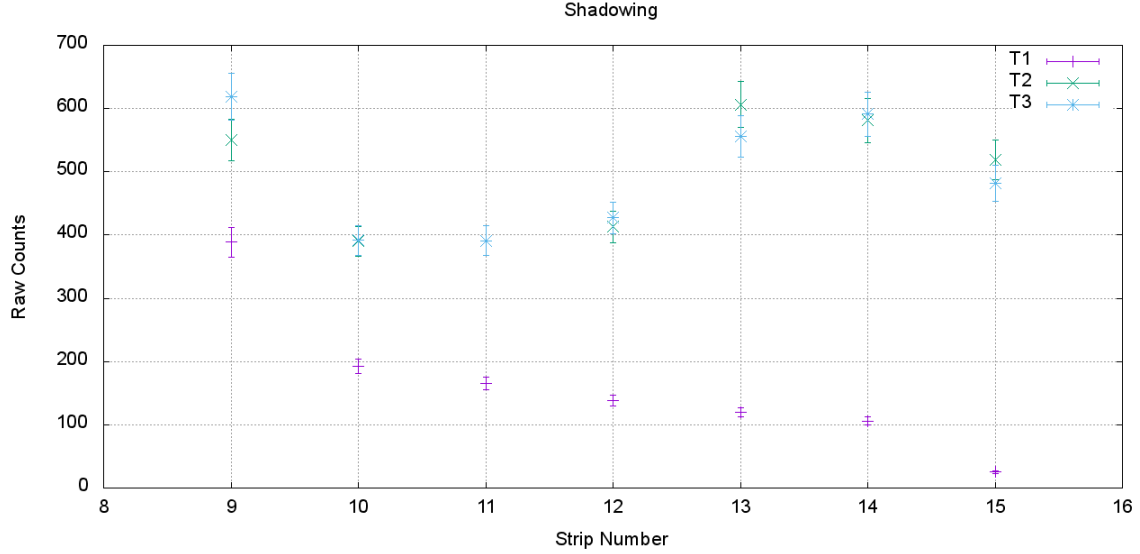


Figure 4.7: Raw counts of ground state tritons from the $^{20}\text{Ne}(p,t)^{18}\text{Ne}$ reaction channel, from run set 2, over strips 9 - 15 from all three telescopes. It can be seen that while telescope 2 and 3 are in good agreement with each other, there is a clear discrepancy with the raw counts in telescope 1. This is due to the fact that the outer strips of telescope 1 was shadowed slightly by the JENSA receiver.

4.2.3 Secondary gain coefficients

The initial calibration only used the ground state of the $^{20}\text{Ne}(p,t)^{18}\text{Ne}$ reaction channel. A single point calibration assumes the origin, but an offset may exist, and a multi-point calibration needs to account for this.

For this section, I will refer to the strip in the E detector as the i index, and the strip in the ΔE as the j index. Initially, particle identification plots were generated for 5 possible combinations, (i,j) , $(i,j+1)$, $(i,j-1)$, $(i,j+2)$ and $(i,j-2)$. However, the number of events in the $(i,j+2)$ and $(i,j-2)$ combinations was of the order 0.1% of the total events, so only the (i,j) , $(i,j+1)$ and $(i,j-1)$ combinations were taken into account. These particle identification plots were gated on individually, and if an event was found in the gate it was added to a triton spectrum for that particular combination. For each of these to be combined into a single index, this required secondary gain corrections for each of the indices, for each of the telescopes and for each of the sets. The dispersion for each of the histograms was chosen so that each channel represents 5 keV.

Table 4.4: Solid angle values used for each strip in each telescope.

Strip	Solid angle per strip (msr)
1	10.990
2	12.446
3	13.984
4	15.594
5	17.897
6	18.973
7	20.703
8	22.430
9	24.129
10	25.770
11	27.327
12	28.772
13	28.525
14	25.697
15	21.466

Although each strip covers a small range of angles, for the purposes of this analysis, the center point of the strip in the lab frame was adopted as the lab angle value for that strip in kinematics calculations. Kinematics calculations were performed for each strip taking i as the index, and using energies listed on ENSDF[2] for each of the excited states in ^{18}Ne . These kinematic calculations can be used to identify states in ^{18}Ne in the calibrated spectra. For each of the combinations, in each set, for each telescope, a triton spectrum was generated and, using kinematic calculations for the corresponding angle, tritons from the ground state, and the $E_x=1887$ -, 3376 -, 5450 - and 6150 keV states were identified based on triton energy. These were each fit individually as a single Gaussian peak. The means were then fit linearly against the kinematically calculated location to give a secondary gain coefficient, which allows us to combine the multiple telescopes with the best possible resolution with these data. If there were issues with the strip for just a single set, for example, one of the ΔE strips stopped working for a number of runs, that combination was switched off for that specific set (Gain coefficients of 0 applied to completely remove that channel).

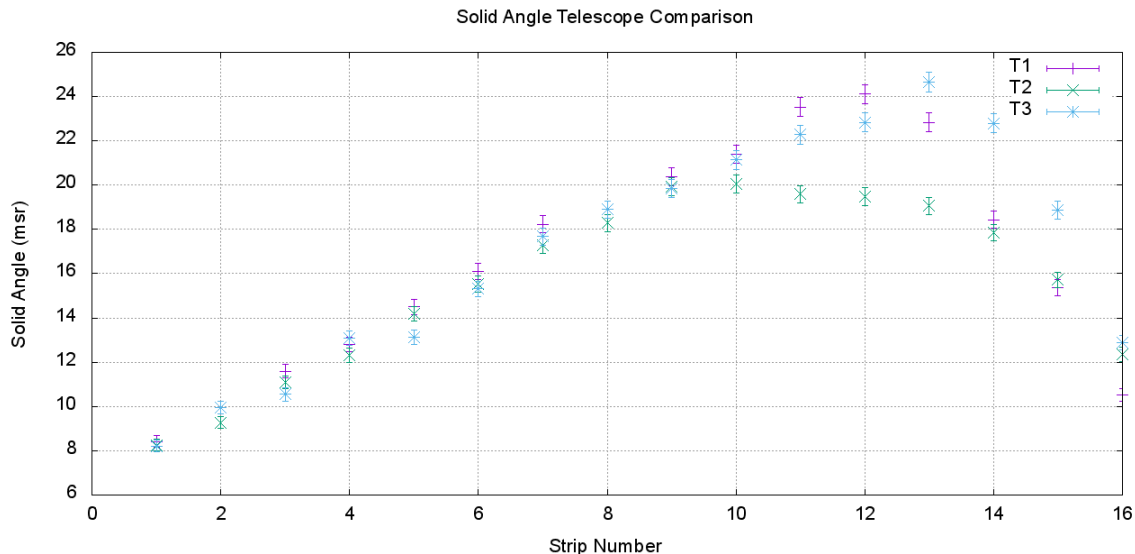


Figure 4.8: Results from the ΔE solid angle run. Telescope 2 was shadowed between strips 10 and 15, and telescope 1 was shadowed slightly for the last 3 strips, potentially due to an off-axis source position. There is good agreement between all three telescopes at lower angles. It is also important to note that these values vary slightly with the values in Table 4.4, because the ΔE detectors were not at the same location as the E detectors and therefore had a slightly different solid angle coverage. The difference is accounted for by including the standoff distance between the ΔE and E detectors.

4.3 Residuals

Five states were initially used in the calibration, the ground state, and the 1887-, 3376-, 5450- and 6150-keV excited states. For each set of runs, and each strip combination, the five peaks corresponding to those states were fit as an individual Gaussian.

The calibration used literature values of the excitation energy to calculate the kinetic energy of tritons from the $^{20}\text{Ne}(p,t)^{18}\text{Ne}$ reaction at each angle. These calculated values were also used to check the calibration. Extracted locations of the peaks after calibration were compared to the calculated energy and these residuals are plotted in Figures 4.9 and 4.10.

These residuals are expected to be scattered around zero, within error bars, as can be seen in Figure 4.9 for the ground state. If the residuals are offset from zero, which was the case for the first excited state, shown in Figure 4.10, then this indicates that the measured

value for excitation energy differs from the value in the literature. Despite the shift being relatively small, it was still enough to skew the calibration.

The original publication[1] reporting this value used Ge(Li) detectors to measure gamma rays from nuclei in the first excited state de-exciting to the ground state. An uncertainty of 0.2 keV is reported for this excitation energy. No other high resolution study of this state could be found in existing literature.

As there was disagreement with the present work and the residuals for the first excited state in ^{18}Ne , this state was not used in the final calibration.

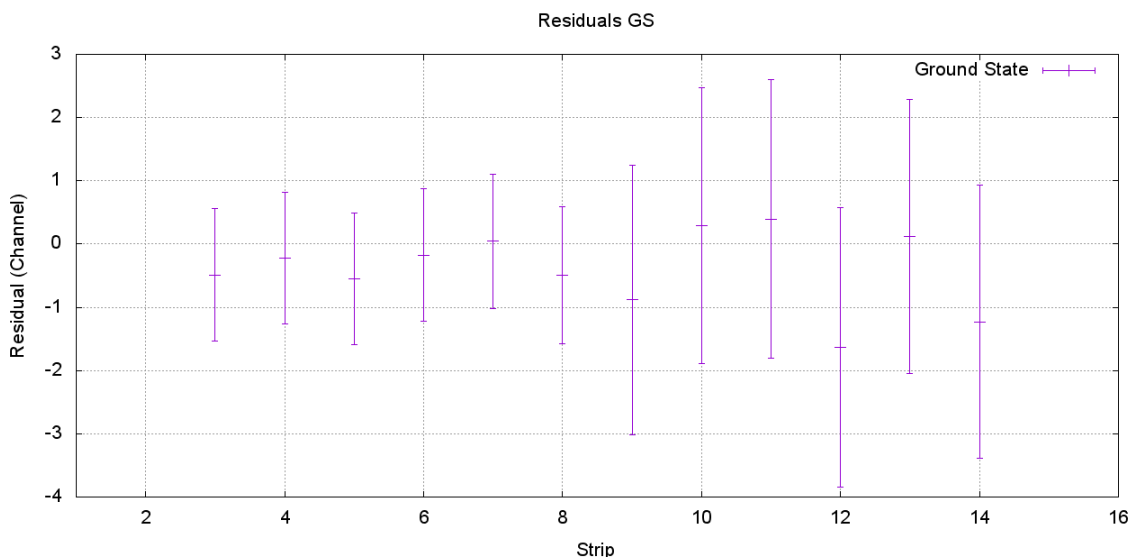


Figure 4.9: Residuals for the ground state of ^{18}Ne . The residuals are scattered around zero

4.3.1 Strip downtime corrections

To extract relative cross sections, it is vital that each strip is active for the same integrated beam dose over the entire experiment. That is, if one strip, for example strip 4 in E2, stops working due to an electronics failure for a number of runs, the total number of events for the angle strip 4 represents will be lower than if the strip were active for the same dose as other strips.

To account for these effects, strips were identified that had no technical issues throughout the entire experimental campaign. Statistics in these strips were sufficient to measure the ground state tritons from the $^{20}\text{Ne}(p,t)^{18}\text{Ne}$ reaction channel in each of the 5 set of runs.

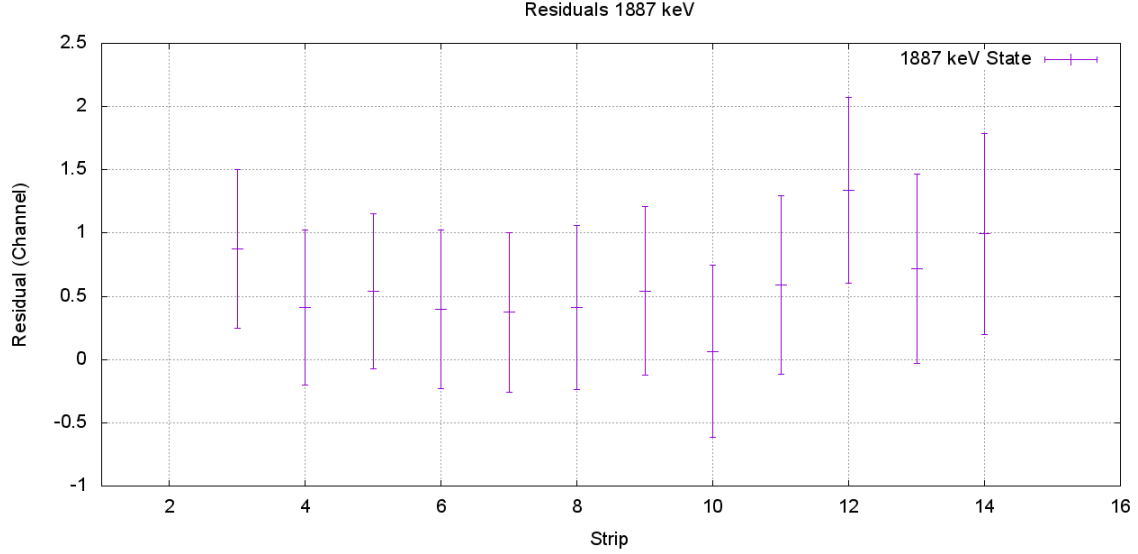


Figure 4.10: The residuals for the first excited state in ^{18}Ne ($E_x = 1887$ keV). The offset of all points from zero in the same direction indicates a disagreement with literature values for this excitation energy of this state.

These give a number of counts in the ground state, in multiple strips active for the entire experimental campaign. Since the target location did not change, and the detector location did not change, then the number of counts in the ground state tritons of a particular strip gives an indication of the total beam current on target for that set of runs.

Since we had multiple strips which had no electronics issues, we have multiple independent measurements of the number of interactions that each set of runs represents for the total data set. This then gives a correction factor to correct for any strip that experienced issues for a small number of runs.

Because the ground state was well populated and we are comparing multiple independent measurements, this is a rigorous way of evaluating the number of interactions each set of runs represent.

Let us say that N_x^n is the number of ground state tritons for strip n over set of runs x. If strip n, in both the E and ΔE was active for the entire set of runs (That is, no issues in recording events), then the ratio is the same for each strip n:

$$\frac{N_x^n}{N_{total}^n} \quad \text{Where:} \quad N_{total}^n = \sum_x N_x^n \quad (4.1)$$

Over this experimental campaign strips 5, 6, 7 and 8 were active completely through all 5 sets of runs in for the first 2 telescopes, so these were used to calculate the corrective factors applied to other strips which did encounter downtime issues at some point through the campaign. Strip 4 was only used in telescope 1, as there was an issue with strip 4 in telescope 2 for the first set of runs. As discussed earlier, telescope 3 had resolution issues for set 5, so all of telescope 3 was excluded from the downtime correction calculations. From above, it should follow that for any set of runs x:

$$\frac{N_x^4}{N_{total}^4} = \frac{N_x^5}{N_{total}^5} = \frac{N_x^6}{N_{total}^6} = \frac{N_x^7}{N_{total}^7} = \frac{N_x^8}{N_{total}^8} \quad (4.2)$$

For each of the 5 sets of runs, the ground state tritons from the $^{20}\text{Ne}(p,t)^{18}\text{Ne}$ reaction channel were fit using a single Gaussian. The area, N_x^n was recorded. Tables 4.5 and 4.6 show the values for $\frac{N_x^n}{N_{total}^n}$ for each telescope.

Table 4.5: Downtime correction factors for telescope 1.

Strip (n)	N_1^n/N_{total}^n	N_2^n/N_{total}^n	N_3^n/N_{total}^n	N_4^n/N_{total}^n	N_5^n/N_{total}^n
4	0.1965	0.2432	0.1555	0.1145	0.2903
5	0.1914	0.2369	0.1575	0.1224	0.2918
6	0.1864	0.2327	0.1648	0.1228	0.2933
7	0.2052	0.2364	0.1619	0.1137	0.2828
8	0.2009	0.2257	0.1605	0.1212	0.2917

Table 4.6: Downtime correction factors for telescope 2.

Strip (n)	N_1^n/N_{total}^n	N_2^n/N_{total}^n	N_3^n/N_{total}^n	N_4^n/N_{total}^n	N_5^n/N_{total}^n
5	0.1876	0.2358	0.1653	0.1202	0.2911
6	0.1735	0.2378	0.1652	0.1167	0.3068
7	0.1465	0.2411	0.1799	0.1188	0.3137
8	0.1449	0.2573	0.1776	0.1260	0.2942

The value for each N_x^n for each strip and telescope is shown in Appendix B, along with the uncertainty of each value. The final averaged values and uncertainties are shown in Table 4.7

Table 4.7: Final correction factors. These factors represent the number of raw counts in the ground state of $^{20}\text{Ne}(p,t)^{18}\text{Ne}$ as a ratio to the total number of counts recorded in the corresponding strip. $\sum N_x^n/N_{total}^n = 1$

Set	Averaged N_x^n/N_{total}^n	% Uncertainty
1	0.1814	3.12
2	0.2385	2.81
3	0.1653	3.28
4	0.1197	3.77
5	0.2951	2.64

These were used to correct for downtime of any strip over individual sets of runs. The downtime correction factors applied to each strip are shown in Table 4.8

4.3.2 Contamination

Between experiments, the JENSA system is evacuated of any leftover gas before changing target material. This leaves only two potential contaminants: Reactions on ^{22}Ne (As the target gas used was natural neon, comprised of 90.5% ^{20}Ne and 9.5% ^{22}Ne) and air potentially leaking through one of the many components of the JENSA system. Table 4.2 shows the Q-values of potential contamination we should expect to see in the triton spectra. The Q-value for (p,t) reactions on ^{22}Ne is almost 12 MeV different to (p,t) reactions on ^{20}Ne . This is not the case for tritons from the $^{16}\text{O}(p,t)^{14}\text{O}$ and $^{14}\text{N}(p,t)^{12}\text{N}$ reactions, although as the Q-values are very similar to $^{20}\text{Ne}(p,t)^{18}\text{Ne}$. This means that, if air did leak into the system through a component of the JENSA system, we might expect to see some tritons from those reaction channels in our spectra.

Using air contamination as intrinsic angular calibration

The polar angle of each strip in the laboratory was initially calculated using distance measurements taken inside the chamber at the time of the experiment. With air contamination in the ^{20}Ne target, measurement of tritons from the $^{16}\text{O}(p,t)^{14}\text{O}$ and $^{14}\text{N}(p,t)^{12}\text{N}$ can be used alongside measurements of tritons from $^{20}\text{Ne}(p,t)$ to give an intrinsic angular calibration.

Table 4.8: These final downtime correction factors take into account which strips were off for whichever runs and are the values that the final fits need to be applied to correct for strip downtime.

Strip	Downtime correction factor (ϵ)
1	0.1475
2	0.0
3	0.1708
4	0.1271
5	0.0984
6	0.0984
7	0.0984
8	0.0984
9	0.1475
10	0.1678
11	0.1475
12	0.2383
13	0.1903
14	0.1528
15	0.3127

Since the nuclei involved in these contamination reactions are of different atomic masses, the energy change per angle due to the kinematics will be different, that is to say that the energy change per degree in lighter nuclei is greater as the angle increases when compared to heavier nuclei. This means that as we move from lower angles to higher angles in the lab frame, the tritons which we measure from states in ^{12}N will appear to “move through” some of the tritons from states in ^{18}Ne . This is very useful for angular calibration, as the precise point that this happens is determined mathematically. Using the locations of the peaks at multiple angles, it is possible to calculate the point where the kinematic lines cross, providing intrinsic angular calibration. Calculations are shown in Figure 4.11 and measurements from the data are shown in Figure 4.12

Finding the point of intersection of the calculated kinematics lines, A and B, is the angle where the two triton lines from the two origins overlap in the triton spectra. The two become unresolvable at strip 6 in the triton spectra, therefore this places strip 6 at that crossing point. As can be seen in Table 4.11, when comparing the intersection of C and D,

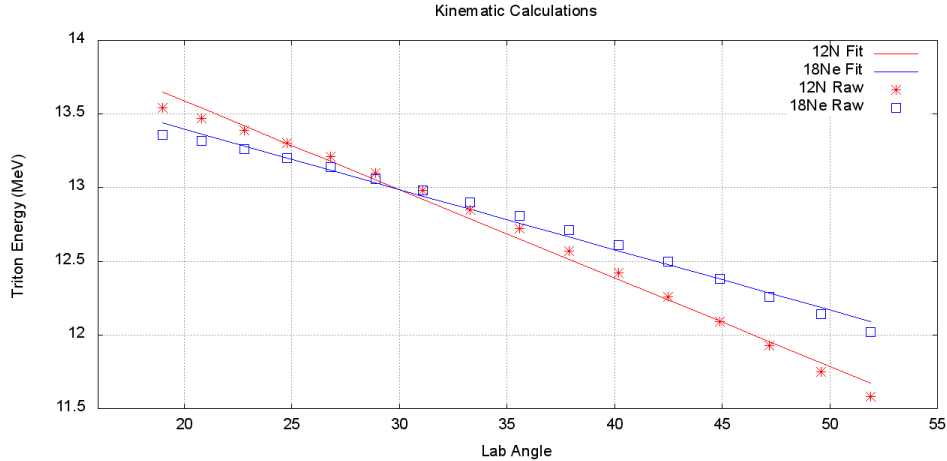


Figure 4.11: Kinematic calculators for tritons from the 2nd excited state in ^{18}Ne (Blue) and the first excited state in ^{12}N (Red). Across the range of angles studied, the behavior is approximately linear. Linear fits were performed on these points and are displayed as lines. The parameters of the fits are given in Table 4.9.

Table 4.9: Parameters of calculated kinematic lines for tritons measured from two of the intersecting states. These used an angular range of 18° to 52° in the laboratory.

Reference	Triton from State	Slope (MeV/lab frame degree)	intercept (MeV)
A	^{18}Ne 2nd	-0.04093	14.2163
B	^{12}N 1st	-0.06001	14.7878

and C and E, the crossing points are around 2° away in the lab frame. The difference of 2° demonstrates the initial calculation of the laboratory angles was incorrect.

4.3.3 Fitting

The result of the calibration procedures is to create a single histogram for each angle. Since the particle-bound structure of ^{18}Ne is well studied (See Tables 1.2 and 1.3), the energies of most of these states are known with a reasonable certainty, allowing accurate identification of the peaks observed in this work. Several of the states observed in this experiment appear as one peak in the spectra because of a combination of the angular coverage of each of the strips and the resolution of the silicon detectors.

States above the particle threshold will have a natural width, which when combined with the detector resolution produces broader peaks. These particle widths also do not

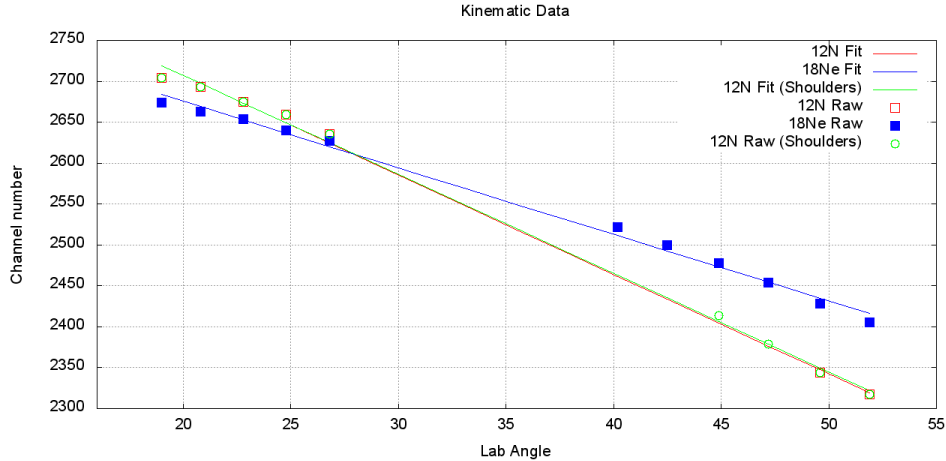


Figure 4.12: The extracted channel locations of tritons identified from the 2nd excited state in ^{18}Ne (Blue) and the first excited state in ^{12}N (Red and Green). Linear fits were performed through the extracted points and are shown as lines on the figure. The difference between the green and red points arises from the two points at approximately 45° and 47° . These peaks were identified as shoulders, and two fits were performed, one ignoring the shoulder points (Red) and one including them (Green). This resulted in a slight difference in crossing point (See Table 4.10).

Table 4.10: Parameters of measured kinematic lines for tritons measured from the two intercepting states. Fit E takes the same strips as D, but 2 additional points are included where the nitrogen triton peak is not fully independent from the neon triton peaks.

Reference	Triton from State	Slope (MeV/lab frame degree)	intercept (MeV)
C	^{18}Ne 2nd	-0.04061	14.1896
D	^{12}N 1st	-0.06079	14.7519
E	^{12}N 1st (Shoulders)	-0.06039	14.7430

have a Gaussian structure, but instead are Lorentzian. To treat these properly would require unbound states to be fit with a convolution integral of a Gaussian to account for the detector resolution and a Lorentzian to account for the particle width. However, for the particle unbound states we observe, the particle widths are much smaller when compared to the detector and angular spread components, and therefore we ignore the Lorentzian contributions and fit each of the states as a Gaussian.

Using literature values gives a good starting point to identify each of the observed peaks, and for the singlet states the starting location for the fitting procedure. In the case of multiple states in close proximity, which cannot be resolved easily, we make an additional assumption

Table 4.11: Comparisons of the expected crossing point of the kinematic lines, and a comparison of the crossing points calculated using the assumed angles of each strip. The calculated crossing points show that the measured distances were incorrect, and the crossing strip, strip 6, should be at the calculated crossing point of around 30° in the lab frame. The intersection of A and B is the calculated crossing point, while intersection of both C and D, and C and E came from measurements. The difference of 2° demonstrates the initial calculation of the laboratory angles was incorrect.

Intersection of references	Crossing angle
A and B	29.953
C and D	27.834
C and E	27.978

that the level energies are known and fix the expected triton energies of the constituent states of the doublets. Since the main goal of this experiment is to extract angular distributions, fixing the peak locations to extract the angular distributions is reasonable.

Fitting was performed in ROOT[61], using a custom function for each strip. Since each spectrum has multiple peaks from varying sources, using a custom function has multiple benefits compared with using the in-built functions, it allows us to model the background more accurately, and it allows the peaks from the same reaction channel to either vary or be fixed in width. All parameters were constrained to be positive, and allowed to vary wherever possible. No peak heights were locked, only constrained to be positive.

The custom function in ROOT was parameterized using 14 Gaussian peaks with shared widths for the ^{18}Ne tritons. Since the shape of each triton peak is assumed to be Gaussian, the width of each peak corresponding to tritons from the population of ^{18}Ne at each angle should be the same. This width parameter was allowed to vary, and each ^{18}Ne peak used the same width. Peak locations were initialized to a calculated expected channel using literature energies and then either allowed to vary within a small range of channels (± 2 to 6, varying based on uncertainties to literature values), or fixed in place. Peaks corresponding to the ground state and first excited state in ^{12}N were treated in the same way and allowed a range of ± 4 channels. The peak corresponding to the ^{14}O ground state was also treated in this way. Three linear fits were used for the background. Since this work covered such a large energy range and both particle bound states and particle unbound states, the background

does not vary linearly over the entire range, though when split up into smaller ranges, it can be approximated to linear over those ranges.

Figure 4.13 shows a fit for a single angle, Figure 4.14 shows the same but displays the constituent Gaussian peaks, and an example of how doublets were treated in the fitting procedure is shown in Figure 4.15. Table 4.12 shows whether mean locations were allowed to vary or were fixed in the fitting procedure

Binning was adjusted on a strip by strip basis, depending on the number of counts in each strip and resolution. Table 4.13 shows the energy per bin for each strip used in through the fitting procedures.

Table 4.12: List of whether the mean of the state was fixed in the fit, or allowed to vary

E_x (keV)	Fixed or Variable mean
0000	Variable
1887	Variable
3376	Variable
3576	Variable
3616	Fixed
4519	Variable
4590	Variable
5090	Fixed
5146	Fixed
5453	Variable
6150	Variable
6297	Fixed
6350	Fixed

With the values for the amplitude, mean and sigma for each peak, and with the background properly taken into account, the area of that peak and uncertainties were calculated. Repeating this process for each peak in each strip gives the area at each angle, and thus a raw angular distribution for each measured state.

To produce an angular distribution the solid angle of each strip was used, corrected for the center of mass, and a final adjustment was made to account for dead strips using the downtime correction values calculated earlier:

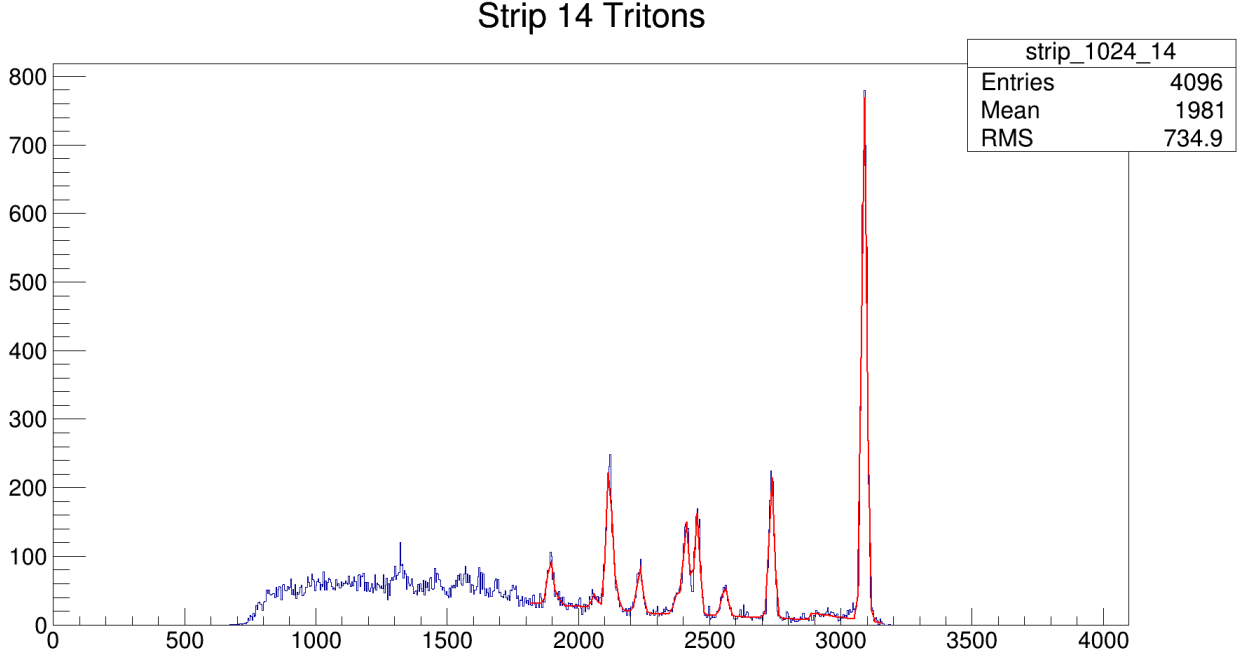


Figure 4.13: This is a single fit for strip 14 over the entire range shown by the red fit line.

$$\frac{C_{raw}}{(1 - \epsilon)} \frac{\sigma}{\frac{d\sigma}{d\Omega}} = C_{final} \quad (4.3)$$

Where: C_{raw} is the number of raw counts in a peak, ϵ is the downtime correction factor, $\frac{d\sigma}{d\Omega}$ is the laboratory-to-center of mass solid angle conversion factor, σ is the laboratory solid angle factor, and C_{final} is the final corrected value of counts per milliradian.

C_{final} is equivalent to a differential cross section for a corresponding angle and strip. This value was calculated for each excited state measured, at each angle, and will be compared to DWBA calculations in Chapter 5. The 15 raw triton spectra, one per strip, used for this analysis are shown in Figure 4.16. For all plots in Figure 4.16, the y-axis is number of counts, and the x-axis is channel number (approximately 5 keV per channel), with smaller triton energies corresponding to lower excitation energy states.

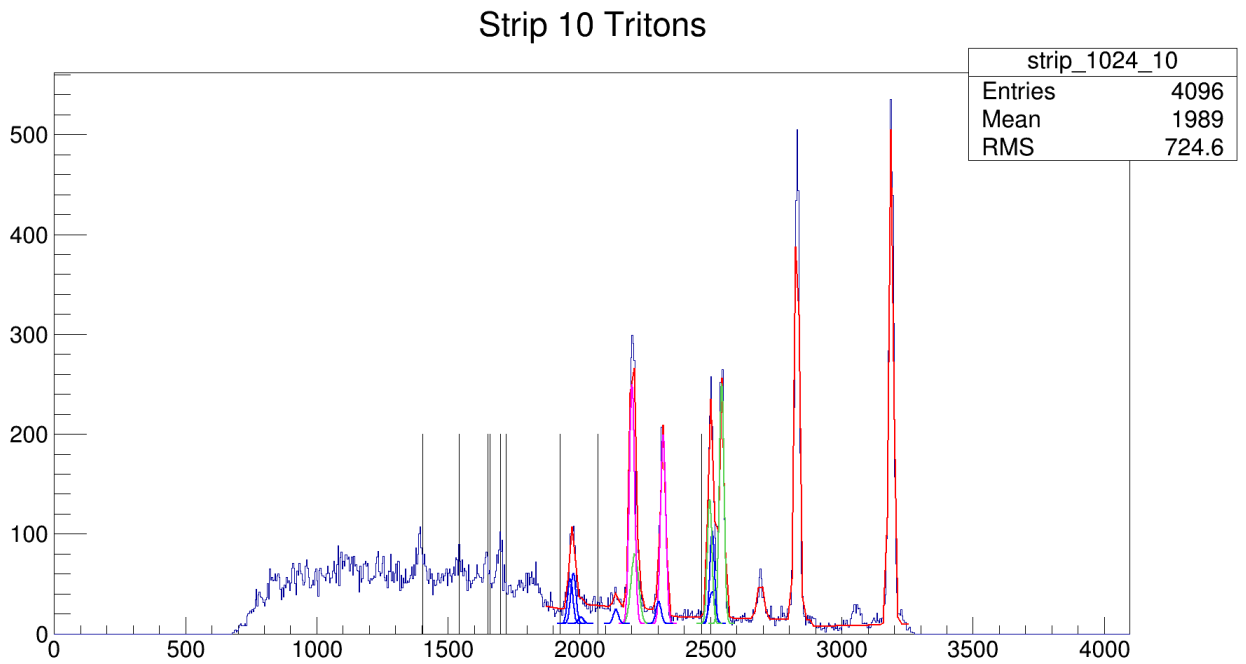


Figure 4.14: This is the entire fit for strip 10, with the individual component gaussians shown along the length of the entire fit. These were added post-fit and are just representative of the constituents of the fit. Background in these display curves is not modeled accurately, while it is in the actual fit. The thin vertical black lines are representative of states in ^{18}Ne , ^{12}N and ^{14}O in current literature.

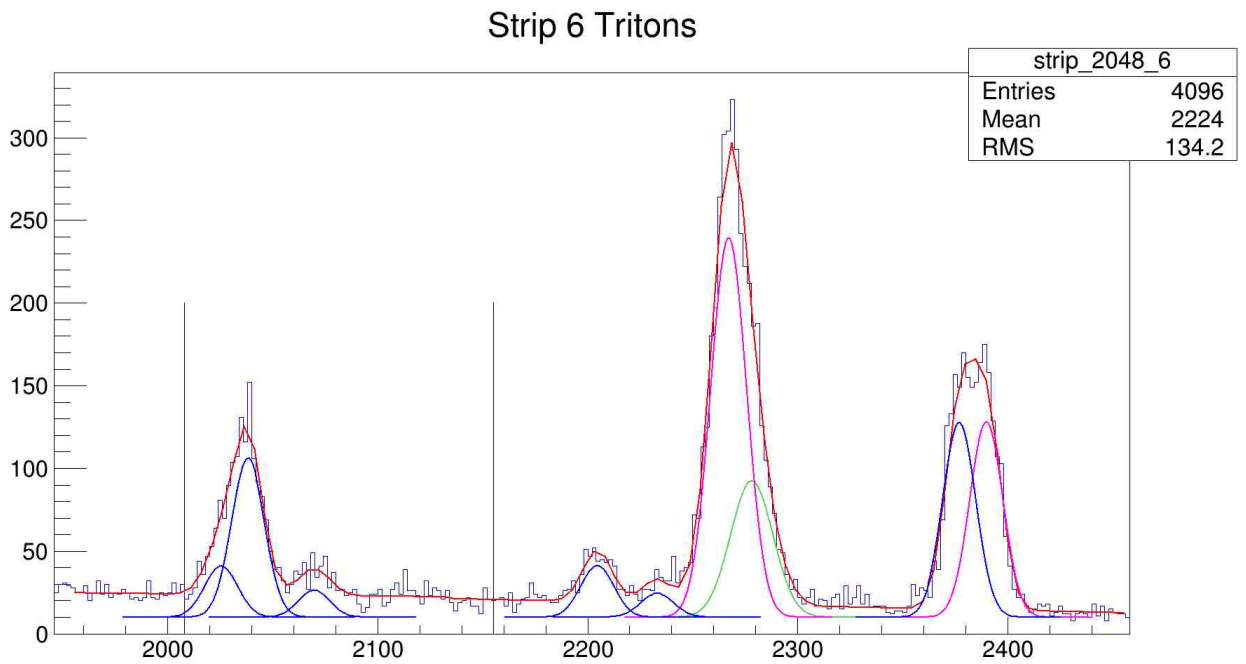


Figure 4.15: A segment of the fit used for strip 6. The red line is the line fit over the entire range, while the blue, green and pink lines represent constituents of the overall fit. These were generated post-fit and are only to guide the eye as to the constituents of the doublets and how they were fit individually. Background estimations shown in these fits is not representative of the background estimations in the actual fit (red line). X axis is channel number, where 1 channel is approximately 5 keV, Y axis is counts per bin

Table 4.13: Listed are the values of energy per bin used when fitting each strip. Binning was adjusted on a strip by strip basis to account for the changes in statistics and the changes in resolution. The energy per channel is always approximately 5 keV, changes in binning are changes in the number of adjacent channels combined

Strip	Energy per bin (keV)
1	20
2	10
3	20
4	10
5	10
6	10
7	10
8	10
9	20
10	20
11	20
12	20
13	20
14	20
15	20

Table 4.14: Q-Values used by larelkin[15] for kinematic calculations

E_x	Q-value
0	-20.020
1887	-21.907
3376	-23.396
3576	-23.596
3616	-23.636
4519	-24.539
4561	-24.581
4590	-24.610
5090	-25.110
5146	-25.166
5435	-25.455
6150	-26.170
6297	-26.317
6353	-26.373

Table 4.15: Laboratory angles for each of the corresponding strips.

Strip	Lab Angle
1	19.69
2	21.64
3	23.66
4	25.75
5	27.89
6	30.09
7	32.35
8	34.65
9	36.99
10	39.37
11	41.78
12	44.20
13	46.63
14	49.07
15	51.49

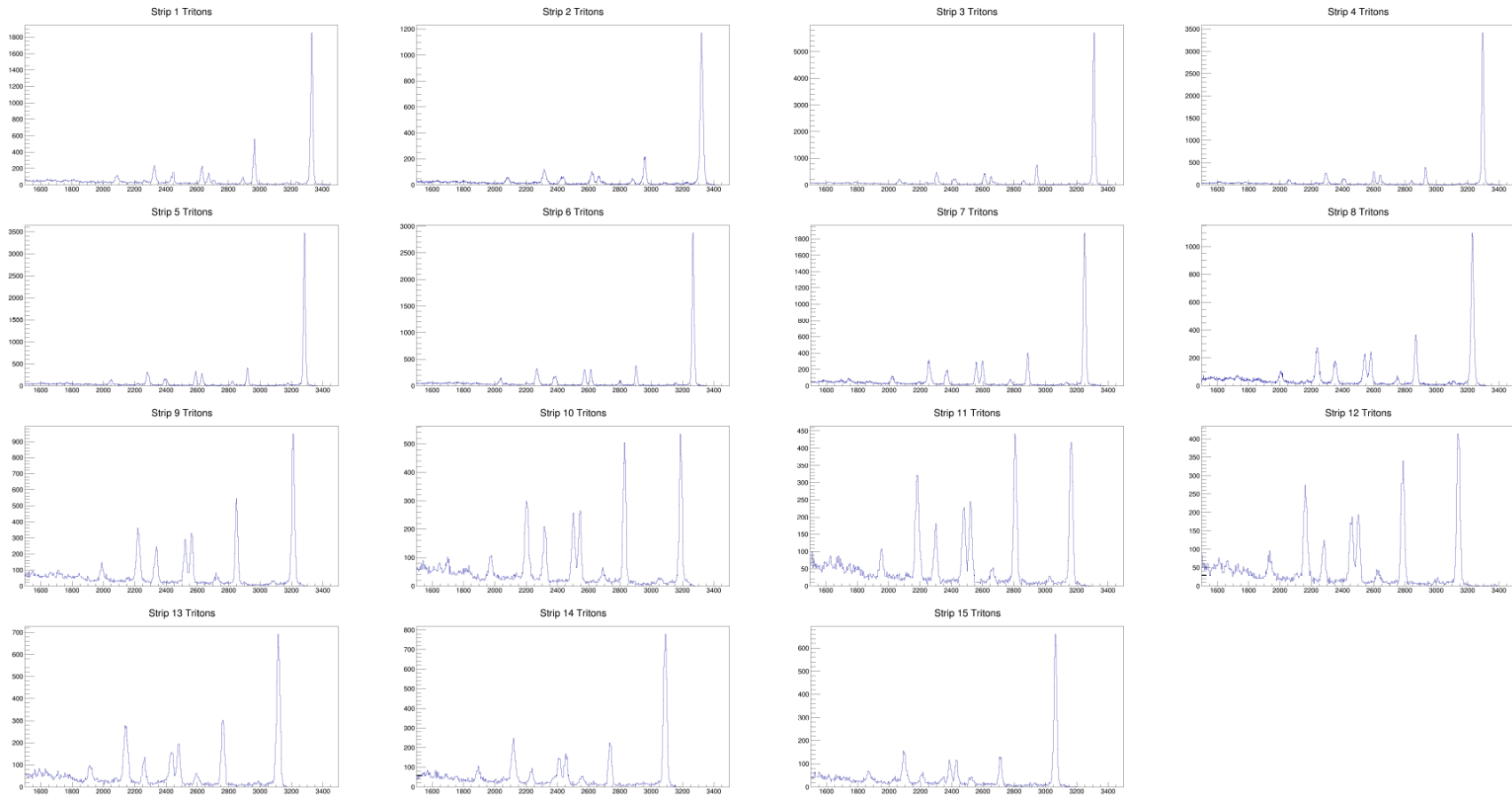


Figure 4.16: The 15 raw triton spectra of strips 1 through 15, used to extract excitation energies and peak integrals used in the analysis of this work. For all plots, the y-axis is number of counts, and the x-axis is channel number (approximately 5 keV per channel), with smaller triton energies corresponding to lower excitation energies.

4.4 Nitrogen background

At angles covered by strips five, six, seven and eight (Between 30° and 40°), the triton peak corresponding to the first excited state in ^{12}N overlaps with tritons corresponding to the $E_x = 3376$ keV state. To account for this background, a published study, Chipps et al[48], of the $^{14}\text{N}(\text{p,t})^{12}\text{N}$ reaction, performed using JENSA with the same detector configuration as the present work was used.

Ratios of the ^{12}N ground state to the ^{12}N first excited state were extracted for the corresponding angles from Chipps et al[48], then the number of tritons measured corresponding to the ^{12}N ground state in the present study were used to subtract the ^{12}N first excited state contribution from the $E_x = 3376$ keV state ^{18}Ne triton peak. As a result of this background subtraction, the uncertainty is higher on those points. This background is present in all 3 states in ^{18}Ne between $3000 < E_x < 4000$ keV.

The study used to correct for the ^{12}N background does not report for the angles covered by strips nine and ten. The nitrogen background still has to be subtracted, so ratios of the ground state of ^{12}N to the first excited state from strips either side were used to correct for the ^{12}N contribution to this peak, with larger uncertainties to account for the subtraction.

Chapter 5

Results

Here I present angular distributions for the ground state, four bound excited states, nine previously measured resonances up to $E_x = 6350$ keV, and a potential new state at $E_x = 5308 \pm 12$ keV. The interpretation of these results will be given in Chapter 6. Four of the states were used as part of the energy calibration. Excitation energies are presented for states where they were found as part of this study. There are three doublets included in this work, at $E_x \approx 3600$ keV, $E_x \approx 5100$ keV, and $E_x \approx 6300$ keV. Where constituent states are separated by 50 keV or less, the individual states are difficult to resolve in this measurement.

For the analysis of the $^{20}\text{Ne}(p,t)^{18}\text{Ne}$ reaction presented here, the assumption is made that the particle transfer is a one step process, consisting of a single 2n nucleon transfer. This results in a spin transfer of $S=0$. Operating under this assumption, we should expect to strongly populate only those states in ^{18}Ne that have J^π assignments that do follow from $\pi = (-1)^L$ and $J = L$, referred to as natural parity states.

For each of the states, a comparison of these data is made to previous literature, and for states where there is uncertainty in the J^π assignment, a χ^2 comparison between DWBA calculations for possible L transfers is presented. All DWBA calculations presented here use the optical model parameters listed in Table 2.1. Tables throughout this chapter list reported states with assignments, omitting states used as part of a calibration and references which only adopt previous values. For states where the excitation energy values were fixed in fits, the values from the latest Evaluated Nuclear Structure Data File were adopted. Where

doublets are treated as a single peak, the combined DWBA calculations use ratios between constituent peaks at 23.5° in the laboratory.

Where there are angular distributions from previous published $^{20}\text{Ne}(p,t)^{18}\text{Ne}$ studies, the data have been extracted and is shown alongside angular distributions from the present work, where applicable. Table 5.1 lists details of the three studies from which triton distributions have been extracted: Falk et al[9], Nero et al[8] and Park et al[10]. These studies were performed with differing proton beam energies to the present work, and as a result there are minor differences in the shape of the triton angular distribution between the previous work and the present study. Data extracted from other publications has been scaled to these data for better comparison of the shape of the angular distribution.

Individual excitation energy values extracted for each strip are listed in Appendix D

Table 5.1: Proton beam energies and targets used in the present work and previous $^{20}\text{Ne}(p,t)^{18}\text{Ne}$ studies.

Reference	E_{beam}	Target
Present Study	37 MeV	Natural neon gas jet
Falk et al[9]	42 MeV	Gas cell with thin Kapton window
Nero et al[8]	41.8 MeV	Gas cell with thin Kapton window
Park et al[10]	35 MeV	^{20}Ne implanted carbon foil

5.1 Ground state

The angular distribution of measured tritons from the population of the ground state of ^{18}Ne are shown in Figure 5.1. As ^{20}Ne and ^{18}Ne are even-even nuclei, the ground states of both are 0^+ , and an L=0 transfer the only possible case. The locations of the maxima and minima in the angular range covered by the detectors are compatible with the DWBA calculation, which is key in determining L-transfer. The shape is well described by the calculation at lower angles, but at higher angles the calculation has a sharper minimum than the measured distribution. This suggests that the optical model is doing a good job of describing the angular distribution, but it is not perfect. Variations in the optical model parameters affect the sharpness of the minima, as well as relative heights of the features.

An L=0 DWBA calculation with $E_{beam} = 42$ MeV is also shown in Figure 5.1 alongside these data, for better comparison between these data and previous work. There is a slight shift in the location of the second minima between the two calculations, due to the differing beam energies. The shape of these data also agrees well with two previous studies over the angular distribution covered in this work. The location of the first minima in the calculation performed as part of this study agree to within 3° when compared with angular distributions extracted from Falk et al[9] and Nero et al[8].

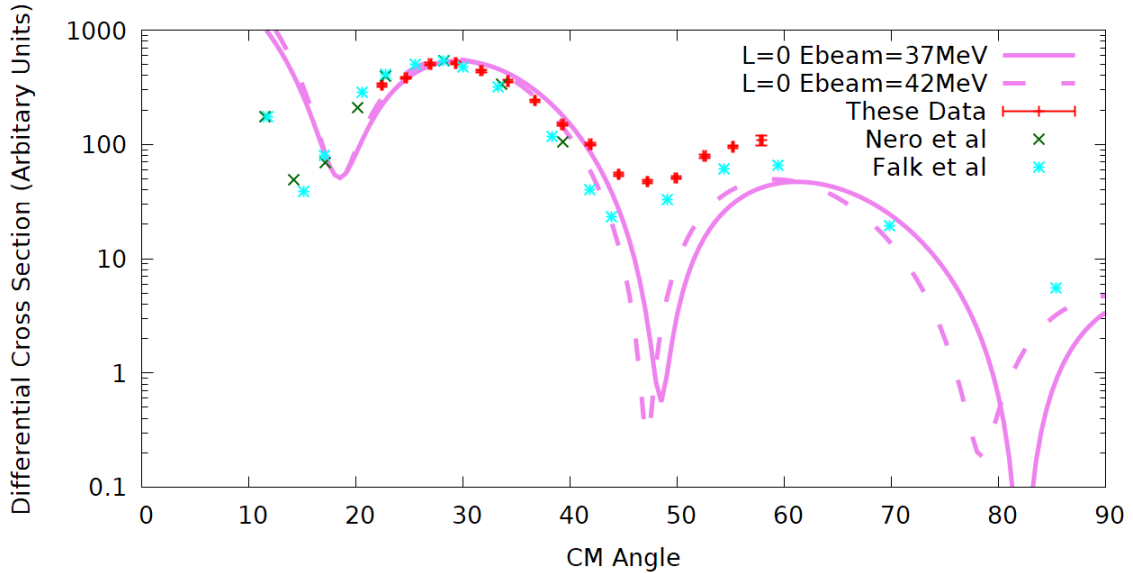


Figure 5.1: Angular distribution for the ground state of ^{18}Ne . The locations of maxima and minima in the distribution agree well with the DWBA calculation, but the relative heights of the features differ at higher angles. Also shown are triton distributions from Nero et al[8] and Falk et al[9], and a second L=0 DWBA calculation performed with $E_{beam} = 42$ MeV.

5.2 $E_x = 1887$ keV state

The $E_x = 1887$ keV state was originally used as part of the calibration, but after finding a discrepancy in the residuals when using this state as part of the calibration (Ref Residuals section) it was removed. Other studies have used the energy of this state as part of their calibrations, and as a result there is only one measurement of the excitation energy of this state.

Previous work on ^{18}Ne and studies on the mirror nucleus ^{18}O constrain the J^π assignment to 2^+ , therefore only an $L=2$ transfer was explored for this state.

The angular distribution for the $E_x = 1887$ keV state in ^{18}Ne is shown in Figure 5.2, alongside calculations for an $L=2$ transfer at both $E_{beam} = 37$ MeV and 42 MeV. A shift of 5° in the location of the second minimum can be seen between calculations for the differing beam energies.

Although the measured distribution is much flatter than the calculation, the location of the peaks and troughs are similar across the angular range covered. Table 5.2 shows the E_x and J^π for this state from Gill et al[1], and the present work.

The shape of the triton angular distribution in the present work agrees with the studies performed by Falk et al[9] and Nero et al[8], although the location of the first minimum appears to be shifted by approximately 4° , as the beam energies differed between these data the previous work. All experimental triton distributions are considerably flatter than the DWBA calculation performed as part of this study.

Table 5.2: J^π and E_x values for the $E_x = 1887$ keV state from Gill et al[1] and the present study. There is slight disagreement between the present value of the excitation energy and the value from Gill et al[1] of 6 keV.

Reference	E_x (keV)	J^π
Present Study	1881 ± 5	2^+
Gill et al[1]	1887.3 ± 0.2	2^+

5.3 $E_x = 3376$ keV state

The $E_x = 3376$ keV state was used as part of the energy calibration. Tritons from this state overlap with tritons from the first excited state in ^{12}N at angles covered by strips five, six, seven and eight, as discussed in Section 4.4. Previous studies constrain the spin-parity assignment to $J^\pi = 4^+$, so only an $L=4$ transfer was explored.

The angular distribution for the $E_x = 3376$ keV state is shown in Figure 5.3. The distribution in the present study is flat and featureless compared with the DWBA calculation,

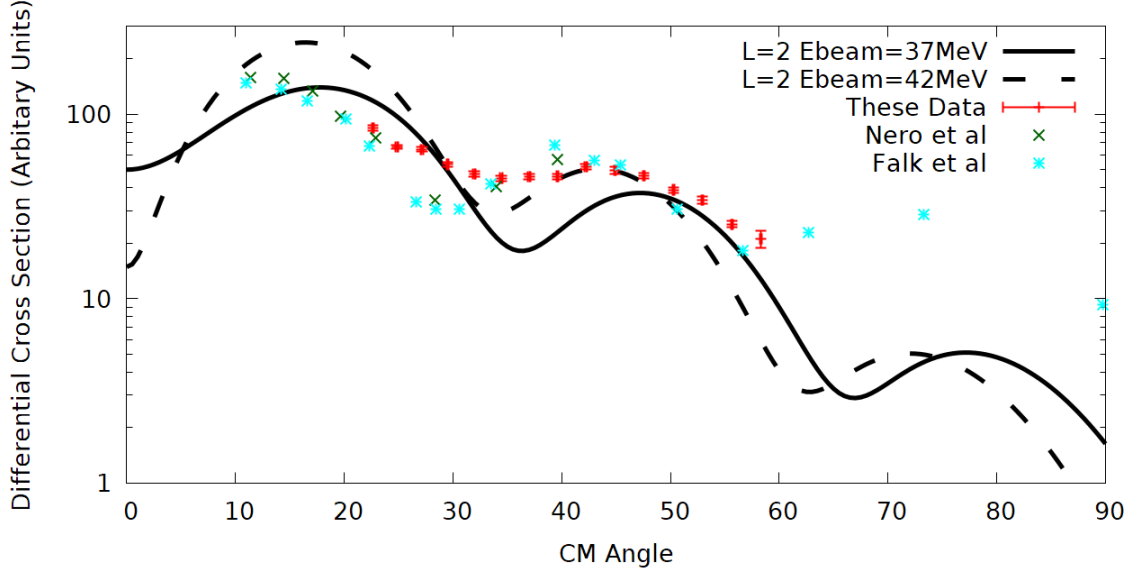


Figure 5.2: Angular distribution of the $E_x = 1887$ keV state. Previous work and mirror arguments constrain the assignment to $J^\pi = 2^+$ therefore only an L=2 transfer was explored for this state. The calculation has a distinctive structure, while the angular distribution is significantly flatter. The trend of the distribution extracted from these data tend to agree with the position of the features, the trough between 30° and 40° and the peak between 40° and 50° . The shape of the triton angular distribution in the present work agrees with the studies performed by Falk et al[9] and Nero et al[8]. A DWBA calculation performed with $E_{beam} = 42$ MeV is also presented for better comparison between these data and previous work.

but has a similar shape to previous studies. Table 5.3 shows the E_x and J^π for this state from Gill et al[1].

Table 5.3: J^π and E_x values from Gill et al[1] and extracted from these data for the $E_x = 3376$ keV state.

Reference	E_x (keV)	J^π
Present Study	3376	4^+
Gill et al[1]	3376.2 ± 0.4	4^+

5.4 $E_x = 3576$ keV state

The $E_x = 3576$ keV and $E_x = 3616$ keV states were difficult to resolve independently, as they are separated in E_x by 40 keV. Triton spectra in these data appear to indicate that

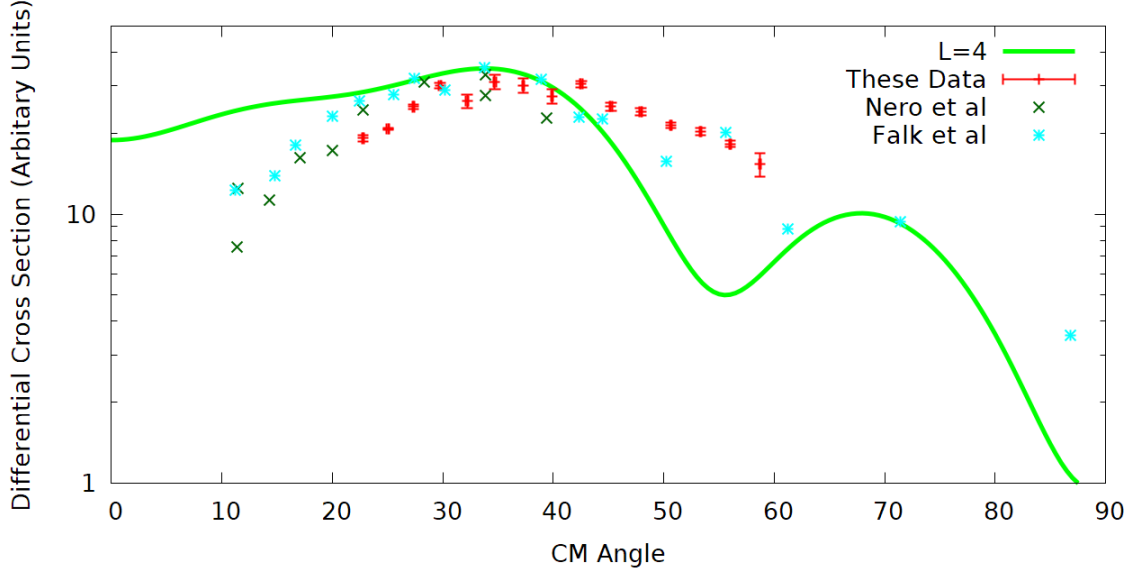


Figure 5.3: Angular distribution of tritons corresponding to the $E_x = 3376$ keV state in ^{18}Ne . There are larger error bars on the points between 30° and 40° due to the subtraction of ^{12}N background, as discussed in Section 5.3. Only L=4 transfer was explored for this state. The extracted distribution is mostly flat while the DWBA calculation for an L=4 transfer shows distinctive features, though these data agrees well with previous work.

there is only one peak located at this energy, while previous studies[1] indicate that this single peak actually contain tritons from two different excitation energies. The peak found at this energy in the present work has a larger width than singlet peaks found in this study, which also indicates that there is more than one component to this triton peak. The bound state peaks from the same reaction should all have approximately the same width for a given angle.

This $E_x = 3576$ keV state and the $E_x = 3616$ keV state were treated in two different ways. Firstly they were fit individually, with the location of this $E_x = 3576$ keV state left as a free parameter in the fit, and the location of the $E_x = 3616$ keV state fixed with values from Gill et al[1]. The results from this fitting method are presented in this Section and Section 5.5. Secondly the two states were also treated as a single peak, which is discussed further in Section 5.6

Tritons from the first excited state of ^{12}N overlapped with tritons from this state at angles covered by strips nine and ten. Refer to Section 4.4 for more detail of the background subtraction for this state.

Previous work and mirror arguments constrain this state to an assignment $J^\pi = 0^+$, therefore only an L=0 transfer was explored for this state. The excitation energy from this study is listed alongside literature values from Gill et al[1] in Table 5.4. The angular distribution for the $E_x = 3576$ keV state is shown in Figure 5.4. There is good agreement between the DWBA calculation and measured distribution for this state. The present study, Nero et al[8], and the DWBA calculation for an L=0 transfer are all in good agreement, with only a slight discrepancy between the calculation and Nero et al[8] data with respect to the location of the first minimum, likely due to the difference in beam energy.

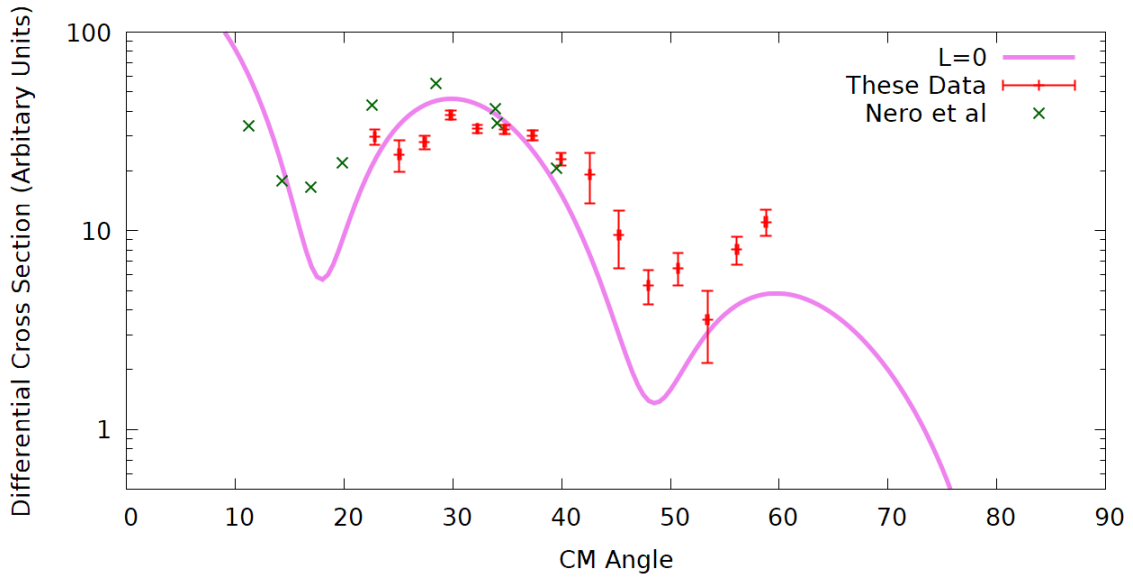


Figure 5.4: Angular distribution for the $E_x = 3576$ keV state. Only an L=0 transfer was explored for this state as previous work has constrained the assignment to $J^\pi = 0^+$. The present study, Nero et al[8] and the DWBA calculation for an L=0 transfer are all in agreement.

Table 5.4: J^π and E_x values from Gill et al[1] and as extracted from these data for the $E_x = 3576$ keV state.

Reference	E_x (keV)	J^π
Present Study	3574 ± 6	0^+
Gill et al[1]	3576.3 ± 2	0^+

5.5 $E_x = 3616$ keV state

For the $E_x = 3616$ keV state, previous work and mirror arguments constrain the assignment to $J^\pi = 2^+$, and therefore only an L=2 transfer was explored for this state.

Tritons from the first excited state in ^{12}N are present in angles covered by strips eleven, twelve and thirteen, with details of the background subtraction given in Section 4.4.

The extracted angular distribution for the $E_x = 3616$ keV state is shown in Figure 5.5 alongside a DWBA calculation for an L=2 transfer. The structure in calculation and experiment match well at angles above 35° , but there is some disagreement between them at lower angles. This disagreement could arise from difficulties resolving the two individual states from the single peak in the fit, especially as the excitation energy for the $E_x = 3616$ keV state was fixed in fits. Overall the distribution agrees well with an L=2 transfer, and there is reasonable agreement between overlapping data points from the present work and Nero et al[8]. The literature value of E_x and J^π for the $E_x = 3616$ keV state from Gill et al[1] are listed in Table 5.5.

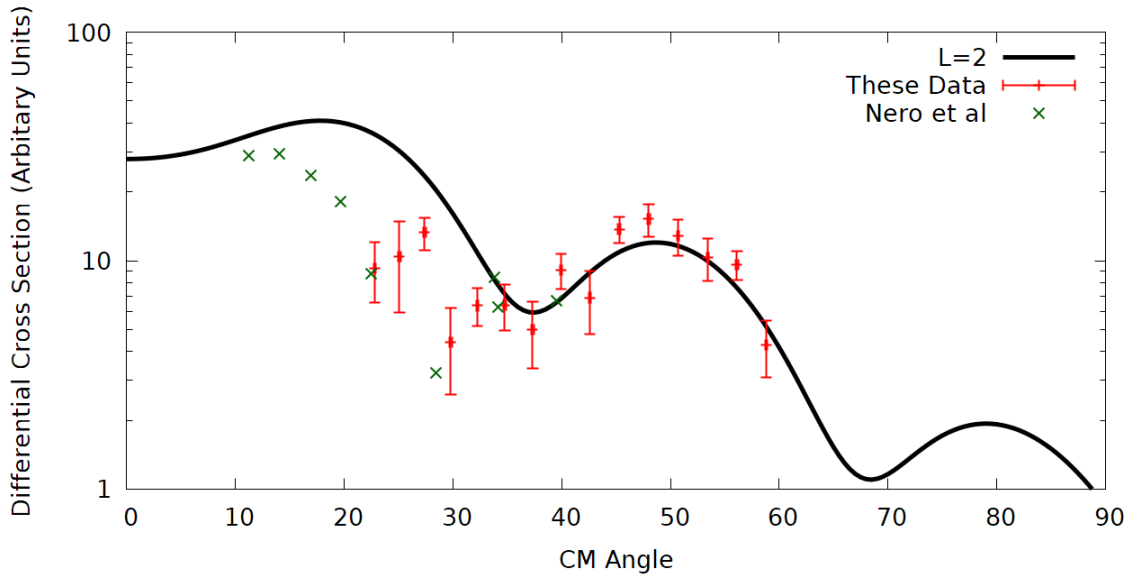


Figure 5.5: Angular distribution for the $E_x = 3616$ keV state. Only an L=2 transfer was explored for this state. At lower angles, there are differences between calculation and the angular distribution while at angles above 35° calculation and these data agree in feature location and relative feature height. There is reasonable agreement at lower angles between these data and Nero et al[8]

Table 5.5: J^π and E_x values from Gill et al[1] and the results from these data for the $E_x = 3616$ keV state.

Reference	E_x (keV)	J^π
Present Study	3616	2^+
Gill et al[1]	3616.4 ± 0.6	2^+

5.6 $E_x = 3600$ keV doublet treated as single peak

The $E_x = 3576$ keV and $E_x = 3616$ keV states were difficult to resolve in the present work. In Sections 5.4 and 5.5 I present angular distributions treating the doublet triton peak as two individual components. In this section I present the angular distribution treating the doublet as a single peak.

This single triton peak corresponds to an excitation energy of $E_x = 3589 \pm 12$ keV. Figure 5.6 shows the angular distribution for this treatment of the two states alongside previous data and a DWBA calculation combining an L=0 transfer for the $E_x = 3576$ keV state and an L=2 transfer for the $E_x = 3616$ keV state.

Falk et al[9] could not resolve the doublet at 3600 keV, while Nero et al[8] resolved the two constituent states. For comparison between the single peak from the present data and Falk et al[9], the two individual components from Nero et al[8] were summed together. The extracted distributions from previous work are in good agreement with each other over the angles they overlap. Agreement between previous data and the present study is also good over angles covered in this work, though there is a difference in the depth of the drop after around 40° , possibly due to differing beam energies.

5.7 $E_x = 4520$ keV state

Previous studies suggest two distinct states separated by only a few keV at $E_x \approx 4520$ keV: a $J^\pi = 1^-$ at $E_x = 4520$ keV, and a $J^\pi = 3^+$ state at $E_x = 4523.7$ keV discovered by Bardayan et al[41]. In this work, we should only expect to strongly populate the $J^\pi = 1^-$ state.

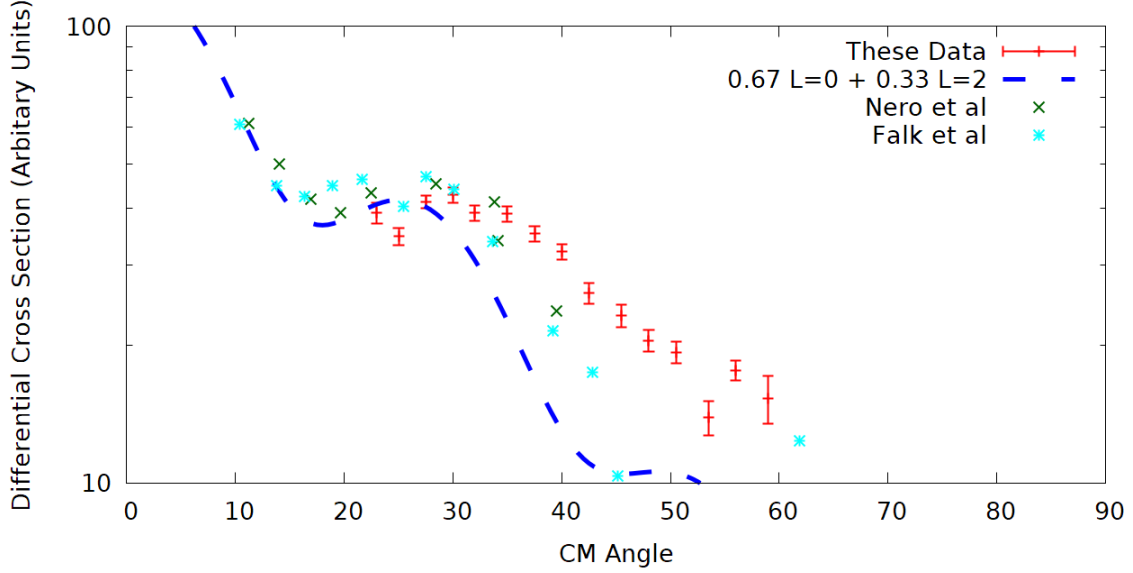


Figure 5.6: Angular distribution of the $E_x = 3600$ keV doublet fit as a single state. This state corresponds to an excitation energy of $E_x = 3589 \pm 12$ keV. The distribution is mostly featureless, appearing flat at lower angles with a downward trend past 30° .

All possible L transfers for the $E_x = 4520$ keV state were explored, with DWBA calculations shown for the L transfers with the lowest two χ^2 , and the angular distribution are shown in Figure 5.7. These data agree with an L=1 transfer, with a slight disagreement in feature height at higher angles, but the structure still agrees well with calculation. Agreement is good between the present study, DWBA calculation for L=1 transfer and Nero et al[8]. The Falk et al[9] reported distribution disagrees with both the present work and Nero et al[8]. This is due to the distribution reported by Falk et al[9] containing components from both the $E_x = 4520$ keV state and the $E_x = 4590$ keV state. The two constituent states in this doublet were resolved in the present work and Nero et al[8]. The summed distribution from both the present work and Nero et al[8] agrees very well with Falk et al[9], as shown in Figure 5.8

Table 5.6 shows literature values for E_x and J^π for this state. χ^2 values of explored L transfers are shown in Table 5.7.

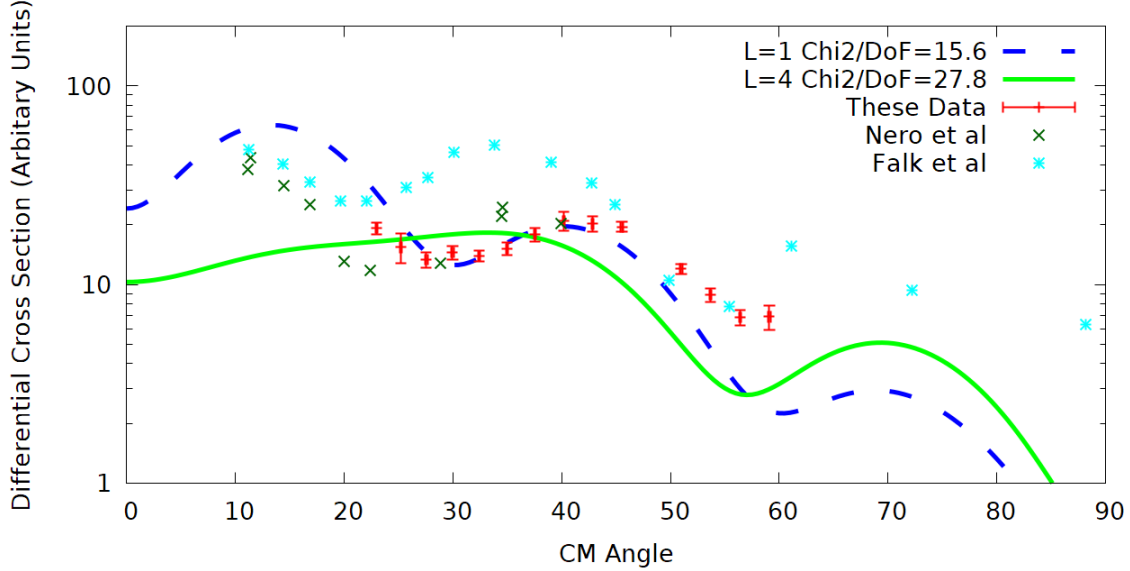


Figure 5.7: Angular distribution for the $E_x = 4520$ keV state. $L=0,1,2,3$ and 4 transfers were all explored for this state, with the two lowest χ^2 values, $L=1$ and $L=4$, shown alongside these data. The DWBA calculation for an $L=1$ transfer agrees very well with these data over the observed angular range. Both calculation and these data follow the same shape, with only slight disagreement in relative feature height at 60° . There is significant disagreement between Falk et al[9] and both these data and Nero et al[8]. This is due to the distribution from Falk et al[9] containing tritons from both the $E_x = 4520$ keV and $E_x = 4590$ keV states being incorrectly attributed to only the $E_x = 4520$ keV state.

5.8 $E_x = 4590$ keV state

Previous work by Hahn et al[16] on the $E_x = 4590$ keV state suggests a $J^\pi = 0^+$ assignment. The angular distribution from these data and the two lowest χ^2 DWBA calculations are shown in Figure 5.9. The angular distribution from these data is in good agreement with the $L=0$ calculation across the measured angular range, which agrees with previous studies.

Table 5.6: J^π and E_x values from Garcia et al[5], Hahn et al[16] and as extracted from these data for the $E_x = 4520$ keV state.

Reference	E_x (keV)	J^π
Present Study	4526 ± 7	1^-
Garcia et al[5]	4519 ± 8	1^-
Hahn et al[16]	4520	1^-

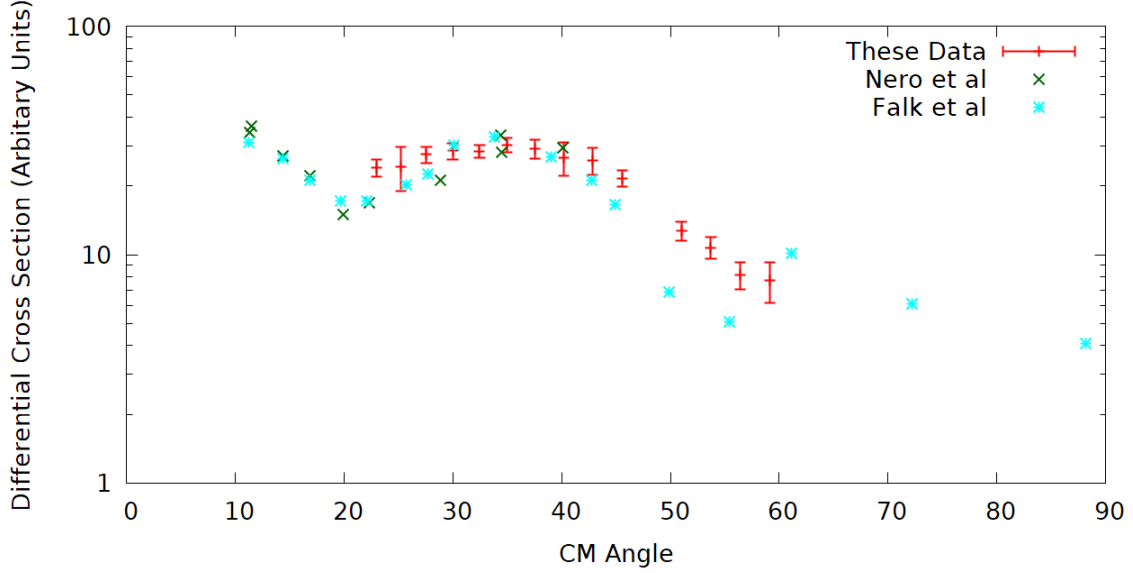


Figure 5.8: Comparison of data from Falk et al[9], Nero et al[8] and these data for the multiplet at $E_x \approx 4500$. Falk et al[9] saw only a single peak, but it had multiple constituents which were completely resolved in both these data and Nero et al[8]. These individual components were summed together for comparison with data from Falk et al[9] in this figure.

The general trend of the distribution from Nero et al[8] agrees over most overlapping angles with respect to these data.

Table 5.8 lists values of J^π and E_x from Hahn et al[16] and Garcia et al[5]. χ^2 of explored L transfers are listed in Table 5.9

Table 5.7: χ^2 values when comparing the angular distribution from this study to DWBA calculations for the different L transfers for the $E_x = 4520$ keV state in ^{18}Ne

L Transfer	χ^2	χ^2/dof
L=0	978.3	69.9
L=1	218.4	15.6
L=2	510.6	36.5
L=3	634.1	45.3
L=4	386.3	27.6

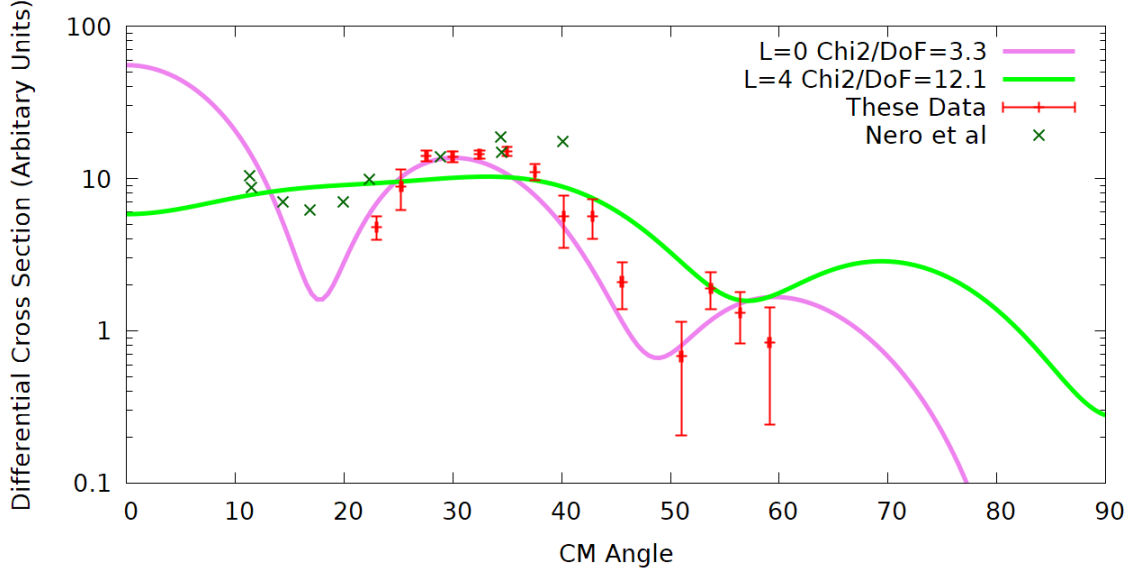


Figure 5.9: Angular distribution for the $E_x = 4590$ keV state. $L=0,1,2,3$ and 4 transfer were all explored for this state and the two lowest χ^2 , DWBA calculations for $L=0$ and $L=4$ transfers are shown. These data and the $L=0$ calculation are in very good agreement, with the presented distribution replicating both relative feature height and location over the angular range studied in the present work. The general trend of the distribution from Nero et al[8] agrees over most overlapping angles with respect to these data.

5.9 $E_x = 5090$ keV state

Near $E_x = 5100$ keV, there are two previously reported states separated by 50 keV, a state at $E_x = 5090$ keV and another at $E_x = 5146$ keV. As 50 keV is smaller than the resolution of the detectors used in the present work, the doublet appears as a single peak in triton spectra for all angles. This doublet was treated in two ways: once as a single peak and again with the previously known constituent states individually fit with fixed excitation energies.

Table 5.8: J^π and E_x values from as extracted from these data, from Garcia et al[5] and Hahn et al[16] for the $E_x = 4590$ keV state.

Reference	E_x (keV)	J^π
Present Study	4596 ± 15	0^+
Garcia et al[5]	4590 ± 8	0^+
Hahn et al[16]	4589	0^+

Table 5.9: χ^2 values for comparing the angular distribution from this study to DWBA calculations for different L transfers for the $E_x = 4590$ keV state.

L Transfer	χ^2	χ^2/dof
L=0	46.56	3.33
L=1	471.37	33.67
L=2	583.91	41.71
L=3	457.50	32.68
L=4	169.22	12.09

The location of tritons from this state were fixed in the fit using the literature value of $E_x = 5090$ keV.

Figure 5.10 shows the angular distribution from the $E_x = 5090$ keV state, with DWBA calculations for L=1,2,3 and 4 transfers shown. At lower angles, these data agree with an L=1 transfer, showing a similar structure. There is disagreement between calculation and these data at angles above 55° . This disagreement at higher angles could potentially be due to the widening resolution that occurs in the higher angle strips, owing to the larger angular coverage of those strips. The distribution extracted from Park et al[10] is flatter than the distribution from the present work. This may be due to the difficulty resolving the two individual components of this doublet in this work. Table 5.10 show the literature values J^π and E_x from Nero et al[8], Hahn et al[16] and Park et al[10], and from these data. χ^2 of explored L transfers are listed in Table 5.11.

Table 5.10: J^π and E_x values from Nero et al[8], Hahn et al[16], and Park et al[10], and from these data for the $E_x=5090$ keV state.

Reference	E_x (keV)	J^π
Present Study	5090	(1 ⁻ , 4 ⁺)
Nero et al[8]	5090±8	(2 ⁺ , 3 ⁻)
Hahn et al[16]	5106	3 ⁻
Park et al[10]	5110	2 ⁺

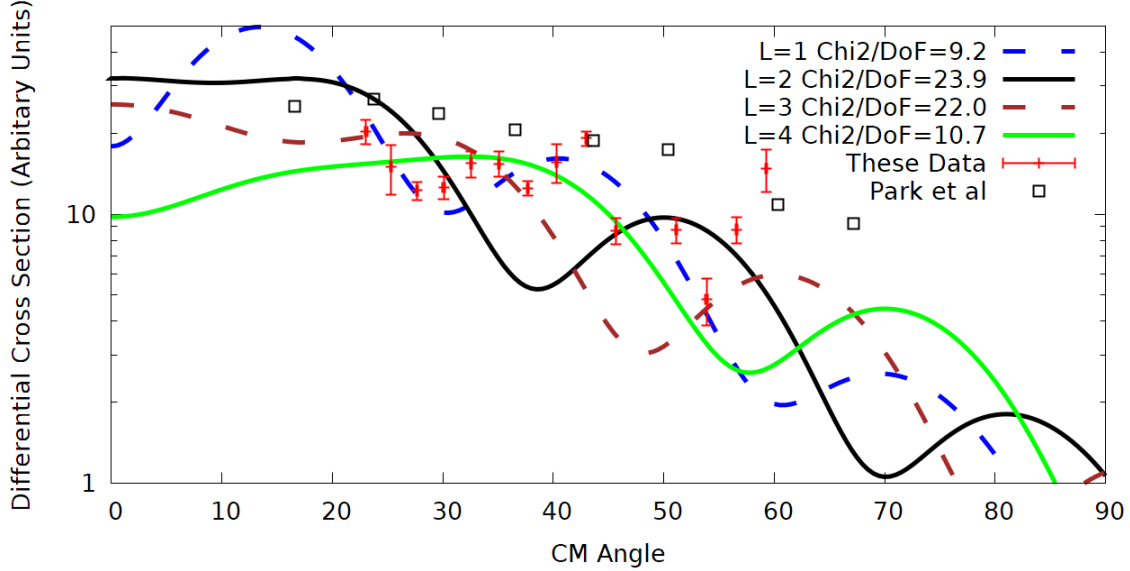


Figure 5.10: Angular distribution for the $E_x = 5090$ keV state. All possible L-transfer were explored for this state. DWBA calculations for L=2 and L=3 transfers are shown alongside these data, because of previous assignments to this state. The transfers with the two lowest χ^2 values are also shown. At lower angles, this combined distribution is featureless and flat, with a small bump at around 35° the extracted distribution appears flat, with larger variations in the differential cross section appearing at higher angles. The value presented from this work was adopted from Nero et al[8]

5.10 $E_x = 5146$ keV state

The $E_x = 5146$ keV state is part of a doublet near $E_x = 5100$ keV state, as mentioned in Section 5.9, and it was difficult to resolve the two constituent states. To allow for the separation of the single peak into the two constituent states, the location of this state was fixed at each angle using $E_x = 5146$ keV, the value listed in the latest ENSDF[2] of ^{18}Ne . The angular distribution for this state is shown in Figure 5.11. This distribution is mostly flat along the angular range with a slight bump at 53° . The location of this bump does not agree with any of the DWBA calculations performed for this state. As was the case for the $E_x = 5100$ keV state, the distribution extracted from Park et al[10] is flatter than the distribution from the present work. This may be due to the difficulty resolving the two individual components of this doublet in this work. Table 5.12 shows the values for E_x and J^π from Nero et al[8], Hahn et al[16], and Park et al[10]. The χ^2 of explored L transfers when compared to these data are shown in Table 5.13.

Table 5.11: χ^2 values for comparing the angular distribution from this study to DWBA calculations for the different possible L transfers for the $E_x = 5090$ keV state.

L Transfer	χ^2	χ^2/dof
L=0	438.1	31.3
L=1	128.4	9.2
L=2	310.4	22.2
L=3	286.6	20.5
L=4	149.8	10.7

Table 5.12: J^π and E_x values from Nero et al[8], Hahn et al[16], and Park et al[10], and as extracted from these data for the $E_x = 5146$ keV state.

Reference	E_x (keV)	J^π
Present Study	5146	(4+)
Nero et al[8]	5154 ± 7	(2 ⁺ , 3 ⁻)
Hahn et al[16]	5153	2 ⁺
Park et al[10]	5150	3 ⁻

5.11 $E_x \approx 5100$ keV doublet treated as single peak

This Section reports the results from treating the doublet at $E_x \approx 5100$ keV as a single peak. These data, previous work, and a combined DWBA calculation of an L=2 and an L=3 transfer are shown in Figure 5.12. This combined distribution is featureless and flat, with a small bump at around 35° . This peak corresponds to an excitation energy of $E_x = 5130 \pm 12$ keV. Multiple previous studies suggest that there are two states at this energy. The

Table 5.13: χ^2 values when comparing the angular distribution from this study to DWBA calculations for the different possible L transfers for the $E_x = 5146$ keV state.

L Transfer	χ^2	χ^2/dof
L=0	1216.5	86.9
L=1	869.4	62.1
L=2	1293.2	92.4
L=3	981.4	70.1
L=4	607.0	43.4

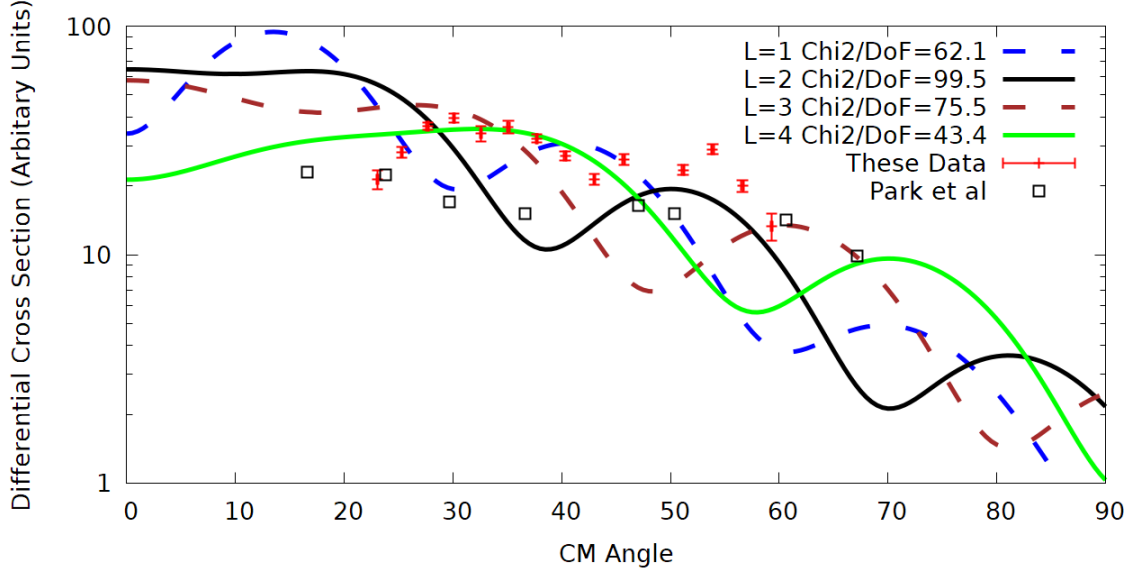


Figure 5.11: Angular distribution for the $E_x = 5146$ keV state. All possible L-transfer were explored for this state. DWBA calculations for L=2 and L=3 transfers are shown alongside these data, because of previous assignments to this state. The transfers with the two lowest χ^2 values are also shown. The angular distribution is mostly flat for the $E_x = 5146$ keV state. The lower angle structure compares favorably with an L=4 transfer, though the distribution from Park et al[10] is significantly flatter than these data, indicating difficulties separating the two constituent states of the single peak.

combined distribution from this doublet compares well when summing the two individual constituent states of this doublet from Park et al[10]. Falk shows a maxima at 23° , which is not present in the distribution from the present work, or the combined distribution from Park et al[10]. This could be due to the differing beam energies between Falk et al[9], the present work and Park et al[10]. The sum of the two states from Park et al[10] agree well with the doublet distribution in the present work, and there is agreement at most overlapping angles agree with respect to the distribution published by Falk et al[9].

5.12 $E_x = 5450$ keV state

The $E_x = 5450$ keV state was used as part of the energy calibration, with the location of this state free in the fit. For the energy calibration, the excitation energy of $E_x = 5453$ keV was used[2]. Previous work suggests an assignment of $J^\pi = 2^-$ for this state, which is off-parity and should not be strongly populated via $^{20}\text{Ne}(p,t)^{18}\text{Ne}$.

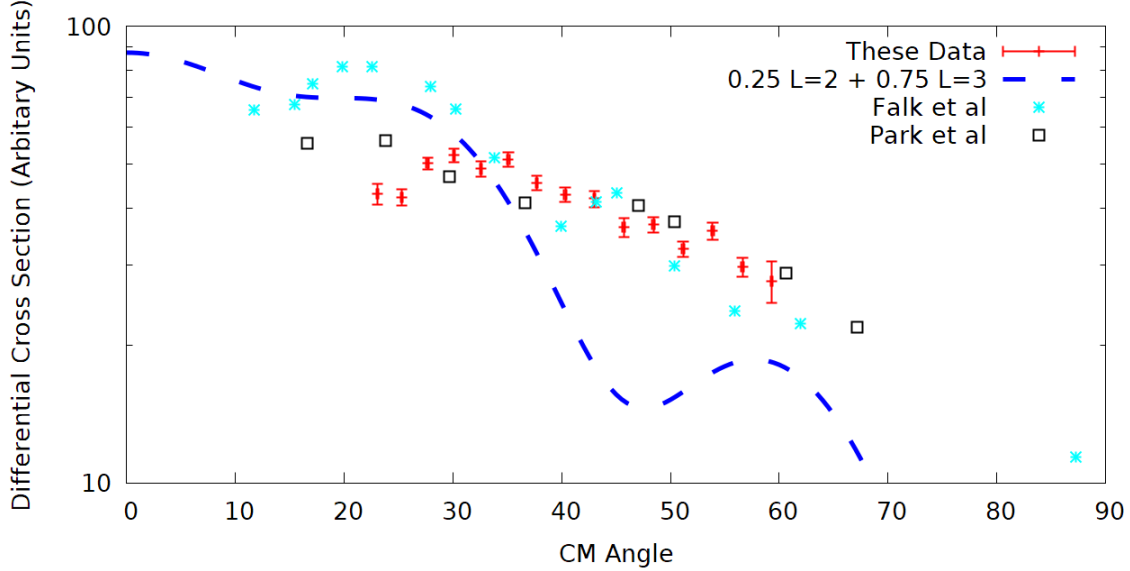


Figure 5.12: Angular distribution of the $E_x = 5090$ keV and $E_x = 5146$ keV doublet fit as a single peak. The angular distribution appears mostly featureless, with a small bump at around 35° . This single peak corresponds to $E_x = 5130 \pm 12$ keV. There is good agreement between these data and Park et al[10] across all angles covered in the present work, and a slight disagreement between Falk et al[9], these data and Park et al[10] at lower angles.

In the present study, the $E_x = 5450$ keV state is clearly seen at all angles, and the angular distribution from these data is shown alongside DWBA calculations for an L=0, L=3 and L=4 transfers in Figure 5.13. These data agree with the calculation for an L=3 transfer and, although the χ^2 for the L=4 calculation is lower than the L=0 calculation, the shape of the distribution agrees better with the L=0 calculation.

Table 5.14 shows the literature values of J^π and E_x as reported in Nero et al[8], Hahn et al[16], and Park et al[10] with the values from these data. χ^2 of explored L transfers are shown in Table 5.15.

Table 5.14: J^π and E_x values from Nero et al[8], Hahn et al[16], and Park et al[10], and from these data for the $E_x = 5450$ keV state.

Reference	E_x (keV)	J^π
Present Study	5453	$(0^+, 3^-)$
Nero et al[8]	5453 ± 10	2^-
Hahn et al[16]	5454	2^-
Park et al[10]	5467 ± 5	N/A

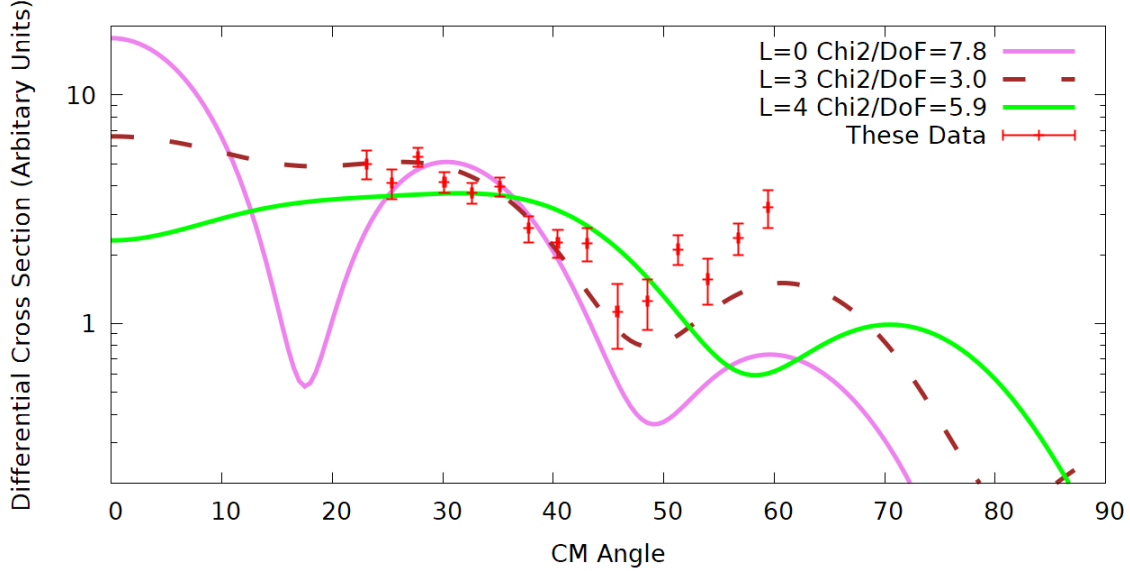


Figure 5.13: Angular distribution for the $E_x = 5450$ keV state. L=0,1,2,3 and 4 transfer were all explored for this state. The distribution shows a slow decline from 20° to 45° with a minima at 45° , then an increase in differential cross section at angles between 45° to 60° . This is well described by DWBA calculations for an L=3 transfer. The relative height of features suggest that L=3 better agree with these data than L=0.

5.13 $E_x = 6150$ keV state

The $E_x = 6150$ keV state was used as part of the energy calibration, with an excitation energy of $E_x = 6150$ keV used[2]. The angular distribution from these data for the $E_x = 6150$ keV state is shown alongside DWBA calculations for L=1, L=3, and L=4 transfers in Figure 5.14. The distribution is fairly flat over the angular range with a small peak at 27° , and a small dip at 50° . The calculation for the L=1 transfer is not compatible with these data, but an L=3 transfer follows the same trend as these data over the angular range. An

Table 5.15: χ^2 values for the different possible L transfers for the $E_x = 5450$ keV state.

L Transfer	χ^2	χ^2/dof
L=0	109.4	7.8
L=1	171.2	12.2
L=2	108.1	7.7
L=3	42.5	3.0
L=4	82.0	5.9

L=0 transfer is also in good agreement with these data. Table 5.16 shows current literature values E_x and the J^π assignments for this state, and χ^2 of all explored L transfers are shown in Table 5.17

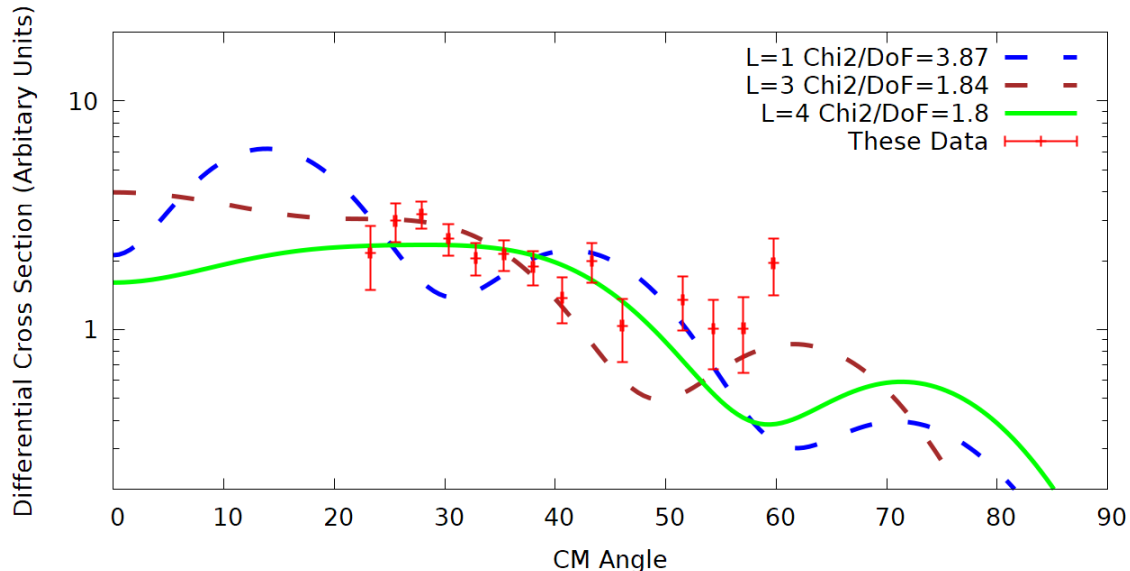


Figure 5.14: Angular distribution for the $E_x = 6150$ keV state, shown alongside DWBA calculations for L=1, L=3, and L=4 transfer. DWBA calculations for an L=3 or L=4 are the lowest χ^2 when compared to the extracted distribution, and the L=1 transfer calculation is shown because of the abundance of previous studies assigning this state a $J^\pi = 1^-$. Mirror arguments also constrain the possible L transfer to L=1, L=3 or L=4 with the assumption of S=0. The structure of the extracted angular distribution does not agree with an L=1 transfer, but is much more compatible with an L=3 transfer.

5.14 $E_x = 6297$ keV state

Previous studies suggest two states within 50 keV near $E_x = 6300$ keV, a state at $E_x = 6297$ keV and another at $E_x = 6353$ keV. These two states were difficult to resolve in the present study and as such were treated in the same way as other doublets in this work, both as a single peak and as two independent states. The location of this state was fixed in the fits, and an excitation energy of $E_x = 6297$ keV was used[2]. For the two independent states case, the angular distribution for the $E_x = 6297$ keV state is shown in Figure 5.15, alongside DWBA calculations for an L=1, L=3 and L=4 transfer, chosen because of mirror nucleus constraints. Features in this distribution are less pronounced compared to calculations. The

Table 5.16: J^π and E_x values from previous studies and from these data for the $E_x = 6150$ keV state.

Reference	E_x (keV)	J^π
Present Study	6150	(3 ⁻)
Hahn et al[16]	6150±100	(1 ⁻)
Harss et al[29]	6150	1 ⁻
Blackmon et al[30]	6137	1 ⁻
He et al[31]	6180±60	1 ⁻
Hu et al[33]	6150±30	1 ⁻

Table 5.17: χ^2 values for comparing the angular distribution from this study to DWBA calculations for the different possible L transfers for the $E_x = 6150$ keV state.

L Transfer	χ^2	χ^2/dof
L=0	46.29	3.31
L=1	54.23	3.87
L=2	43.35	3.10
L=3	25.76	1.84
L=4	25.42	1.82

distribution presented in Falk et al[9] compares well to the distribution from these data. Table 5.18 lists the J^π and E_x for the $E_x = 6297$ keV state from literature and these data. χ^2 of explored L transfers are shown in Table 5.19.

5.15 $E_x = 6353$ keV state

The $E_x = 6353$ keV state is part of a doublet at $E_x \approx 6300$ keV. Because of the close proximity of the two states, the location was fixed using a literature value of $E_x = 6353$ keV[2]. This allowed for separation of the two constituent states of the single peak. The angular distribution for this is shown in Figure 5.16 alongside DWBA calculations for an L=1, L=3 and L=4 transfer. This distribution is flat and had no defining features across the measured angular range.

Table 5.20 shows the values for E_x and J^π for the $E_x = 6353$ keV state from literature, and χ^2 of explored L transfers are shown in Table 5.21.

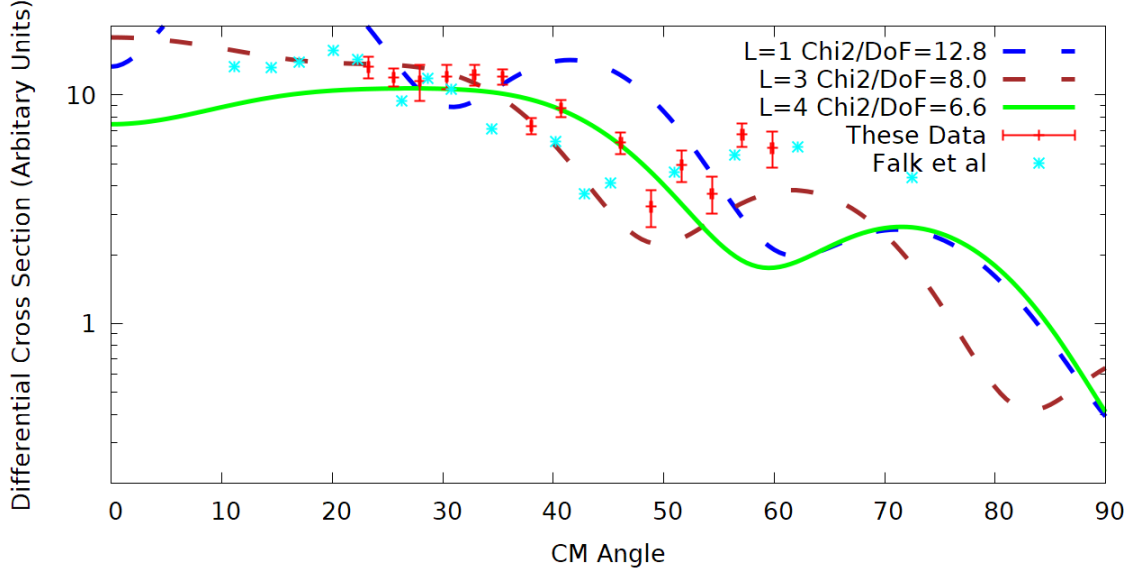


Figure 5.15: Angular distribution for the $E_x = 6297$ keV state shown alongside DWBA calculations for an L=1, L=3 and L=4 transfer, chosen because of mirror nucleus constraints and low χ^2 values. An L=3 transfer calculation seems to describe the presented distribution well. The distribution presented in Falk et al[9] compares well to the distribution from these data.

5.16 $E_x \approx 6300$ keV doublet treated as single peak

As described in Section 5.14, the doublet at $E_x \approx 6300$ keV was treated as two individual states, with results presented in Sections 5.14 and 5.15, and as a single peak, the results of which are presented in this section. Figure 5.17 shows the angular distribution when treating this doublet as an individual peak. In the present study, this peak is a single peak in triton spectra at all angles. Previous studies suggest two states at this energy, as discussed in Section 5.14. The distribution for this single peak is mostly flat with a small bump at 55° . This peak corresponds to an excitation energy $E_x = 6315 \pm 11$ keV.

5.17 Potential candidate state at $E_x \approx 5300$ keV

A weakly populated state at $E_x = 5309 \pm 13$ keV was identified between 23° and 41° in the center of mass in this study. Figures 5.18 and 5.19 show raw count spectra for 27.5° and 32.5° in the center of mass respectively, with known peaks labeled and the unidentified peak

Table 5.18: J^π and E_x values from literature and as extracted from these data for the $E_x = 6300$ keV state.

Reference	E_x (keV)	J^π
Present Study	6297	(1 ⁻ , 4 ⁺)
Nero et al[8]	6297±10	4 ⁺
Hahn et al[16]	6286	4 ⁺
Park et al[10]	6305±4	N/A
Harss et al[29]	6290	3 ⁻
Hu et al[33]	6280±30	3 ⁻

Table 5.19: χ^2 values for comparing the angular distribution from this study to DWBA calculations for the different possible L transfers for the $E_x = 6297$ keV state.

L Transfer	χ^2	χ^2/dof
L=0	175.6	12.5
L=1	179.2	12.8
L=2	221.3	15.8
L=3	111.7	8.0
L=4	92.4	6.6

labeled 5300 keV. Figure 5.20 shows the angular distribution for this previously unobserved candidate state. χ^2 of explored L transfers are shown in Table 5.22.

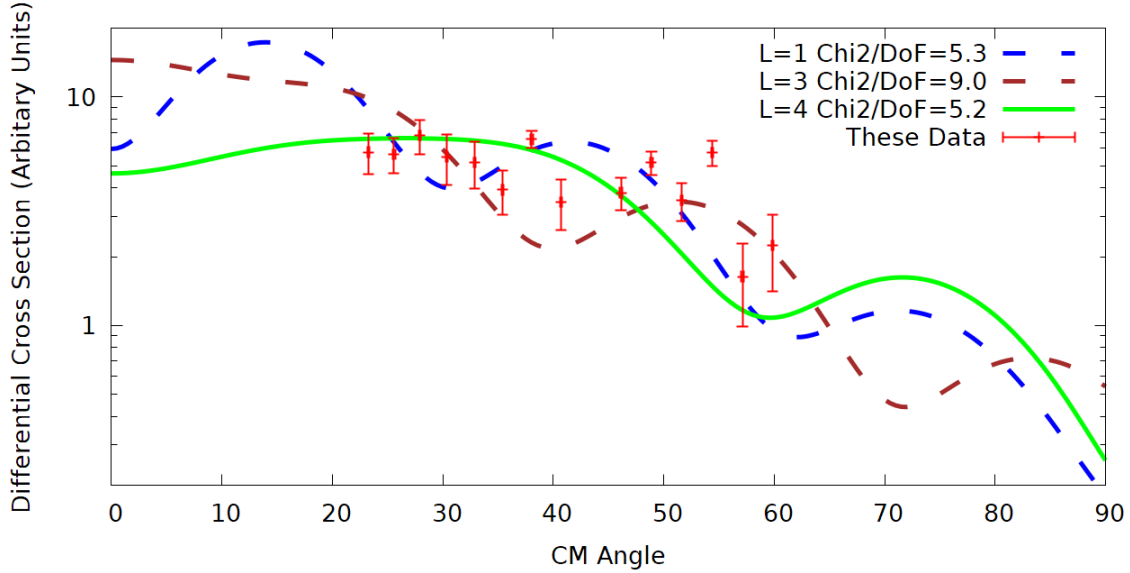


Figure 5.16: Angular distribution for the $E_x = 6353$ keV state shown alongside DWBA calculations for an L=1, L=3 and L=4 calculation, chosen because of mirror nucleus constraints and low χ^2 values. The distribution for this state does not show any pronounced features across the measured angular range.

Table 5.20: J^π and E_x values from literature and from these data for the $E_x = 6353$ keV state.

Reference	E_x (keV)	J^π
Present Study	6353	(2-)
Nero et al[8]	6353 ± 10	N/A
Hahn et al[16]	6345	2-
Park et al[10]	6358 ± 5	N/A
Harss et al[29]	6350	2-
Hu et al[33]	6350 ± 30	3-

Table 5.21: χ^2 values comparing the angular distribution from this study to DWBA calculations for the different possible L transfers for the $E_x = 6353$ keV state.

L Transfer	χ^2	χ^2/dof
L=0	152.5	10.9
L=1	74.2	5.3
L=2	109.7	7.8
L=3	125.3	9.0
L=4	72.7	5.2

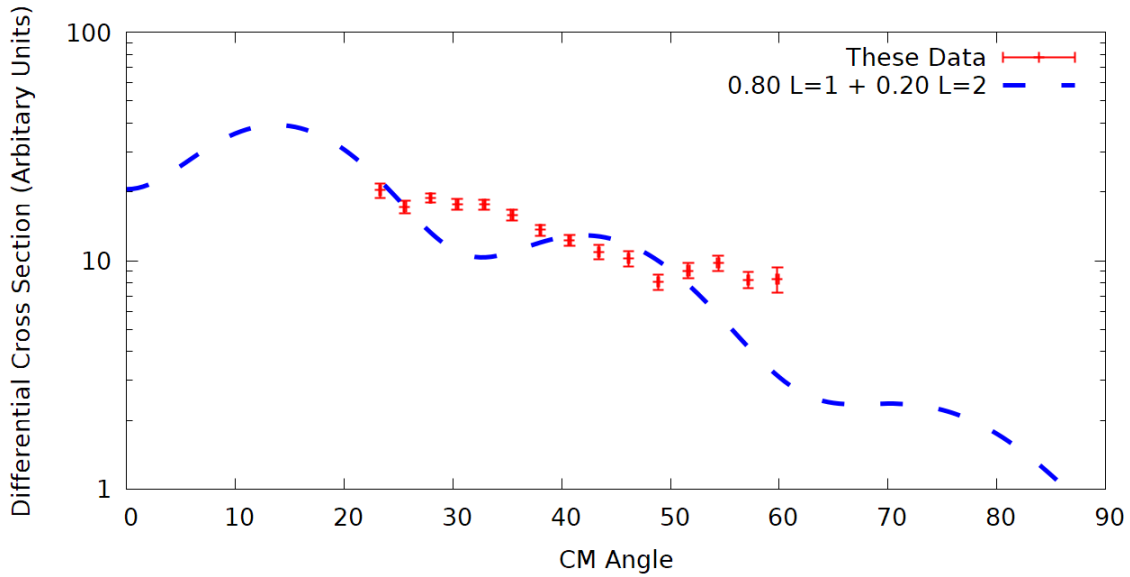


Figure 5.17: Angular distribution of the $E_x = 6297$ keV and $E_x = 6353$ keV doublet fit as a single peak. The excitation energy of this single peak corresponds to $E_x = 6315 \pm 11$ keV. Previous work indicates two states at this energy, therefore this combined distribution is expected to be flatter than that of a single state, with less pronounced features. There are no defining features aside from a small bump at around 55° .

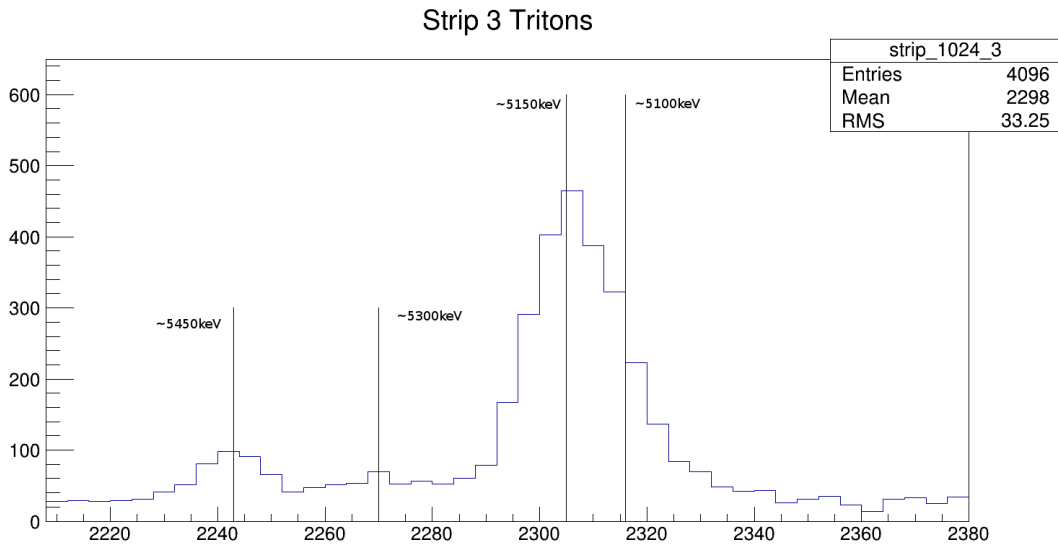


Figure 5.18: Raw counts vs channel plot with three labeled previously observed states and a potential new state as detected at 27.5° in the center of mass. This state corresponds to $E_x = 5309 \pm 13$ keV

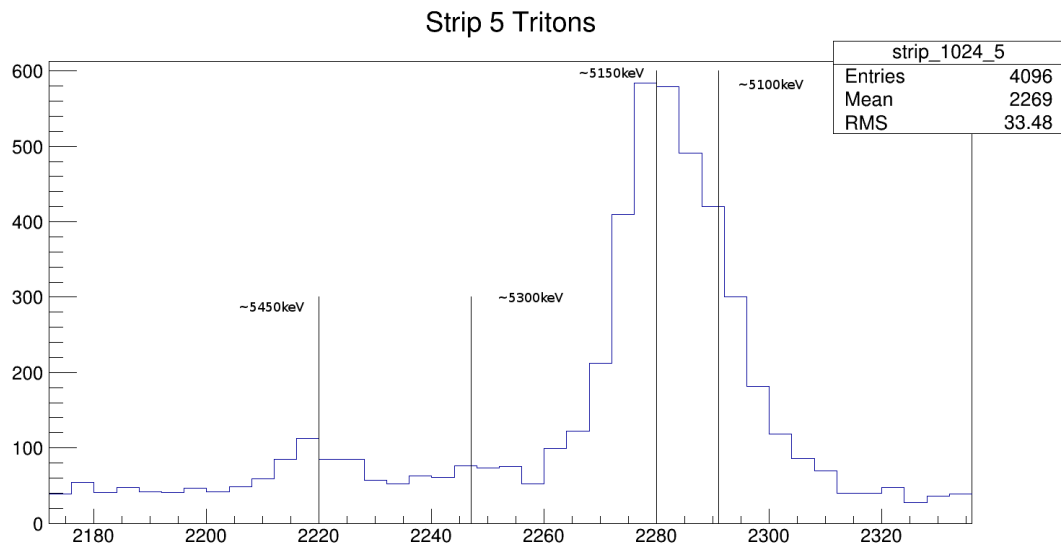


Figure 5.19: Raw counts vs channel plot with three labeled previously observed states and a potential new state as detected at 32.5° in the center of mass. This state corresponds to $E_x = 5309 \pm 13$ keV

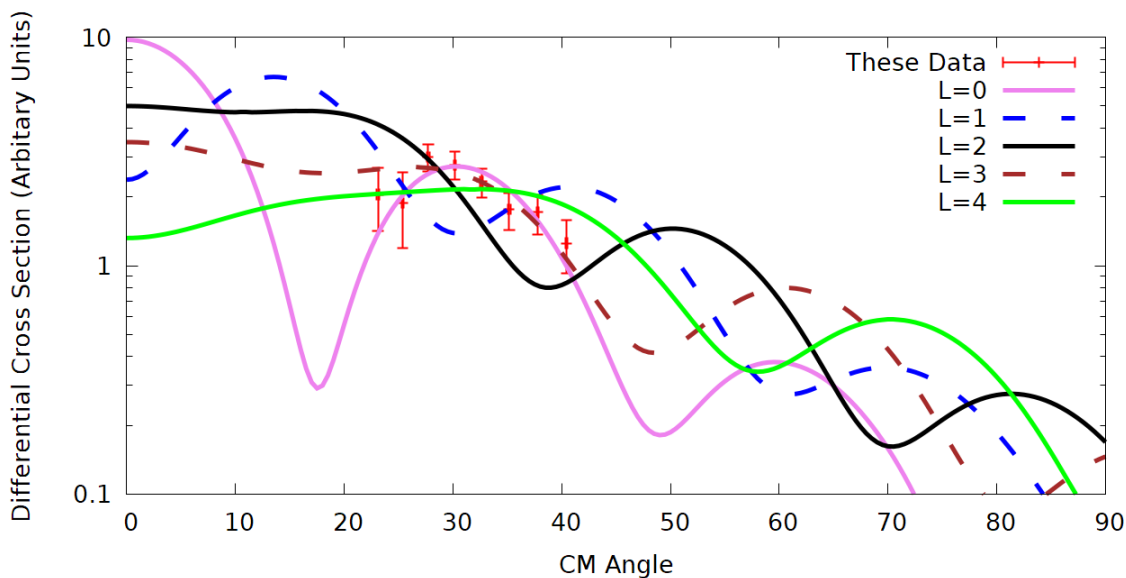


Figure 5.20: Angular distribution of the triton peak observed at $E_x = 5309 \pm 13$ keV shown alongside DWBA calculations for L=0 through L=4 transfers..

Table 5.22: χ^2 values for comparing the angular distribution from this study to DWBA calculations for the different possible L transfers for the $E_x = 5300$ keV state.

L Transfer	χ^2	χ^2/dof
L=0	6.2	0.9
L=1	43.6	6.2
L=2	38.3	5.5
L=3	4.4	0.6
L=4	12.5	1.8

Chapter 6

Conclusions

In this chapter, the results presented in Chapter 5 will be discussed and compared to current literature. Discussion of agreement and discrepancies between previously published work and the current study will also be presented, and where there are differences, the impact and potential reasons for these differences will also be explored.

6.1 States $E_x > 6000$ keV

This section discusses three states: the $E_x = 6150$ keV state (Refer to Figure 5.14 and Table 5.17), $E_x = 6297$ keV state (Refer to Figure 5.15 and Table 5.19), and $E_x = 6353$ keV state (Refer to Figure 5.16 and Table 5.21).

The present study suggests that the $E_x = 6150$ keV state is not well described by L=1 transfer, as features in the L=1 DWBA calculation are not compatible with the angular distribution from these data. The distribution from this work is more compatible with an L=3 transfer, matching the general shape of the distribution and relative feature height well. The conclusion from almost all previous studies for this state has been an assignment of $J^\pi = 1^-$, though there has been a reanalysis of previous work which disagrees with this conclusion.

He et al[40] performed a reanalysis of the work done by Gomez del Campo et al[39], who studied $^{17}\text{F}(p,p)^{17}\text{F}$. According to the R-matrix analysis performed as part of the reanalysis, He et al[40] could not replicate the $J^\pi = 1^-$ assignment for this state, as a $J^\pi = 1^-$ resonance at this energy would have a completely different structure to the measured cross sections. This

reanalysis concludes that a $J^\pi = 3^-$ assignment for the 6150 keV state in ^{18}Ne is more suitable than the long-established $J^\pi = 1^-$ assignment, and these data agree with this conclusion.

There are three states in the $6000 \text{ keV} < E_x < 6500 \text{ keV}$ region in the well studied mirror nucleus, ^{18}O : $E_x = 6198.2 \text{ keV}$ with a $J^\pi = 1^-$ assignment, $E_x = 6351.3 \text{ keV}$ with a $J^\pi = (2^-)$ assignment and $E_x = 6404.4 \text{ keV}$ with a $J^\pi = 3^-$ assignment. There is also a $J^\pi = 4^+$ state which lies at $E_x = 7116.9 \text{ keV}$. We expect to very weakly populate the unnatural parity $J^\pi = 2^-$ state via $^{20}\text{Ne}(p,t)^{18}\text{Ne}$, leaving $J^\pi = 1^-, 3^-$ or 4^+ via mirror nucleus constraints for the $E_x = 6150 \text{ keV}$ state. Considering mirror arguments and the angular distribution presented, a tentative assignment of $J^\pi = (3^-)$ is given to the $E_x = 6150 \text{ keV}$ state in the present work.

For the doublet at $E_x \approx 6300 \text{ keV}$, the reanalysis performed by He et al[40] suggests that an assignment of $J^\pi = 1^-$ is more suitable. While the same conclusion cannot be drawn from the angular distribution of the $E_x = 6297 \text{ keV}$ state alone, the present work observed strong population of the $E_x = 6297 \text{ keV}$ state via the $^{20}\text{Ne}(p,t)^{18}\text{Ne}$ reaction and a weak population of the $E_x = 6353 \text{ keV}$ state. Treating the doublet as a single peak yields an $E_x = 6315 \pm 11 \text{ keV}$, which leans closer to the $E_x = 6297 \text{ keV}$ state, suggesting significantly stronger population of the $E_x = 6297 \text{ keV}$ state relative to the $E_x = 6353 \text{ keV}$ state. Park et al[10] did state that they fully resolved the two independent states in the $E_x \approx 6300 \text{ keV}$ doublet, reporting excitation energies and widths for the two states, though there were no spin-parity assignments to either states in the doublet. Mirror nucleus considerations suggest a $J^\pi = 1^-$ state, a $J^\pi = 2^-$ state, a $J^\pi = 3^-$ state here, and a $J^\pi = 4^+$ state lies 700 keV higher. Thomas-Ehrman shifts of approximately 700 keV are present when comparing other analog states between ^{18}O and ^{18}Ne . For these reasons, the present work suggests a tentative assignment of $J^\pi = (1^-, 4^+)$ for the $E_x = 6297 \text{ keV}$ state, and an assignment of $J^\pi = (2^-)$ for the $E_x = 6353 \text{ keV}$ state.

The $J^\pi = 1^-$ state dominates the $^{14}\text{O}(\alpha, p)^{17}\text{F}$ cross section at the temperatures involved in Type-1 x-ray bursts[6], and calculations performed by He et al[40] show that if the $E_x = 6297 \text{ keV}$ state is $J^\pi = 1^-$ rather than the $E_x = 6150 \text{ keV}$ state, then the $^{14}\text{O}(\alpha, p)^{17}\text{F}$ reaction rate is a factor of 6 lower than previous calculations suggest, at $T_9=0.4$. At temperatures $< T_9=0.9$, $^{15}\text{O}(\alpha, \gamma)^{19}\text{Ne}$ will be the most dominant reaction rate for breakout

of the CNO-cycle. Above that, in more extreme conditions, $T_9 > 0.9$, this reaction will strongly contribute to breakout from the hot CNO cycle.

6.2 States $4500 < E_x < 4600$ keV

This section discusses three states: the $E_x = 4520$ keV state (Refer to Figure 5.7 and Table 5.7), $E_x = 4561$ keV state, and the $E_x = 4590$ keV state (Refer to Figure 5.9 and Table 5.9).

Previous work suggests that there are three states in ^{18}Ne between $4500 < E_x < 4600$ keV. Hahn et al[16] report a $J^\pi = 1^-$ state at $E_x = 4520$ keV, a $J^\pi = 3^+$ state at $E_x = 4561$ keV, and a $J^\pi = 0^+$ state at $E_x = 4590$ keV, while Bardayan et al[41] found that the $J^\pi = 3^+$ state lies at $E_x = 4523.7 \pm 2.9$ keV. The $J^\pi = 3^+$ state is an unnatural parity state and should only be very weakly populated in the present work.

There are two other published triton angular distributions in this energy region, Falk et al[9] and Nero et al[8]. The shape of the angular distributions published in Nero et al[8] for the $E_x = 4520$ keV and $E_x = 4590$ keV states both agree with the present work, but there is a discrepancy between the distribution for the $E_x = 4520$ keV state from Falk et al[9], with both Nero and the present study. The distribution presented as $E_x = 4520$ keV in Falk et al[9] does however agree very well with a combined distribution of the $E_x = 4520$ keV and $E_x = 4590$ keV states from the present work. This is indicative that Falk et al[9] measured both the $E_x = 4520$ keV and $E_x = 4590$ keV states in their work, although they could not resolve the individual constituent states.

The excitation energies and spin parity assignments of the $E_x = 4520$ keV and $E_x = 4590$ keV states agree with known states in ^{18}Ne , past studies indicate an unnatural parity state in this energy range, $E_x = 4523.7 \pm 2.9$ keV with an assignment of $J^\pi = 3^+$. The present work showed no hints of this state, which is expected and supports the assumption that unnatural parity states are weakly populate in this reaction.

6.3 States $5000 < E_x < 5500$ keV

This section discusses four states, three previously observed states: the $E_x = 5090$ keV state (Refer to Figure 5.10 and Table 5.11), $E_x = 5146$ keV state (Refer to Figure 5.11 and Table 5.13), and $E_x = 5450$ keV state (Refer to Figure 5.13 and Table 5.15), and a candidate for a previously unobserved state with $E_x = 5309 \pm 13$ keV (Refer to Figure 5.20 and Table 5.22)

6.3.1 $E_x = 5450$ keV

The first study to observe this state was Nero et al[8], giving the $E_x = 5450$ keV state a tentative $J^\pi = 2^-$ assignment, with no further discussion. Hahn et al[16] tentatively agreed, through the observation of this state in two reactions, $^{16}\text{O}(^3\text{He},n)^{18}\text{Ne}$ and $^{12}\text{C}(^{12}\text{C},^6\text{He})^{18}\text{Ne}$. They and did not observe this state in their $^{20}\text{Ne}(p,t)^{18}\text{Ne}$ study. Park et al[10] observed this state in their $^{20}\text{Ne}(p,t)^{18}\text{Ne}$ study, with an excitation energy of $E_x = 5467 \pm 5$ keV, but no spin-parity assignment. These assignments also have a strong mirror argument, as the mirror nucleus ^{18}O has a $J^\pi = 2^-$ state at $E_x = 5530.2$ keV. Although no calculation of the Thomas-Ehrman shift could be found for this state, typical shifts between states in ^{18}O and ^{18}Ne are on the order of ≈ 100 to 200 keV.

In the present work, the $E_x = 5450$ keV state is clearly seen at all angles studied. This is indicative of a natural spin-parity assignment for this state. The triton angular distribution for the $E_x = 5450$ keV state is compatible with both an L=0 and L=3 transfer, though in these data, relative peak and trough heights in the calculation for L=3 transfer better describes these data. There are no known, and unaccounted for, $J^\pi = 0^+$ states in ^{18}O in this energy region. Therefore, we cannot arrive at the same conclusion as the previous work, but instead we tentatively assign this state $J^\pi = (3^-)$.

6.3.2 Candidate for a previously unobserved state at $E_x = 5309 \pm 13$ keV

Hints of an excited state at $E_x = 5309 \pm 13$ keV were seen between 23° and 41° in the triton spectra in the center of mass. This triton peak did not correspond to any known states in

^{18}Ne , and the contaminants ^{12}N , and ^{14}O . At this energy, the density of states in ^{20}Ne is approximately 1 state per 75 keV. The kinematics of this peak suggest that it is from the $^{20}\text{Ne}(p,t)^{18}\text{Ne}$ reaction.

The $E_x = 5450$ keV state is more strongly populated when compared to the population of this candidate state. This peak is seen above background only at forward angles, suggesting an unnatural parity for this candidate state. Therefore a tentative assignment of $J^\pi = (2^-)$ is given to this candidate state.

This tentative assignment is given although the DWBA calculations for an $L=0$ or an $L=3$ transfer matches these data better, as if this state has unnatural parity, the DWBA calculations performed as part of the present work will not accurately reflect the angular distribution, due to the $S=0$ assumption.

The present work is the first study of ^{18}Ne to report the observation of this candidate state at $E_x = 5309 \pm 13$ keV. One possible reason that other studies have not seen this state could be due to background. As an extremely low background target was utilized for this work, and allowed for a clean measurement across the entire energy range studied.

6.3.3 $E_x = 5090$ keV and $E_x = 5146$ keV states

The doublet at $E_x \approx 5100$ keV was not clearly resolved in this work, but there is good agreement with the combined distribution for this doublet and previous work.

Park et al[10] were able to completely resolve the two constituent states in their $^{20}\text{Ne}(p,t)^{18}\text{Ne}$ study, and gave a tentative J^π assignment of (2^+) to the $E_x = 5090$ keV state and (3^-) to the $E_x = 5146$ keV state.

The doublet, when treated as a single peak (Refer to Figure 5.12), corresponds to an excitation energy of $E_x = 5130 \pm 12$ keV, which indicates that the two constituent states are both similarly populated. Strong population of both states in the doublet suggests that the $E_x = 5090$ keV and $E_x = 5146$ keV states in ^{18}Ne are natural parity.

Angular distributions in the present work suggests a tentative $J^\pi = (1^- \text{ or } 4^+)$ to the $E_x = 5090$ keV state, and $J^\pi = (4^+)$ based on the individual distributions. Previous work and known states in the mirror nucleus ^{18}O do not support this conclusion.

6.4 Bound states

This section discusses the five bound states in ^{18}Ne : the ground state (Refer to Figure 5.1), $E_x = 1887$ keV state (Refer to Figure 5.2), $E_x = 3376$ keV state (Refer to Figure 5.3), $E_x = 3576$ keV state (Refer to Figure 5.4), and the $E_x = 3616$ keV state (Refer to Figure 5.5).

6.4.1 Ground state

For the ground state, the L=0 transfer DWBA calculation compares favorably with these data. Feature locations agree but there is a slight disagreement with relative feature height, replicated in experimental angular distributions from previous work[8, 9]. This is indicative that the optical model used in the DWBA calculations is not perfect, though the shape of the transfer is described reasonably. Large variations in optical model parameters are required to shift the locations of maximums and minimums, while small variations in optical model parameters have little effect on the shape of the distribution (Section 2.2.2), but do affect the relative height of features. ^{18}Ne and ^{20}Ne are both even-even nuclei, so for the ground state of both nuclei $J^\pi = 0^+$. This means L=0 transfer is the only possibility. Between previous studies and these data, there is good agreement over the angular range covered in this work.

6.4.2 $E_x = 1887$ keV state

While feature locations compare favorably between the $E_x = 1887$ keV state and L=2 DWBA calculation, there is disagreement between relative peak and trough height. This could be due in part to the optical model parameters used, as the parameters used for this work, from Park et al[10], were adapted for the doublet at $E_x \approx 5100$ keV. Previously published data compares favorably with the current work. There are slight differences in structure over the angular range studied in this work, in part due to the differing beam energies, as a shift of 5° in the location of the second minimum is seen between the calculations. Though the distribution is flat and featureless over the angular range for this state, mirror arguments and previous work constrain the assignment to $J^\pi = 2^+$. The $E_x = 1887$ keV state was also initially part of the calibration, but upon examination of the residuals, a systematic

shift in all strips was observed in the excitation energy of this state when used as part of the calibration. All values extracted from the present study were shifted lower than the expected value when using the calibration to predict the location of the $E_x = 1887$ keV state. Because of this systematic shift, the state was removed from the calibration, and a value for excitation energy for this state was extracted from these data. The present work yields an excitation energy of $E_x = 1881 \pm 5$ keV. This is slightly lower than the currently accepted value of $E_x = 1887 \pm 0.2$ keV reported in Gill et al[1].

6.4.3 $E_x = 3376$ keV state

The L=4 DWBA calculation for the $E_x = 3376$ keV has clear features which are not recreated in the angular distribution in these data. There is however good agreement between Falk et al[9], Nero et al[8] and these data over the angular range studied. Neither previous studies nor these data recreate features in the L=4 DWBA calculation well. The angular distribution presented in Falk et al[9] does not agree with their DWBA calculation in a similar way to the present work; The angular distribution is reasonably well described by the L=4 transfer calculation at angles below 40° , with disagreement between their calculation and angular distribution at higher angles. The spin-parity assignment for this state is still constrained to $J^\pi = 4^+$ due to mirror considerations and previous work.

6.4.4 $E_x = 3576$ keV and $E_x = 3616$ keV states

The doublet at $E_x \approx 3600$ keV is resolved in the present work. The DWBA calculation for an L=0 transfer compared favorably with these data for the $E_x = 3576$ keV state, and the value of $E_x = 3574 \pm 6$ keV from these data agrees with the currently accepted value of $E_x = 3576.3 \pm 2$ keV reported in Gill et al[1]. For the $E_x = 3616$ keV state, the structure of the angular distribution in the present study agrees reasonably well with an L=2 DWBA calculation, and the general shape matches these data over the angular range studied, though there is disagreement with relative feature height at lower angles.

This disagreement could arise as a result of the close proximity of the two states in this doublet. The two individual angular distributions for the constituent states in this doublet compare favorably with previous work performed by Nero et al[8].

6.5 Commissioning of JENSA

The JENSA system was commissioned at Oak Ridge National Laboratory with characterization measurements and commissioning experiments, using the $^{14}\text{N}(\text{p},\text{t})^{12}\text{N}$ [48], $^{20}\text{Ne}(\text{p},\text{d})^{19}\text{Ne}$ [49], $^{20}\text{Ne}(\text{p},\text{t})^{18}\text{Ne}$, $^{15}\text{N}(\alpha,\alpha)^{15}\text{N}$ [11] and $^{120}\text{Sn}(\text{p},\text{t})^{119}\text{Sn}$ [50] reactions, and then moved to the National Superconducting Cyclotron Laboratory at Michigan State University. Characterizations were then performed at the NSCL, along with another commissioning experiment, using the $^{14}\text{N}(\alpha,\text{p})^{17}\text{O}$ reaction. Since then, there has also been a PAC-approved measurement performed with JENSA, $^{34}\text{Ar}(\alpha,\text{p})^{37}\text{K}$. Refer back to Section 3.1.4 for discussion of the jet density measurements performed at both ORNL and the NSCL. The JENSA system has now been fully characterized and commissioned, is operational, and stationed permanently in the ReA3 hall at the NSCL.

6.6 Further work

At excitation energies $E_x > 5000$ keV, triton angular distributions appear to flatten out and lose distinctive features seen at lower excitation energies. This could indicate that we are seeing effects of sequential neutron pickup, and the assumption that $S=0$ is less valid at these higher excitation energies. While two-body effects do change the distribution as a whole, they have a smaller effect on the specific locations of features than a different change in L -transfer. DWBA calculations presented in this work were performed using TWOFNR, which assumes only the $S=0$ transfer mechanism. To take into account these two-step processes, more rigorous calculations will have to be performed using a reaction code such as FRESKO.

There are additional triton peaks at $E_x > 6500$ keV which, due to difficulties modeling the background in the higher excitation energy region, have been omitted in this work. Triton angular distributions will be extracted for these states and compared to DWBA calculations.

There is a discrepancy between this study that the currently accepted excitation energy of the first excited state in ^{18}Ne by 6keV. Many other studies of ^{18}Ne use this state as a calibration state. This discrepancy suggests that excitation energies from studies that have used this state as part of their calibration may be slightly off. A higher resolution study of this state is suggested. Further study of this state could include a high resolution direct measurement of the excitation energy of this state, measuring γ -rays released as the nucleus transitions from the first excited state to the ground state. This could potentially be done via $^{16}\text{O}(^3\text{He},n)^{18}\text{Ne}$.

Bibliography

- [1] R. D. Gill et al., *Physics Letters* **28B 2**, 116 (1968). [x](#), [xiii](#), [10](#), [12](#), [58](#), [77](#), [78](#), [79](#), [80](#), [81](#), [82](#), [107](#)
- [2] D. R. Tilley et al., *Nuclear Physics A* **595**, 1 (1995). [x](#), [xvii](#), [11](#), [12](#), [13](#), [16](#), [56](#), [88](#), [90](#), [92](#), [93](#), [94](#)
- [3] F. Ajzenberg-Selove, *Nuclear Physics A* **392**, 1 (1983). [x](#), [12](#)
- [4] F. Ajzenberg-Selove, *Nuclear Physics A* **475**, 1 (1987). [x](#), [12](#)
- [5] A. Garcia et al., *Physical Review C* **43**, 2012 (1991). [x](#), [xiii](#), [12](#), [84](#), [85](#), [86](#)
- [6] M. Wiescher et al., *The Astrophysical Journal* **316**, 162 (1987). [x](#), [10](#), [11](#), [12](#), [14](#), [15](#), [23](#), [102](#)
- [7] L. Kraus et al., *Physical Review C* **37**, 2529 (1988). [x](#), [12](#)
- [8] A. V. Nero et al., *Physical Review C* **24**, 1864 (2014). [x](#), [xiii](#), [xxiii](#), [xxiv](#), [xxv](#), [12](#), [75](#), [76](#), [77](#), [78](#), [80](#), [81](#), [82](#), [83](#), [84](#), [85](#), [86](#), [87](#), [88](#), [89](#), [91](#), [96](#), [97](#), [103](#), [104](#), [106](#), [107](#), [108](#)
- [9] W. R. Falk et al., *Nuclear Physics A* **157**, 241 (1970). [x](#), [xviii](#), [xix](#), [xx](#), [xxiii](#), [xxiv](#), [xxv](#), [xxvi](#), [12](#), [26](#), [27](#), [28](#), [29](#), [30](#), [31](#), [32](#), [75](#), [76](#), [77](#), [78](#), [82](#), [83](#), [84](#), [85](#), [90](#), [91](#), [94](#), [95](#), [103](#), [106](#), [107](#)
- [10] S. H. Park et al., *Physical Review C* **59 2**, 1182 (1999). [x](#), [xiii](#), [xx](#), [xxv](#), [xxvi](#), [13](#), [26](#), [27](#), [32](#), [75](#), [87](#), [88](#), [89](#), [90](#), [91](#), [96](#), [97](#), [102](#), [104](#), [105](#), [106](#)
- [11] K. A. Chipps et al., *Nuclear Instruments and Methods in Physics Research A* **763**, 553 (2014). [xi](#), [xx](#), [34](#), [35](#), [36](#), [38](#), [40](#), [47](#), [108](#)
- [12] K. Schmidt et al., *Nuclear Instruments and Methods in Physics Research A* (In Preparation). [xi](#), [37](#), [38](#), [40](#)
- [13] K. J. R. Rosman and P. D. P. Taylor, *Pure and Applied Chemistry* **70**, 217 (1998). [xi](#), [41](#)
- [14] Micron Semiconductor Ltd., *Micron semiconductor ltd. catalogue*, Online (2017), <http://www.micronsemiconductor.co.uk/silicon-detector-catalogue/>. [xi](#), [xx](#), [44](#), [45](#)

- [15] M. Drogg, *Larelkin, version 1.12.1*, Online (2017), two-body relativistic kinematics code, documented in the IAEA report IAEA-NDS-08 (February 2017), obtained via the IAEA Nuclear Data Section. [xii](#), [70](#)
- [16] K. I. Hahn et al., Physical Review C **54**, 1999 (1996). [xiii](#), [6](#), [11](#), [13](#), [14](#), [15](#), [84](#), [85](#), [86](#), [87](#), [88](#), [89](#), [91](#), [94](#), [96](#), [97](#), [103](#), [104](#)
- [17] J. M. Saken, *Hr diagram*, <http://www.profjohn.com/courses/ast1004/starlives/starlives.htm> (2002), online; Accessed 1st November 2017. [xvii](#), [2](#)
- [18] Swinburne University of Technology, *Accretion disk*, <https://astronomy.swin.edu.au/cosmos/R/Roche-lobe> (1999), online; Accessed 17th October 2017. [xvii](#), [5](#)
- [19] H. S. M. Wiescher and A. E. Champagne, Philosophical Transactions of the Royal Society A **356**, 2105 (1998). [xvii](#), [7](#)
- [20] K. Langanke and H. Schatz, Physica Scripta **2013**, 014011 (2013). [xvii](#), [7](#)
- [21] R. H. Cyburt et al., The Astrophysical Journal **830:55**, 1 (2016). [xvii](#), [10](#), [11](#), [14](#)
- [22] J. Marion and F. Young, *Nuclear Reaction Analysis Graphs and Tables* (John Wiley & Sons, 1968). [xviii](#), [19](#), [20](#)
- [23] User:Bakken at English Wikipedia, *Shell model diagram*, <https://commons.wikimedia.org/w/index.php?curid=15039395> (2008), online; Accessed 17th October 2017. [xviii](#), [22](#)
- [24] C. E. Rolfs and W. S. Rodney, *Cauldrons in the Cosmos* (The University of Chicago Press, 1988). [8](#), [9](#)
- [25] R. K. Wallace and S. E. Woosley, Astrophysical J. Supplemental Series **45**, 389 (1981). [10](#)
- [26] J. Towle and B. E. F. Macefield, Proceeding of the Physical Society **77**, 399 (1961). [10](#)
- [27] B. C. Robertson et al., Nuclear Physics A **126**, 431 (1969). [11](#)

- [28] D. W. Bardayan et al., Physical Review Letters **83** 1, 45 (1999). [13](#), [44](#)
- [29] B. Harss et al., Physical Review C **65**, 035803 (2002). [13](#), [15](#), [94](#), [96](#), [97](#)
- [30] J. C. Blackmon et al., Nuclear Physics A **718**, 127c (2003). [13](#), [14](#), [15](#), [94](#)
- [31] J. J. He et al., The European Physical Journal A **47**, 67 (2011). [13](#), [15](#), [94](#)
- [32] S. Almaraz-Calderon et al., Physical Review C **86**, 025801 (2012). [13](#)
- [33] J. Hu et al., Physical Review C **90**, 025803 (2014). [13](#), [94](#), [96](#), [97](#)
- [34] A. Kim et al., Physical Review C **92**, 035801 (2015). [13](#)
- [35] A. Parikh et al., The Astrophysical Journal Supplement Series **178**, 110 (2008). [14](#)
- [36] J. C. Blackmon et al., Nuclear Physics A **688**, 142c (2001). [14](#)
- [37] M. Notani et al., Nuclear Physics A **746**, 113 (2004). [14](#)
- [38] C. Fu, V. Z. Goldberg, A. M. Mukhamedzhanov, G. G. Chubarian, G. V. Rogachev, B. Skorodumov, M. McCleskey, Y. Zhai, T. Al-Abdullah, G. Tabacaru, et al., Phys. Rev. C **76**, 021603 (2007), URL <https://link.aps.org/doi/10.1103/PhysRevC.76.021603>. [14](#)
- [39] G. del Campo et al., Physical Review Letters **86**, 43 (2001). [15](#), [101](#)
- [40] J. J. He, H. W. Wang, J. Hu, L. Li, L. Y. Zhang, M. L. Liu, S. W. Xu, and X. Q. Yu, ArXiv e-prints (2017), [1001.2053](#). [15](#), [101](#), [102](#)
- [41] D. W. Bardayan et al., Physical Review C **62**, 055804 (2000). [15](#), [82](#), [103](#)
- [42] K. A. Chipps et al., Physical Review Letters **102**, 152502 (2009). [16](#)
- [43] G. R. Satchler, *Introduction To Nuclear Reactions* (Oxford University Press, 1990). [24](#)
- [44] I. J. Thompson and F. M. Nunes, *Nuclear Reactions for Astrophysics* (Cambridge, 2009). [25](#), [26](#), [28](#)

- [45] J. A. Tostevin, *University of surrey version of the code twofnr (of m. toyama, m. igarashi and n. kishida) and code front (private communication)*, Online (2017), <http://www.nucleartheory.net/NPG/code.htm>. 25
- [46] T. Tamura, Phys. Rep. **14C**, 59 (1974). 28
- [47] G. R. Satchler, Nuc. Phys. **55**, 1 (1964). 28
- [48] K. A. Chipps et al., Physical Review C **92**, 0344325 (2015). 36, 44, 73, 108
- [49] D. W. Bardayan et al., Physical Review C **96**, 055806 (2017). 36, 44, 108
- [50] D. W. Bardayan et al., Nuclear Instruments and Methods in Physics Research B **407**, 297 (2017). 36, 108
- [51] W. K. G. Bittner and W. Schuster, Nuclear Instruments and Methods **167**, 1 (1979). 36
- [52] K. Schmid and L. Veisz, REVIEW OF SCIENTIFIC INSTRUMENTS **83**, 053304 (2012). 36
- [53] G. F. Knoll, *Radiation Detection and Measurement* (John Wiley & Sons, 2000). 38, 43
- [54] B. Singh and E. Browne, Nuclear Data Sheets **109**, 2439 (2008). 39
- [55] C. Hanke and J. Laursen, Nuclear Instruments and Methods **151**, 253 (1978). 39
- [56] M. S. Basunia, Nuclear Data Sheets **107**, 2323 (2006). 40
- [57] G. Mills, *Private communication with gerald mills* (2017). 43
- [58] T. Davidson et al., Nuclear Instruments and Methods in Physics Research A **454**, 350 (2000). 44
- [59] K. G. McKay, Nuclear Instruments and Methods in Physics Research A **288**, 212 (1990). 46
- [60] D. B. O.B. Tarasov, Nuclear Instruments and Methods in Physics Research B **266**, 4657 (2008). 51

- [61] R. Brun and F. Rademakers, *Root - an object oriented data analysis framework*, <http://root.cern.ch/> (1996), proceedings AIHENP'96 Workshop, Lausanne, Sep. 1996, Nucl. Inst. Meth. in Phys. Res. A 389 (1997) 81-86. [65](#)

Appendices

A Length of runs

Table 1 provides a list of the start and stop times of each of the .ldf files used in this analysis, and the numbers of the runs contained in each file.

Table 1: Length of runs

File	Runs contained	Start	Stop
ne20pt01.ldf	1,2	14:30	16:22
ne20pt03.ldf	3,4	16:24	17:56
ne20pt05.ldf	5,6	17:58	19:56
ne20pt07.ldf	7,8	19:58	21:54
ne20pt09.ldf	9	12:39	13:35
ne20pt10.ldf	10	13:37	13:44
ne20pt11.ldf	11	15:56	16:12
ne20pt12.ldf	12,13	16:17	17:41
ne20pt14.ldf	14,15	17:42	19:31
ne20pt16.ldf	16,17	19:32	21:40
ne20pt18.ldf	18	21:41	22:08
ne20pt19.ldf	19,20	11:34	
ne20pt21.ldf	21,22	13:04	14:49
ne20pt23.ldf	23	15:12	15:52
ne20pt24.ldf	24,25,26,27	15:54	17:35
ne20pt28.ldf	28,29,30	17:36	18:42
ne20pt31.ldf	31,32,33	18:43	19:44
ne20pt34.ldf	34,35,36,37,38	19:45	22:08
ne20pt40.ldf	40	12:58	13:49
ne20pt41.ldf	41	16:23	17:24

B Downtime correction values and uncertainties

Table 2 through Table 15 show the number of counts in the peak corresponding to tritons from the ground state of ^{18}Ne . Uncertainties reported by the fit, and statistical uncertainties corresponding to $\frac{\sqrt{N}}{N}$ are reported. For uncertainty propagation calculations, the larger of the two reported uncertainties were used. Data collected in telescope 3 for set of runs 5 has been discarded due to electronics issues.

Table 2: Number of counts in the peak corresponding to ^{18}Ne tritons in telescope 1 for runs included in set 1. The uncertainty reported by the fit and the statistical uncertainty ($\frac{\sqrt{N}}{N}$) are listed.

Strip	Counts	Fit error (%)	$\frac{\sqrt{N}}{N}$
4	1993	2.0	2.2
5	1899	1.9	2.3
6	1691	2.1	2.4
7	1418	2.2	2.7
8	792	3.3	3.6

Table 3: Number of counts in the peak corresponding to ^{18}Ne tritons in telescope 2 for runs included in set 1. The uncertainty reported by the fit and the statistical uncertainty ($\frac{\sqrt{N}}{N}$) are listed.

Strip	Counts	Fit error (%)	$\frac{\sqrt{N}}{N}$
5	1789	2.2	2.4
6	1288	2.3	2.8
7	720	2.9	3.7
8	553	3.7	4.3

Table 4: Number of counts in the peak corresponding to ^{18}Ne tritons in telescope 3 for runs included in set 1. The uncertainty reported by the fit and the statistical uncertainty ($\frac{\sqrt{N}}{N}$) are listed.

Strip	Counts	Fit error (%)	$\frac{\sqrt{N}}{N}$
4	1901	2.2	2.3
5	1889	2.1	2.3
6	1523	2.4	2.6
7	1192	2.6	2.9
8	729	3.4	3.7

Table 5: Number of counts in the peak corresponding to ^{18}Ne tritons in telescope 1 for runs included in set 2. The uncertainty reported by the fit and the statistical uncertainty ($\frac{\sqrt{N}}{N}$) are listed.

Strip	Counts	Fit error (%)	$\frac{\sqrt{N}}{N}$
4	2467	2.0	2.0
5	2350	2.1	2.1
6	2110	2.0	2.2
7	1634	2.2	2.5
8	890	2.8	3.4

Table 6: Number of counts in the peak corresponding to ^{18}Ne tritons in telescope 2 for runs included in set 2. The uncertainty reported by the fit and the statistical uncertainty ($\frac{\sqrt{N}}{N}$) are listed.

Strip	Counts	Fit error (%)	$\frac{\sqrt{N}}{N}$
5	2248	2.1	2.1
6	1765	2.2	2.4
7	1185	2.6	2.9
8	982	2.9	3.2

Table 7: Number of counts in the peak corresponding to ^{18}Ne tritons in telescope 3 for runs included in set 2. The uncertainty reported by the fit and the statistical uncertainty ($\frac{\sqrt{N}}{N}$) are listed.

Strip	Counts	Fit error (%)	$\frac{\sqrt{N}}{N}$
4	2439	1.9	2.0
5	2361	1.9	2.1
6	2096	2.1	2.2
7	1561	2.5	2.5
8	1033	2.9	3.1

Table 8: Number of counts in the peak corresponding to ^{18}Ne tritons in telescope 1 for runs included in set 3. The uncertainty reported by the fit and the statistical uncertainty ($\frac{\sqrt{N}}{N}$) are listed.

Strip	Counts	Fit error (%)	$\frac{\sqrt{N}}{N}$
4	1577	2.1	2.5
5	1562	2.1	2.5
6	1495	2.0	2.6
7	1119	2.4	3.0
8	633	3.3	4.0

Table 9: Number of counts in the peak corresponding to ^{18}Ne tritons in telescope 2 for runs included in set 3. The uncertainty reported by the fit and the statistical uncertainty ($\frac{\sqrt{N}}{N}$) are listed.

Strip	Counts	Fit error (%)	$\frac{\sqrt{N}}{N}$
5	1576	2.0	2.5
6	1226	2.3	2.9
7	884	2.5	3.4
8	678	3.1	3.8

Table 10: Number of counts in the peak corresponding to ^{18}Ne tritons in telescope 3 for runs included in set 3. The uncertainty reported by the fit and the statistical uncertainty ($\frac{\sqrt{N}}{N}$) are listed.

Strip	Counts	Fit error (%)	$\frac{\sqrt{N}}{N}$
4	1560	2.1	2.5
5	1570	2.0	2.5
6	1467	2.0	2.6
7	1088	2.5	3.0
8	737	3.0	3.7

Table 11: Number of counts in the peak corresponding to ^{18}Ne tritons in telescope 1 for runs included in set 4. The uncertainty reported by the fit and the statistical uncertainty ($\frac{\sqrt{N}}{N}$) are listed.

Strip	Counts	Fit error (%)	$\frac{\sqrt{N}}{N}$
4	1162	2.2	2.9
5	1214	2.0	2.9
6	1114	2.1	3.0
7	786	2.6	3.6
8	478	3.0	4.6

Table 12: Number of counts in the peak corresponding to ^{18}Ne tritons in telescope 2 for runs included in set 4. The uncertainty reported by the fit and the statistical uncertainty ($\frac{\sqrt{N}}{N}$) are listed.

Strip	Counts	Fit error (%)	$\frac{\sqrt{N}}{N}$
5	1146	2.2	3.0
6	866	2.3	3.4
7	584	2.8	4.1
8	481	3.2	4.6

Table 13: Number of counts in the peak corresponding to ^{18}Ne tritons in telescope 3 for runs included in set 4. The uncertainty reported by the fit and the statistical uncertainty ($\frac{\sqrt{N}}{N}$) are listed.

Strip	Counts	Fit error (%)	$\frac{\sqrt{N}}{N}$
4	1174	2.2	2.9
5	1120	2.1	3.0
6	953	2.2	3.2
7	742	2.6	3.7
8	542	2.9	4.3

Table 14: Number of counts in the peak corresponding to ^{18}Ne tritons in telescope 1 for runs included in set 5. The uncertainty reported by the fit and the statistical uncertainty ($\frac{\sqrt{N}}{N}$) are listed.

Strip	Counts	Fit error (%)	$\frac{\sqrt{N}}{N}$
4	2945	2.0	1.8
5	2895	2.0	1.9
6	2660	2.0	1.9
7	1955	2.4	2.3
8	1150	2.8	2.9

Table 15: Number of counts in the peak corresponding to ^{18}Ne tritons in telescope 2 for runs included in set 5. The uncertainty reported by the fit and the statistical uncertainty ($\frac{\sqrt{N}}{N}$) are listed.

Strip	Counts	Fit error (%)	$\frac{\sqrt{N}}{N}$
5	2776	2.0	1.9
6	2277	2.1	2.1
7	1542	2.5	2.5
8	1123	3.0	3.0

Table 16: Final correction factors. These factors represent the number of raw counts in the ground state of $^{20}\text{Ne}(p,t)^{18}\text{Ne}$ as a ratio to the total number of counts recorded in the corresponding strip. $\Sigma N_x^n/N_{total}^n = 1$

Set	Averaged N_x^n/N_{total}^n	% Uncertainty
1	0.1814	3.12
2	0.2385	2.81
3	0.1653	3.28
4	0.1197	3.77
5	0.2951	2.64

Table 17: Downtime correction factors for telescope 1.

Strip (n)	N_1^n/N_{total}^n	N_2^n/N_{total}^n	N_3^n/N_{total}^n	N_4^n/N_{total}^n	N_5^n/N_{total}^n
4	0.1965	0.2432	0.1555	0.1145	0.2903
5	0.1914	0.2369	0.1575	0.1224	0.2918
6	0.1864	0.2327	0.1648	0.1228	0.2933
7	0.2052	0.2364	0.1619	0.1137	0.2828
8	0.2009	0.2257	0.1605	0.1212	0.2917

Table 18: Downtime correction factors for telescope 2.

Strip (n)	N_1^n/N_{total}^n	N_2^n/N_{total}^n	N_3^n/N_{total}^n	N_4^n/N_{total}^n	N_5^n/N_{total}^n
5	0.1876	0.2358	0.1653	0.1202	0.2911
6	0.1735	0.2378	0.1652	0.1167	0.3068
7	0.1465	0.2411	0.1799	0.1188	0.3137
8	0.1449	0.2573	0.1776	0.1260	0.2942

C List of collaborators

This work would not be possible without the JENSA gas jet target system. The JENSA collaboration involves members at various different institutions. Listed below are those who have significantly contributed to the JENSA project as it exists today.

S. Ahn (Texas A&M University)
D.W. Bardayan (Notre Dame)
J.C. Blackmon (Louisiana State University)
J. Browne (Michigan State University/National Superconducting Cyclotron Laboratory)
K.A. Chipps (Oak Ridge National Laboratory)
O. Gomez (Florida International/Michigan State University)
U. Greife (Colorado School of Mines)
A. Kontos (Michigan State University/National Superconducting Cyclotron Laboratory)
L.E. Linhardt (Louisiana State University)
M. Matos (International Atomic Energy Agency)
Z. Meisel (Ohio University)
F. Montes (Michigan State University/National Superconducting Cyclotron Laboratory)
P.D. O'Malley (Notre Dame)
W.J. Ong (Michigan State University/National Superconducting Cyclotron Laboratory)
S.D. Pain (Oak Ridge National Laboratory)
S.T. Pittman
A. Sachs
H. Schatz (Michigan State University/National Superconducting Cyclotron Laboratory)
K. Schmidt (Michigan State University/National Superconducting Cyclotron Laboratory)
K.T. Schmitt
M.S. Smith (Oak Ridge National Laboratory)
N.F. Soares de Bem (Tennessee Tech University)

D Excitation energies

Table 19 provides a list of the excitations energies extracted for each strip in the present work. These values were used to calculate the uncertainties listed in Chapters 5 and 6.

Table 19: Individual excitation energies for each strip, extracted from these data. All energies are given in keV.

Strip	$E_x = 1887$	$E_x = 3576$	$E_x = 4520$	$E_x = 4590$	$E_x = 5309 \pm 13$
1	1875.9	3576.2			5325.6
2	1878.0	3582.0	4529.0	4599.4	5299.5
3	1880.5	3575.9	4523.4	4589.6	5320.4
4	1884.0	3578.3	4527.9	4593.8	5305.7
5	1881.6	3573.2	4521.1	4590.4	5313.8
6	1884.4	3576.4	4520.1	4586.0	5307.1
7	1885.6	3580.3	4531.5	4593.6	5289.2
8	1882.5	3564.3	4525.9	4593.8	5301.8
9	1879.6	3565.5	4514.4	4581.8	
10	1887.7	3567.6	4537.8	4634.5	
11	1887.0				
12	1871.6				
13	1883.5				
14	1875.0				
15	1874.2				

Vita

Paul Thompson was born in Salford, UK, on December 10th, 1987. He studied Physics at the University of Sheffield, receiving an MPhys in May 2010. He then moved to Knoxville, Tennessee in August 2011 to pursue a Ph.D. in Physics at the University of Tennessee, working as a T.A. for 2 years before starting work with the experimental nuclear astrophysics group at ORNL and starting his work on the JENSA project and his thesis work.